Spectroscopy and Such (Working Title)

By
Blaise Jonathan Thompson

A dissertation submitted in partial fulfillment of
the requirements for the degree of

Doctor of Philosophy
(Chemistry)

at the
UNIVERSITY OF WISCONSIN - MADISON
20xx

Date of final oral examination: xx/xx/xxxx
This dissertation is approved by the following members of the Final Oral Committee:
John C. Wright, Professor, Analytical Chemistry
x
x
x
x

Contents

List of Figures

List of Tables

Acknowledgments

x

Abstract

The explanatory stories that people find compelling are simple; are concrete rather than abstract; assign a larger role to talent, stupidity and intentions than to luck; and focus on a few striking events that happened rather than on the countless events that failed to happen.

The ultimate test of an explanation is whether it would have made the event predictable in advance.

Paradoxically, it is easier to construct a coherent story when you know little, when there are fewer pieces to fit into the puzzle. Our comforting conviction that the world makes sense rests on a secure foundation: our almost unlimited ability to ignore our ignorance.

– Daniel Kahneman [1]

Chapter 1

Introduction

1.1 Coherent Multidimensional Spectroscopy

CMDS, coherent multidimensional spectroscopy

1.2 The CMDS Instrument

1.3 Scientific Software

Part I

Background

Chapter 2

Spectroscopy

In this chapter I lay out the foundations of spectroscopy.

2.1 Light

2.2 Light-Matter Interaction

Spectroscopic experiments all derive from the interaction of light and matter. Many material properties can be deduced by measuring the nature of this interaction.

Nonlinear spectroscopy relies upon higher-order terms in the light-matter interaction. In a generic system, each term is roughly ten times smaller than the last.

2.2.1 Representations

Many strategies have been introduced for diagrammatically representing the interaction of multiple electric fields in an experiment.

Circle Diagrams

Double-sided Feynman Diagrams

WMEL Diagrams

So-called wave mixing energy level (WMEL) diagrams are the most familiar way of representing spectroscopy for Wright group members. WMEL diagrams were first proposed by Lee and Albrecht in an appendix to their seminal work *A Unified View of Raman, Resonance Raman, and Fluorescence Spectroscopy* [2]. WMEL diagrams are drawn using the following rules.

1. The energy ladder is represented with horizontal lines - solid for real states and dashed for virtual states.
2. Individual electric field interactions are represented as vertical arrows. The arrows span the distance between the initial and final state in the energy ladder.
3. The time ordering of the interactions is represented by the ordering of arrows, from left to right.
4. Ket-side interactions are represented with solid arrows.
5. Bra-side interactions are represented with dashed arrows.
6. Output is represented as a solid wavy line.

Mukamel Diagrams

2.3 Linear Spectroscopy

2.3.1 Reflectivity

This derivation adapted from *Optical Processes in Semiconductors* by Jacques I. Pankove [3]. For normal incidence, the reflection coefficient is

$$R = \frac{(n-1)^2 + k^2}{(n+1)^2 + k^2} \tag{2.1}$$

Further derivation adapted from [4]. To extend reflectivity to a differential measurement

2.4 Coherent Multidimensional Spectroscopy

multiresonant coherent multidimensional spectroscopy

2.4.1 Three Wave

2.4.2 Four Wave

Fluorescence

Raman

2.4.3 Five Wave

2.4.4 Six Wave

multiple population-period transient spectroscopy (MUPPETS)

2.5 Strategies for CMDS

2.5.1 Homodyne vs. Heterodyne Detection

Two kinds of spectroscopies: 1) heterodyne 2) homodyne. Heterodyne techniques may be self heterodyne or explicitly heterodyned with a local oscillator.

In all heterodyne spectroscopies, signal goes as N. In all homodyne spectroscopies, signal goes as N^2. This literally means that homodyne signals go as the square of heterodyne signals, which is what we mean when we say that homodyne signals are intensity level and heterodyne signals are amplitude level.

Transient absorption, TA

2.5.2 Frequency vs. Time Domain

Time domain techniques become more and more difficult when large frequency bandwidths are needed. With very short, broad pulses:

- Non-resonant signal becomes brighter relative to resonant signal
- Pulse distortions become important.

This epi-CARS paper might have some useful discussion of non-resonant vs resonant for shorter and shorter pulses [5].

An excellent discussion of pulse distortion phenomena in broadband time-domain experiments was published by Spencer et al. [6].

Another idea in defense of frequency domain is for the case of power studies. Since time-domain pulses in-fact possess all colors in them they cannot be trusted as much at perturbative fluence. See that paper that Natalia presented...

2.5.3 Triply Electronically Enhanced Spectroscopy

Triply Electronically Enhanced (TrEE) spectroscopy has become the workhorse homodyne-detected 4WM experiment in the Wright Group.

2.5.4 Transient Absorbance Spectroscopy

Transient absorption (TA)

Quantitative TA

Transient absorbance (TA) spectroscopy is a self-heterodyned technique. Through chopping you can measure nonlinearities quantitatively much easier than with homodyne detected (or explicitly heterodyned) experiments.

Figure 2.1 diagrams the TA measurement for a generic sample. Here I show measurement of both the reflected and transmitted probe beam . . . not important in opaque (pyrite) or non-reflective (quantum dot) samples . . .

Typically one attempts to calculate the change in absorbance ΔA . . .

$$\begin{aligned}
\Delta A &= A_{\text{on}} - A_{\text{off}} && (2.2)\\
&= -\log_{10}\left(\frac{I_{\text{T}} + I_{\text{R}} + I_{\Delta\text{T}} + I_{\Delta\text{R}}}{I_0}\right) + \log\left(\frac{I_{\text{T}} + I_{\text{R}}}{I_0}\right) && (2.3)\\
&= -\left(\log_{10}(I_{\text{T}} + I_{\text{R}} + I_{\Delta\text{T}} + I_{\Delta\text{R}}) - \log_{10}(I_0)\right) + \left(\log_{10}(I_{\text{T}} + I_{\text{R}}) - \log_{10}(I_0)\right) && (2.4)\\
&= -\left(\log_{10}(I_{\text{T}} + I_{\text{R}} + I_{\Delta\text{T}} + I_{\Delta\text{R}}) - \log_{10}(I_{\text{T}} + I_{\text{R}})\right) && (2.5)\\
&= -\log_{10}\left(\frac{I_{\text{T}} + I_{\text{R}} + I_{\Delta\text{T}} + I_{\Delta\text{R}}}{I_{\text{T}} + I_{\text{R}}}\right) && (2.6)
\end{aligned}$$

Equation 2.6 simplifies beautifully if reflectivity is negligible ...

Now I define a variable for each experimental measurable:

V_{T}	voltage recorded from transmitted beam, without pump
V_{R}	voltage recorded from reflected beam, without pump
$V_{\Delta\text{T}}$	change in voltage recorded from transmitted beam due to pump
$V_{\Delta\text{R}}$	change in voltage recorded from reflected beam due to pump

We will need to calibrate using a sample with a known transmisivity and reflectivity constant:

$V_{\text{T, ref}}$	voltage recorded from transmitted beam, without pump
$V_{\text{R, ref}}$	voltage recorded from reflected beam, without pump
$\mathcal{T}_{\text{ref}}$	transmissivity
$\mathcal{R}_{\text{ref}}$	reflectivity

Define two new proportionality constants...

$$\begin{aligned}
C_{\text{T}} &\equiv \frac{\mathcal{T}}{V_{\text{T}}} && (2.7)\\
C_{\text{R}} &\equiv \frac{\mathcal{R}}{V_{\text{R}}} && (2.8)
\end{aligned}$$

These are explicitly calibrated (as a function of probe color) prior to the experiment using the calibration sample.

Given the eight experimental measurables (V_{T}, V_{R}, $V_{\Delta\text{T}}$, $V_{\Delta\text{R}}$, $V_{\text{T, ref}}$, $V_{\text{R, ref}}$, $\mathcal{T}_{\text{ref}}$, $\mathcal{R}_{\text{ref}}$) I can express

all of the intensities in Equation 2.6 in terms of I_0.

$$C_T = \frac{\mathcal{T}_{ref}}{V_{T,\,ref}} \tag{2.9}$$

$$C_R = \frac{\mathcal{R}_{ref}}{V_{R,\,ref}} \tag{2.10}$$

$$I_T = I_0 C_T V_T \tag{2.11}$$

$$I_R = I_0 C_R V_R \tag{2.12}$$

$$I_{\Delta T} = I_0 C_T V_{\Delta T} \tag{2.13}$$

$$I_{\Delta R} = I_0 C_R V_{\Delta R} \tag{2.14}$$

Wonderfully, the I_0 cancels when plugged back in to Equation 2.6, leaving a final expression for ΔA that only depends on my eight measurables.

$$\Delta A = -\log_{10}\left(\frac{C_T(V_T + V_{\Delta T}) + C_R(V_R + V_{\Delta R})}{C_T V_T + C_R V_R}\right) \tag{2.15}$$

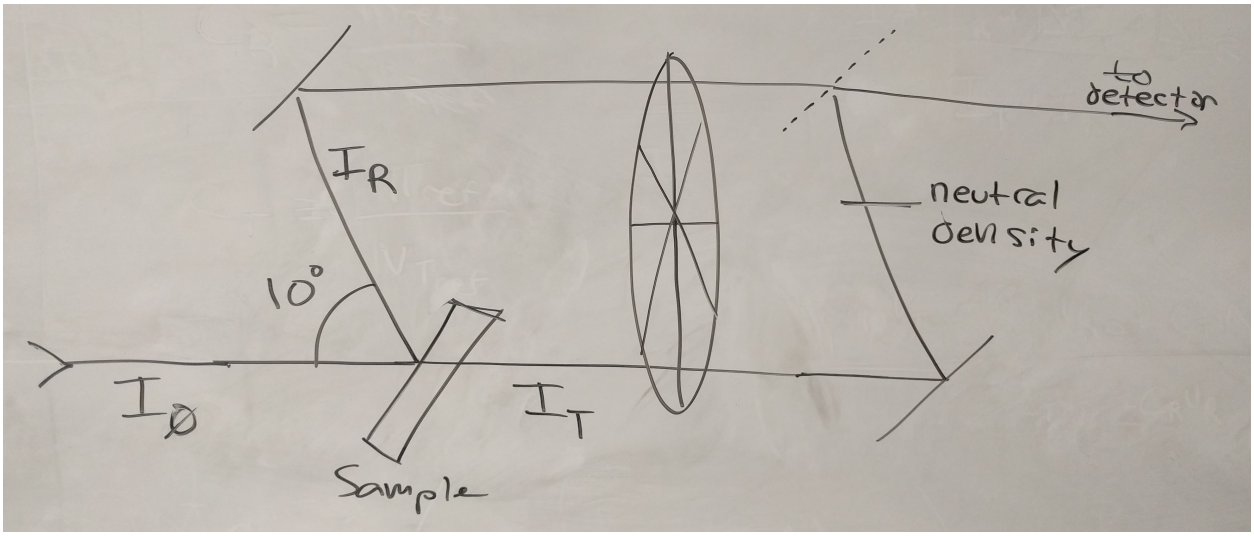

Figure 2.1: CAPTION TODO

2.5.5 Cross Polarized TrEE

2.5.6 Pump-TrEE-Probe

Pump TrEE probe (PTP).

2.6 Instrumental Response Function

The instrumental response function (IRF) is a classic concept in analytical science. Defining IRF becomes complex with instruments as complex as these, but it is still useful to attempt.

It is particularly useful to define bandwidth.

2.6.1 Time Domain

I will use four wave mixing to extract the time-domain pulse-width. I use a driven signal *e.g.* near infrared carbon tetrachloride response. I'll homodyne-detect the output. In my experiment I'm moving pulse 1 against pulses 2 and 3 (which are coincident).

The driven polarization, P, goes as the product of my input pulse *intensities*:

$$P(T) = I_1(t - T) \times I_2(t) \times I_3(t) \tag{2.16}$$

In our experiment we are convolving I_1 with $I_2 \times I_3$. Each pulse has an *intensity-level* width, σ_1, σ_2, and σ_3. $I_2 \times I_3$ is itself a Gaussian, and

$$\sigma_{I_2 I_3} = \ldots \tag{2.17}$$

$$= \sqrt{\frac{\sigma_2^2 \sigma_3^2}{\sigma_2^2 + \sigma_3^2}}. \tag{2.18}$$

The width of the polarization (across T) is therefore

$$\begin{aligned} \sigma_P &= \sqrt{\sigma_1^2 + \sigma_{I_2 I_3}^2} && (2.19) \\ &= \ldots && (2.20) \\ &= \sqrt{\frac{\sigma_1^2 + \sigma_2^2 \sigma_3^2}{\sigma_1^2 + \sigma_2^2}}. && (2.21) \end{aligned}$$

I assume that all of the pulses have the same width. I_1, I_2, and I_3 are identical Gaussian functions with FWHM σ. In this case, Equation 2.21 simplifies to

$$\begin{aligned} \sigma_P &= \sqrt{\frac{\sigma^2 + \sigma^2 \sigma^2}{\sigma^2 + \sigma^2}} && (2.22) \\ &= \ldots && (2.23) \\ &= \sigma \sqrt{\frac{3}{2}} && (2.24) \end{aligned}$$

Finally, since we measure σ_P and wish to extract σ:

$$\sigma = \sigma_P \sqrt{\frac{2}{3}} \quad (2.25)$$

Again, all of these widths are on the *intensity* level.

2.6.2 Frequency Domain

We can directly measure σ (the width on the intensity-level) in the frequency domain using a spectrometer. A tune test contains this information.

2.6.3 Time-Bandwidth Product

For a Gaussian, approximately 0.441

Chapter 3

Materials

"Kroemer's Lemma of Proven Ignorance": If, in discussing a semiconductor problem, you cannot draw an Energy Band Diagram, this shows that you don't know what you are talking about, If you can draw one, but don't, then your audience won't know what you are talking about.

Chapter 4

Disentangling material and instrument response

Ultrafast spectroscopy is often collected in the mixed frequency/time domain, where pulse durations are similar to system dephasing times. In these experiments, expectations derived from the familiar driven and impulsive limits are not valid. This work simulates the mixed-domain Four Wave Mixing response of a model system to develop expectations for this more complex field-matter interaction. We explore frequency and delay axes. We show that these line shapes are exquisitely sensitive to excitation pulse widths and delays. Near pulse overlap, the excitation pulses induce correlations which resemble signatures of dynamic inhomogeneity. We describe these line shapes using an intuitive picture that connects to familiar field-matter expressions. We develop strategies for distinguishing pulse-induced correlations from true system inhomogeneity. These simulations provide a foundation for interpretation of ultrafast experiments in the mixed domain.

4.1 Introduction

Ultrafast spectroscopy is based on using nonlinear interactions, created by multiple ultrashort ($10^{-9} - 10^{-15}$s) pulses, to resolve spectral information on timescales as short as the pulses themselves.[**Rentzepis1970**,

Mukamel2000] The ultrafast specta can be collected in the time domain or the frequency domain.[**Park1998**]

Time-domain methods scan the pulse delays to resolve the free induction decay (FID).[**Gallagher1998**] The Fourier Transform of the FID gives the ultrafast spectrum. Ideally, these experiments are performed in the impulsive limit where FID dominates the measurement. FID occurs at the frequency of the transition that has been excited by a well-defined, time-ordered sequence of pulses. Time-domain methods are compromised when the dynamics occur on faster time scales than the ultrafast excitation pulses. As the pulses temporally overlap, FID from other pulse time-orderings and emission driven by the excitation pulses both become important. These factors are responsible for the complex "coherent artifacts" that are often ignored in pump-probe and related methods.[**Lebedev2007**, **Vardeny1981**, **Joffre1988**, **Pollard1992**] Dynamics faster than the pulse envelopes are best measured using line shapes in frequency domain methods.

Frequency-domain methods scan pulse frequencies to resolve the ultrafast spectrum directly.[**Druet1979**, **Oudar1980**] Ideally, these experiments are performed in the driven limit where the steady state dominates the measurement. In the driven limit, all time-orderings of the pulse interactions are equally important and FID decay is negligible. The output signal is driven at the excitation pulse frequencies during the excitation pulse width. Frequency-domain methods are compromised when the spectral line shape is narrower than the frequency bandwidth of the excitation pulses. Dynamics that are slower than the pulse envelopes can be measured in the time domain by resolving the phase oscillations of the output signal during the entire FID decay.

There is also the hybrid mixed-time/frequency-domain approach, where pulse delays and pulse frequencies are both scanned to measure the system response. This approach is uniquely suited for experiments where the dephasing time is comparable to the pulse durations, so that neither frequency-domain nor time-domain approaches excel on their own.[**Oudar1980**, **Wright1997a**, **Wright1991**] In this regime, both FID and driven processes are important.[**Pakoulev2006**] Their relative importance depends on pulse frequencies and delays. Extracting the correct spectrum from the measurement then requires a more complex analysis that explicitly treats the excitation pulses and the different time-orderings.[**Pakoulev2007**, **Kohler2014**, **Gelin2009a**] Despite these complications, mixed-domain methods have a practical advantage: the dual frequency- and delay-scanning capabilities allow these

methods to address a wide variety of dephasing rates.

The relative importance of FID and driven processes and the changing importance of different coherence pathways are important factors for understanding spectral features in all ultrafast methods. These methods include partially-coherent methods involving intermediate populations such as pump-probe,[**Hamm2000**] transient grating,[**Salcedo1978**, **Fourkas1992**, **Fourkas1992a**] transient absorption/reflection,[**Au Bakker2002**] photon echo,[**DeBoeij1996**, **Patterson1984**, **Tokmakoff1995**] two dimensional-infrared spectroscopy (2D-IR),[**Hamm1999**, **Asplund2000**, **Zanni2001**] 2D-electronic spectroscopy (2D-ES),[**Hybl2001a**, **Brixner2004**] and three pulse photon echo peak shift (3PEPS)[**Emde1998**, **DeBoeij1996**, **DeBoeij1995**, **Cho1992**, **Passino1997**] spectroscopies. These methods also include fully-coherent methods involving only coherences such as Stimulated Raman Spectroscopy (SRS),[**Yoon2005**, **McCamant2005**] Doubly Vibrationally Enhanced (DOVE),[**Zhao1999**, **Zhao1999a**, **Zhao2000**, **Meyer2003**, **Donaldson2007**, **Donaldson2008**, **Fournier2008**] Triply Resonant Sum Frequency (TRSF),[**Boyle2013a**, **Boyle2013**, **Boyle2014**] Sum Frequency Generation (SFG)[**Lagutchev2007**], Coherent Anti-Stokes Raman Spectroscopy (CARS)[**Carlson1990b**, **Carlson1990a**, **Carlson1991**] and other coherent Raman methods[**Steehler1985**].

This paper focuses on understanding the nature of the spectral changes that occur in Coherent Multidimensional Spectroscopy (CMDS) as experiments transition between the two limits of frequency- and time-domain methods. CMDS is a family of spectroscopies that use multiple delay and/or frequency axes to extract homogeneous and inhomogeneous broadening, as well as detailed information about spectral diffusion and chemical changes.[**Kwac2003**, **Wright2016**] For time-domain CMDS (2D-IR, 2D-ES), the complications that occur when the impulsive approximation does not strictly hold has only recently been addressed.[**Erlik2017**, **Smallwood2016**]

Frequency-domain CMDS methods, referred to herein as multi-resonant CMDS (MR-CMDS), have similar capabilities for measuring homogeneous and inhomogeneous broadening. Although these experiments are typically described in the driven limit,[**Gallagher1998**, **Fourkas1992**, **Fourkas1992a**] many of the experiments involve pulse widths that are comparable to the widths of the system.[**Meyer2003**, **Donaldson2007**, **Pakoulev2009**, **Zhao1999**, **Czech2015**, **Kohler2014**] MR-CMDS then becomes a mixed-domain experiment whereby resonances are characterized with marginal resolution in both frequency and time. For example, DOVE spectroscopy involves three different pathways[**Wright2003**]

whose relative importance depends on the relative importance of FID and driven responses.[**Donaldson2010**] In the driven limit, the DOVE line shape depends on the difference between the first two pulse frequencies so the line shape has a diagonal character that mimics the effects of inhomogeneous broadening. In the FID limit where the coherence frequencies are defined instead by the transition, the diagonal character is lost. Understanding these effects is crucial for interpreting experiments, yet these effects have not been characterized for MR-CMDS.

This work considers the third-order MR-CMDS response of a 3-level model system using three ultrafast excitation beams with the commonly used four-wave mixing (FWM) phase-matching condition, $\vec{k}_{\text{out}} = \vec{k}_1 - \vec{k}_2 + \vec{k}_{2'}$. Here, the subscripts represent the excitation pulse frequencies, ω_1 and $\omega_2 = \omega_{2'}$. These experimental conditions were recently used to explore line shapes of excitonic systems,[**Kohler2014**, **Czech2015**] and have been developed on vibrational states as well.[**Meyer2004**] Although MR-CMDS forms the context of this model, the treatment is quite general because the phase matching condition can describe any of the spectroscopies mentioned above with the exception of SFG and TRSF, for which the model can be easily extended. We numerically simulate the MR-CMDS response with pulse durations at, above, and below the system coherence time. To highlight the role of pulse effects, we build an interpretation of the full MR-CMDS response by first showing how finite pulses affect the evolution of a coherence, and then how finite pulses affect an isolated third-order pathway. When considering the full MR-CMDS response, we show that spectral features change dramatically as a function of delay, even for a homogeneous system with elementary dynamics. Importantly, the line shape can exhibit correlations that mimic inhomogeneity, and the temporal evolution of this line shape can mimic spectral diffusion. We identify key signatures that can help differentiate true inhomogeneity and spectral diffusion from these measurement artifacts.

4.2 Theory

We consider a simple three-level system (states $n = 0, 1, 2$) that highlights the multidimensional line shape changes resulting from choices of the relative dephasing and detuning of the system and the temporal and spectral widths of the excitation pulses. For simplicity, we will ignore population relaxation

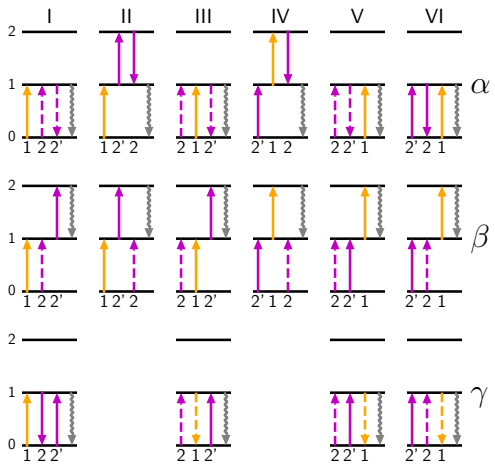

Figure 4.1: The sixteen triply-resonant Liouville pathways for the third-order response of the system used here. Time flows from left to right. Each excitation is labeled by the pulse stimulating the transition; excitatons with ω_1 are yellow, excitations with $\omega_2 = \omega_{2'}$ are purple, and the final emission is gray.

effects: $\Gamma_{11} = \Gamma_{00} = 0$.

The electric field pulses, $\{E_l\}$, are given by:

$$E_l(t; \omega_l, \tau_l, \vec{k}_l \cdot z) = \frac{1}{2}\left[c_l(t-\tau_l)e^{i\vec{k}_l \cdot z}e^{-i\omega_l(t-\tau_l)} + c.c.\right], \tag{4.1}$$

where ω_l is the field carrier frequency, $\vec{k}_l$ is the wavevector, τ_l is the pulse delay, and c_l is a slowly varying envelope. In this work, we assume normalized (real-valued) Gaussian envelopes:

$$c_l(t) = \frac{1}{\Delta_t}\sqrt{\frac{2\ln 2}{2\pi}}\exp\left(-\ln 2\left[\frac{t}{\Delta_t}\right]^2\right), \tag{4.2}$$

where Δ_t is the temporal FWHM of the envelope intensity. We neglect non-linear phase effects such as chirp so the FWHM of the frequency bandwidth is transform limited: $\Delta_\omega \Delta_t = 4\ln 2 \approx 2.77$, where Δ_ω is the spectral FWHM (intensity scale).

The Liouville-von Neumann Equation propagates the density matrix, $\boldsymbol{\rho}$:

$$\frac{d\boldsymbol{\rho}}{dt} = -\frac{i}{\hbar}\left[\mathbf{H_0} + \boldsymbol{\mu} \cdot \sum_{l=1,2,2'} E_l(t), \boldsymbol{\rho}\right] + \mathbf{\Gamma}\boldsymbol{\rho}. \tag{4.3}$$

Here $\mathbf{H_0}$ is the time-independent Hamiltonian, $\boldsymbol{\mu}$ is the dipole superoperator, and $\mathbf{\Gamma}$ contains the pure dephasing rate of the system. We perform the standard perturbative expansion of Equation 4.3 to third order in the electric field interaction[**mukamel1995principles**, **Yee1978**, **Oudar1980**, **Armstrong1962**, **Schweigert2008**] and restrict ourselves only to the terms that have the correct spatial wave vector $\vec{k}_{\text{out}} = \vec{k}_1 - \vec{k}_2 + \vec{k}_{2'}$. This approximation narrows the scope to sets of three interactions, one from each field, that result in the correct spatial dependence. The set of three interactions have $3! = 6$ unique time-ordered sequences, and each time-ordering produces either two or three unique system-field interactions for our system, for a total of sixteen unique system-field interaction sequences, or Liouville pathways, to consider. Fig. 4.1 shows these sixteen pathways as Wave Mixing Energy Level (WMEL) diagrams[**Lee1985**].

We first focus on a single interaction in these sequences, where an excitation pulse, x, forms ρ_{ij} from

ρ_{ik} or ρ_{kj}. For brevity, we use $\hbar = 1$ and abbreviate the initial and final density matrix elements as ρ_i and ρ_f, respectively. Using the natural frequency rotating frame, $\tilde{\rho}_{ij} = \rho_{ij} e^{-i\omega_{ij}t}$, the formation of ρ_f using pulse x is written as

$$\begin{aligned}\frac{d\tilde{\rho}_f}{dt} =& -\Gamma_f \tilde{\rho}_f \\ &+ \frac{i}{2}\lambda_f \mu_f c_x(t-\tau_x) e^{i\kappa_f\left(\vec{k}_x\cdot z+\omega_x\tau_x\right)} e^{i\kappa_f\Omega_{fx}t}\tilde{\rho}_i(t),\end{aligned} \tag{4.4}$$

where $\Omega_{fx} = \kappa_f^{-1}\omega_f - \omega_x (= |\omega_f| - \omega_x)$ is the detuning, ω_f is the transition frequency of the i^{th} transition, μ_f is the transition dipole, and Γ_f is the dephasing/relaxation rate for ρ_f. The λ_f and κ_f parameters describe the phases of the interaction: $\lambda_f = +1$ for ket-side transitions and -1 for bra-side transitions, and κ_f depends on whether ρ_f is formed via absorption ($\kappa_f = \lambda_f$) or emission ($\kappa_f = -\lambda_f$).[1] In the following equations we neglect spatial dependence ($z = 0$).

Equation 4.4 forms the basis for our simulations. It provides a general expression for arbitrary values of the dephasing rate and excitation pulse bandwidth. The integral solution is

$$\begin{aligned}\tilde{\rho}_f(t) =& \frac{i}{2}\lambda_f \mu_f e^{i\kappa_f\omega_x\tau_x} e^{i\kappa_f\Omega_{fx}t} \\ &\times \int_{-\infty}^{\infty} c_x(t-u-\tau_x)\tilde{\rho}_i(t-u)\Theta(u) \\ &\times e^{-(\Gamma_f + i\kappa_f\Omega_{fx})u} du,\end{aligned} \tag{4.5}$$

where Θ is the Heaviside step function. Equation 4.5 becomes the steady state limit expression when $\Delta_t\,|\Gamma_f + i\kappa_f\Omega_{fx}| \gg 1$, and the impulsive limit expression results when $\Delta_t\,|\Gamma_f + i\kappa_f\Omega_{fx}| \ll 1$. Both limits are important for understanding the multidimensional line shape changes discussed in this paper. The steady state and impulsive limits of Equation 4.5 are discussed in Appendix 4.3.1.

Fig. 4.2 gives an overview of the simulations done in this work. Fig. 4.2a shows an excitation pulse (gray-shaded) and examples of a coherent transient for three different dephasing rates. The color bindings to dephasing rates introduced in Fig. 4.2a will be used consistently throughout this work. Our simulations use systems with dephasing rates quantified relative to the pulse duration: $\Gamma_{10}\Delta_t = 0.5, 1,$ or 2. The temporal axes are normalized to the pulse duration, Δ_t. The $\Gamma_{10}\Delta_t = 2$ transient is mostly

[1] κ_f also has a direct relationship to the phase matching relationship: for transitions with E_2, $\kappa_f = 1$, and for E_1 or $E_{2'}$, $\kappa_f = -1$.

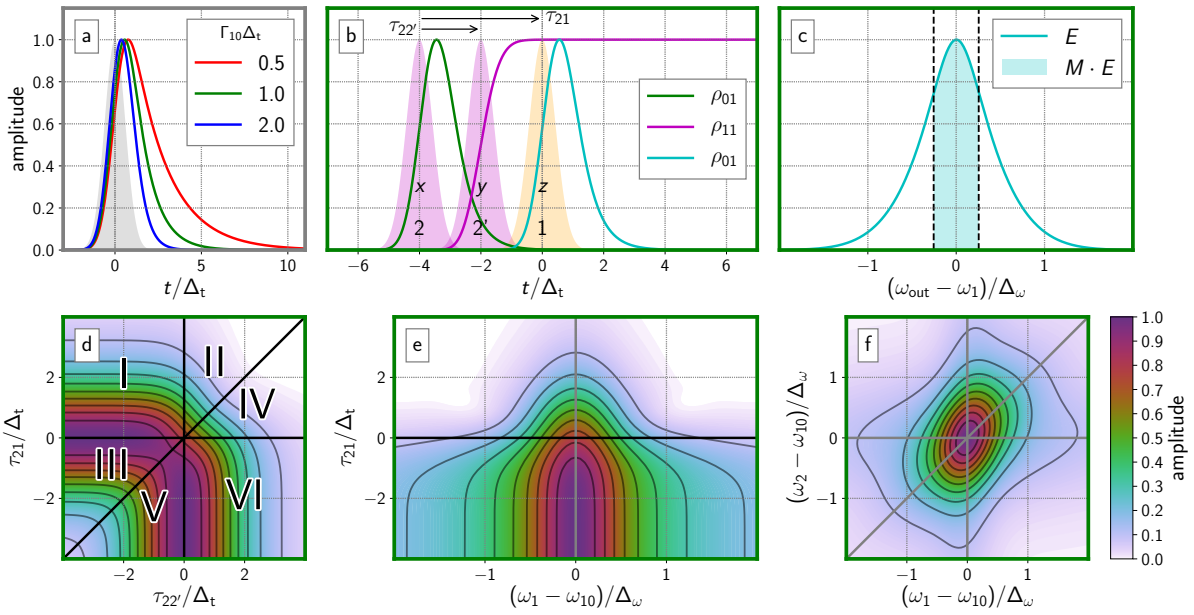

Figure 4.2: Overview of the MR-CMDS simulation. (a) The temporal profile of a coherence under pulsed excitation depends on how quickly the coherence dephases. In all subsequent panes, the relative dephasing rate is kept constant at $\Gamma_{10}\Delta_t = 1$. (b) Simulated evolution of the density matrix elements of a third-order Liouville pathway $V\gamma$ under fully resonant excitation. Pulses can be labeled both by their time of arrival (x,y,z) and by the lab lasers used to stimulate the transitions (2,2′,1). The final coherence (teal) creates the output electric field. (c) The frequency profile of the output electric field is filtered by a monochromator gating function, $M(\omega)$, and the passed components (shaded) are measured. (d-f) Signal is viewed against two laser parameters, either as 2D delay (d), mixed delay-frequency (e), or 2D frequency plots (f). The six time-orderings are labeled in (d) to help introduce our delay convention.

driven by the excitation pulse while $\Gamma_{10}\Delta_t = 0.5$ has a substantial free induction decay (FID) component at late times. Fig. 4.2b shows a pulse sequence (pulses are shaded orange and pink) and the resulting system evolution of pathway $V\gamma$ ($00 \xrightarrow{2} 01 \xrightarrow{2'} 11 \xrightarrow{1} 10 \xrightarrow{\text{out}} 00$) with $\Gamma_{10}\Delta_t = 1$. The final polarization (teal) is responsible for the emitted signal, which is then passed through a frequency bandpass filter to emulate monochromator detection (Fig. 4.2c). The resulting signal is explored in 2D delay space (Fig. 4.2d), 2D frequency space (Fig. 4.2f), and hybrid delay-frequency space (Fig. 4.2e). The detuning frequency axes are also normalized by the pulse bandwidth, Δ_ω.

We now consider the generalized Liouville pathway $L : \rho_0 \xrightarrow{x} \rho_1 \xrightarrow{y} \rho_2 \xrightarrow{z} \rho_3 \xrightarrow{\text{out}} \rho_4$, where x, y, and z denote properties of the first, second, and third pulse, respectively, and indices 0, 1, 2, 3, and 4 define the properties of the ground state, first, second, third, and fourth density matrix elements, respectively. Fig. 4.2b demonstrates the correspondence between x, y, z notation and 1, 2, $2'$ notation for the laser pulses with pathway $V\gamma$.[2]

The electric field emitted from a Liouville pathway is proportional to the polarization created by the third-order coherence:

$$E_L(t) = i\mu_4\rho_3(t). \tag{4.6}$$

Equation 4.6 assumes perfect phase-matching and no pulse distortions through propagation. Equation 4.5 shows that the output field for this Liouville pathway is

$$\begin{aligned} E_L(t) =& \frac{i}{8}\lambda_1\lambda_2\lambda_3\mu_1\mu_2\mu_3\mu_4 e^{i(\kappa_1\omega_x\tau_x+\kappa_2\omega_y\tau_y+\kappa_3\omega_z\tau_z)}e^{-i(\kappa_3\omega_z+\kappa_2\omega_y+\kappa_1\omega_x)t} \\ &\times \iiint_{-\infty}^{\infty} c_z(t-u-\tau_z)c_y(t-u-v-\tau_y)c_x(t-u-v-w-\tau_x)R_L(u,v,w)dw\ dv\ du, \end{aligned} \tag{4.7}$$

$$R_L(u,v,w) = \Theta(w)e^{-(\Gamma_1+i\kappa_1\Omega_{1x})w}\Theta(v)e^{-(\Gamma_2+i[\kappa_1\Omega_{1x}+\kappa_2\Omega_{2y}])v}\Theta(u)e^{-(\Gamma_3+i[\kappa_1\Omega_{1x}+\kappa_2\Omega_{2y}+\kappa_3\Omega_{3z}])u}, \tag{4.8}$$

where R_L is the third-order response function for the Liouville pathway. The total electric field will be

[2] For elucidation of the relationship between the generalized Liouville pathway notation and the specific parameters for each Liouville pathway, see Table S1 in the Supplementary Information.

the superposition of all the Liouville pathways:

$$E_{\text{tot}} = \sum_{L} E_L(t). \tag{4.9}$$

For the superposition of Equation 4.9 to be non-canceling, certain symmetries between the pathways must be broken. In general, this requires one or more of the following inequalities: $\Gamma_{10} \neq \Gamma_{21}$, $\omega_{10} \neq \omega_{21}$, and/or $\sqrt{2}\mu_{10} \neq \mu_{21}$. Our simulations use the last inequality, which is important in two-level systems ($\mu_{21} = 0$) and in systems where state-filling dominates the non-linear response, such as in semiconductor excitons. The exact ratio between μ_{10} and μ_{21} affects the absolute amplitude of the field, but does not affect the multidimensional line shape. Importantly, the dipole inequality does not break the symmetry of double quantum coherence pathways (time-orderings II and IV), so such pathways are not present in our analysis.

In MR-CMDS, a monochromator resolves the driven output frequency from other nonlinear output frequencies, which in our case is $\omega_m = \omega_1 - \omega_2 + \omega_{2'} = \omega_1$. The monochromator can also enhance spectral resolution, as we show in Section 4.4.1. In this simulation, the detection is emulated by transforming $E_{\text{tot}}(t)$ into the frequency domain, applying a narrow bandpass filter, $M(\omega)$, about ω_1, and applying amplitude-scaled detection:

$$S_{\text{tot}}(\omega_1, \omega_2, \tau_{21}, \tau_{22'}) = \sqrt{\int \left| M(\omega - \omega_1) E_{\text{tot}}(\omega) \right|^2 d\omega}, \tag{4.10}$$

where $E_{\text{tot}}(\omega)$ denotes the Fourier transform of $E_{\text{tot}}(t)$ (see Fig. 4.2c). For M we used a rectangular function of width $0.408\Delta_\omega$. The arguments of S_{tot} refer to the *experimental* degrees of freedom. The signal delay dependence is parameterized with the relative delays τ_{21} and $\tau_{22'}$, where $\tau_{nm} = \tau_n - \tau_m$ (see Fig. 4.2b). Table S1 summarizes the arguments for each Liouville pathway. Fig. 4.2f shows the 2D (ω_1, ω_2) S_{tot} spectrum resulting from the pulse delay times represented in Fig. 4.2b.

4.2.1 Inhomogeneity

Inhomogeneity is isolated in CMDS through both spectral signatures, such as line-narrowing[**Besemann2004**, **Oudar1980**, **Carlson1990**, **Riebe1988**, **Steehler1985**], and temporal signatures, such as photon echoes[**Weiner1985**, **Agarwal2002**]. We simulate the effects of static inhomogeneous broadening by convolving the homogeneous response with a Gaussian distribution function. Further details of the convolution are in Appendix 4.3.2. Dynamic broadening effects such as spectral diffusion are beyond the scope of this work.

4.3 Methods

A matrix representation of differential equations of the type in Equation 4.7 was numerically integrated for parallel computation of Liouville elements (see SI for details).[**Dick1983**, **Gelin2005**] The lower bound of integration was $2\Delta_t$ before the first pulse, and the upper bound was $5\Gamma_{10}^{-1}$ after the last pulse, with step sizes much shorter than the pulse durations. Integration was performed in the FID rotating frame; the time steps were chosen so that both the system-pulse difference frequencies and the pulse envelope were well-sampled.

The following simulations explore the four-dimensional $(\omega_1, \omega_2, \tau_{21}, \tau_{22'})$ variable space. Both frequencies are scanned about the resonance, and both delays are scanned about pulse overlap. We explored the role of sample dephasing rate by calculating signal for systems with dephasing rates such that $\Gamma_{10}\Delta_t = 0.5, 1$, and 2. Inhomogeneous broadening used a spectral FWHM, Δ_{inhom}, that satisfied $\Delta_{\text{inhom}}/\Delta_\omega = 0, 0.5, 1$, and 2 for the three dephasing rates. For all these dimensions, both $\rho_3(t; \omega_1, \omega_2, \tau_{21}, \tau_{22'})$ and $S_{\text{tot}}(\omega_1, \omega_2, \tau_{21}, \tau_{22'})$ are recorded for each unique Liouville pathway. Our simulations were done using the open-source SciPy library.[**Oliphant2007**]

4.3.1 Characteristics of Driven and Impulsive Response

The changes in the spectral line shapes described in this work are best understood by examining the driven/continuous wave (CW) and impulsive limits of Equations 4.5 and 4.7. The driven limit is achieved when pulse durations are much longer than the response function dynamics: $\Delta_t \left|\Gamma_f + i\kappa_f\Omega_{fx}\right| \gg 1$. In this limit, the system will adopt a steady state over excitation: $d\rho/dt \approx 0$. Neglecting phase factors, the driven solution to Equation 4.5 will be

$$\tilde{\rho}_f(t) = \frac{\lambda_f\mu_f}{2}\frac{c_x(t-\tau_x)e^{i\kappa_f\Omega_{fx}t}}{\kappa_f\Omega_{fx}}\tilde{\rho}_i(t). \tag{4.11}$$

The frequency and temporal envelope of the excitation pulse controls the coherence time evolution, and the relative amplitude and phase of the coherence is directly related to detuning from resonance.

The impulsive limit is achieved when the excitation pulses are much shorter than response function dynamics: $\Delta_t \left|\Gamma_f + i\kappa_f\Omega_{fx}\right| \ll 1$. The full description of the temporal evolution has two separate expressions: one for times when the pulse is interacting with the system, and one for times after pulse interaction. Both expressions are important when describing CMDS experiments.

For times after the pulse interaction, $t \gtrsim \tau_x + \Delta_t$, the field-matter coupling is negligible. The evolution for these times, on resonance, is given by

$$\tilde{\rho}_f(t) = \frac{i\lambda_f\mu_f}{2}\tilde{\rho}_i(\tau_x)\int c_x(u)du\ e^{-\Gamma_f(t-\tau_x)}. \tag{4.12}$$

This is classic free induction decay (FID) evolution: the system evolves at its natural frequency and decays at rate Γ_f. It is important to note that, while this expression is explicitly derived from the impulsive limit, FID behavior is not exclusive to impulsive excitation, as we have defined it. A latent FID will form if the pulse vanishes at a fast rate relative to the system dynamics.

For evaluating times near pulse excitation, $t \lesssim \tau_x + \Delta_t$, we implement a Taylor expansion in the response function about zero: $e^{-(\Gamma_f + i\kappa_f\Omega_{fx})u} = 1 - (\Gamma_f + i\kappa_f\Omega_{fx})u + \cdots$. Our impulsive criterion requires that a low order expansion will suffice; it is instructive to consider the result of the first order expansion of

Equation 4.5:

$$\begin{aligned}\tilde{\rho}_f(t) =& \frac{i\lambda_f\mu_f}{2} e^{-i\kappa_f\omega_x\tau_x} e^{-i\kappa_f\Omega_{fx}t}\tilde{\rho}_i(\tau_x) \\ &\times \Bigg[(1-(\Gamma_f + i\kappa_f\Omega_{fx})(t-\tau_x)) \int_{-\infty}^{t-\tau_x} c_x(u)du \\ &+ (\Gamma_f + i\kappa_f\Omega_{fx}) \int_{-\infty}^{t-\tau_x} c_x(u)u\ du \Bigg].\end{aligned} \tag{4.13}$$

During this time $\tilde{\rho}_f$ builds up roughly according to the integration of the pulse envelope. The build-up is integrated because the pulse transfers energy before appreciable dephasing or detuning occurs. Contrary to the expectation of impulsive evolution, the evolution of $\tilde{\rho}_f$ is explicitly affected by the pulse frequency, and the temporal profile evolves according to the pulse.

It is important to recognize that the impulsive limit is defined not only by having slow relaxation relative to the pulse duration, but also by small detuning relative to the pulse bandwidth (as is stated in the inequality). As detuning increases, the higher orders of the response function Taylor expansion will be needed to describe the rise time, and the driven limit of Equation 4.11 will become valid. The details of this build-up time can often be neglected in impulsive approximations because build-up contributions are often negligible in analysis; the period over which the initial excitation occurs is small in comparison to the free evolution of the system. The build-up behavior can be emphasized by the measurement, which makes Equation 4.13 important.

We now consider full Liouville pathways in the impulsive and driven limits of Equation 4.7. For the driven limit, Equation 4.7 can be reduced to

$$\begin{aligned}E_L(t) =& \frac{1}{8}\lambda_1\lambda_2\lambda_3\mu_1\mu_2\mu_3\mu_4 e^{-i(\kappa_1\omega_x\tau_x+\kappa_2\omega_y\tau_y+\kappa_3\omega_z\tau_z)} \\ &\times e^{i(\kappa_3\omega_z+\kappa_2\omega_y+\kappa_1\omega_x)t} \\ &\times c_z(t-\tau_z)c_y(t-\tau_y)c_x(t-\tau_x) \\ &\times \frac{1}{\kappa_1\Omega_{1x}-i\Gamma_1}\frac{1}{\kappa_1\Omega_{1x}+\kappa_2\Omega_{2y}-i\Gamma_2} \\ &\times \frac{1}{\kappa_1\Omega_{1x}+\kappa_2\Omega_{2y}+\kappa_3\Omega_{3z}-i\Gamma_3}.\end{aligned} \tag{4.14}$$

It is important to note that the signal depends on the multiplication of all the fields; pathway discrimina-

tion based on pulse time-ordering is not achievable because polarizations exists only when all pulses are overlapped. This limit is the basis for frequency-domain techniques. Frequency axes, however, are not independent because the system is forced to the laser frequency and influences the resonance criterion for subsequent excitations. As an example, observe that the first two resonant terms in Equation 4.14 are maximized when $\omega_x = |\omega_1|$ and $\omega_y = |\omega_2|$. If ω_x is detuned by some value ε, however, the occurrence of the second resonance shifts to $\omega_y = |\omega_2| + \varepsilon$, effectively compensating for the ω_x detuning. This shifting of the resonance results in 2D line shape correlations.

If the pulses do not temporally overlap ($\tau_x + \Delta_t \lesssim \tau_y + \Delta_t \lesssim \tau_z + \Delta_t \lesssim t$), then the impulsive solution to the full Liouville pathway of Equation 4.7 is

$$\begin{aligned} E_L(t) =& \frac{i}{8}\lambda_1\lambda_2\lambda_3\mu_1\mu_2\mu_3\mu_4 e^{i(\omega_1+\omega_2+\omega_3)t} \\ & \times \int c_x(w)dw \int c_y(v)dv \int c_z(u)du \\ & \times e^{-\Gamma_1(\tau_y-\tau_x)} e^{-\Gamma_2(\tau_z-\tau_y)} e^{-\Gamma(t-\tau_z)}. \end{aligned} \tag{4.15}$$

Pathway discrimination is demonstrated here because the signal is sensitive to the time-ordering of the pulses. This limit is suited for delay scanning techniques. The emitted signal frequency is determined by the system and can be resolved by scanning a monochromator.

The driven and impulsive limits can qualitatively describe our simulated signals at certain frequency and delay combinations. Of the three expressions, the FID limit most resembles signal when pulses are near resonance and well-separated in time (so that build-up behavior is negligible). The build-up limit approximates well when pulses are near-resonant and arrive together (so that build-up behavior is emphasized). The driven limit holds for large detunings, regardless of delay.

4.3.2 Convolution Technique for Inhomogeneous Broadening

Here we describe how to transform the data of a single reference oscillator signal to that of an inhomogeneous distribution. The oscillators in the distribution are allowed have arbitrary energies for their states, which will cause frequency shifts in the resonances. To show this, we start with a modified, but

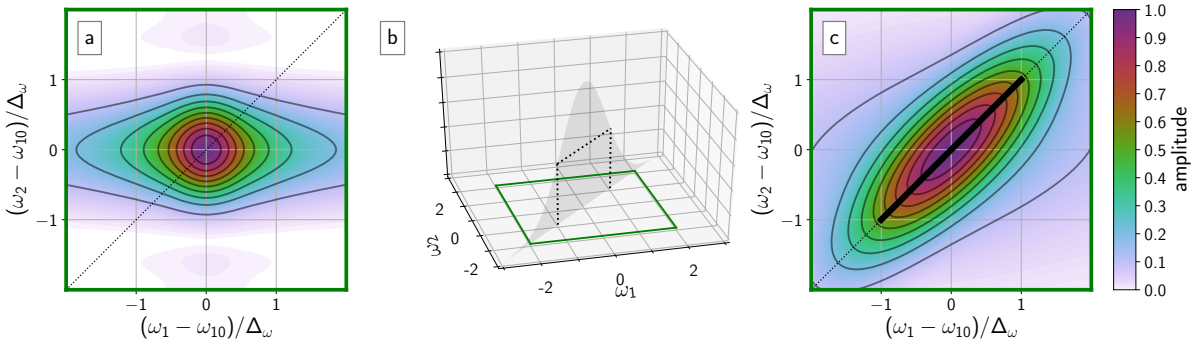

Figure 4.3: Overview of the convolution. (a) The homogeneous line shape. (b) The distribution function, K, mapped onto laser coordinates. (c) The resulting ensemble line shape computed from the convolution. The thick black line represents the FWHM of the distribution function.

equivalent, form of Equation 4.4:

$$\begin{aligned}\frac{d\tilde{\rho}_f}{dt} =& -\Gamma_f\tilde{\rho}_f + \frac{i}{2}\lambda_f\mu_f c_x(t-\tau_x) \\ & \times e^{i\kappa_f\left(\vec{k}\cdot z+\omega_x\tau_x\right)}e^{-i\kappa_f(\omega_x-|\omega_f|)t}\tilde{\rho}_i(t).\end{aligned} \tag{4.16}$$

We consider two oscillators with transition frequencies ω_f and $\omega'_f = \omega_f + \delta$. So long as $|\delta| \leq \omega_f$ (so that $|\omega_f + \delta| = |\omega_f| + \delta$ and thus the rotating wave approximation does not change), Equation 4.16 shows that the two are related by

$$\frac{d\tilde{\rho}'_f}{dt}(t;\omega_x) = \frac{d\tilde{\rho}_f}{dt}(t;\omega_x-\delta)e^{i\kappa_f\delta\tau_x}. \tag{4.17}$$

Because both coherences are assumed to have the same initial conditions ($\rho_0(-\infty) = \rho'_0(-\infty) = 0$), the equality also holds when both sides of the equation are integrated. The phase factor $e^{i\kappa_f\delta\tau_x}$ in the substitution arises from Equation 4.1, where the pulse carrier frequency maintains its phase within the pulse envelope for all delays.

The resonance translation can be extended to higher order signals as well. For a third-order signal, we compare systems with transition frequencies $\omega'_{10} = \omega_{10} + a$ and $\omega'_{21} = \omega_{21} + b$. The extension of Equation 4.17 to pathway $V\beta$ gives

$$\begin{aligned}\tilde{\rho}'_3(t;\omega_2,\omega'_2,\omega_1) =& \tilde{\rho}_3(t;\omega_2-a,\omega_{2'}-a,\omega_1-b) \\ & \times e^{i\kappa_2 a\tau_2}e^{i\kappa_{2'}a\tau_{2'}}e^{i\kappa_1 b\tau_1}.\end{aligned} \tag{4.18}$$

The translation of each laser coordinate depends on which transition is made (e.g. a for transitions between $|0\rangle$ and $|1\rangle$ or b for transitions between $|1\rangle$ and $|2\rangle$), so the exact translation relation differs between pathways. We can now compute the ensemble average of signal for pathway $V\beta$ as a convolution

between the distribution function of the system, $K(a,b)$, and the single oscillator response:

$$\begin{aligned}\langle\tilde{\rho}_3(t;\omega_2,\omega_{2'},\omega_1)\rangle = &\iint K(a,b)\\ &\times \tilde{\rho}_3(t;\omega_2+a,\omega_{2'}+a,\omega_1+b)\\ &\times e^{i\kappa_2 a\tau_2}e^{i\kappa_{2'}a\tau_{2'}}e^{i\kappa_1 b\tau_1}da\ db.\end{aligned} \tag{4.19}$$

For this work, we restrict ourselves to a simpler ensemble where all oscillators have equally spaced levels (i.e. $a=b$). This makes the translation identical for all pathways and reduces the dimensionality of the convolution. Since pathways follow the same convolution we may also perform the convolution on the total signal field:

$$\begin{aligned}\langle E_{\text{tot}}(t)\rangle = &\sum_L \mu_{4,L}\int K(a,a)\\ &\times \tilde{\rho}_{3,L}(t;\omega_x-a,\omega_y-a\omega_z-a)\\ &\times e^{ia(\kappa_x\tau_x+\kappa_y\tau_y+\kappa_z\tau_z)}da.\end{aligned} \tag{4.20}$$

Furthermore, since $\kappa=-1$ for E_1 and $E_{2'}$, while $\kappa=1$ for E_2, we have $e^{ia(\kappa_x\tau_x+\kappa_y\tau_y+\kappa_z\tau_z)} = e^{-ia(\tau_1-\tau_2+\tau_{2'})}$ for all pathways. Equivalently, if the electric field is parameterized in terms of laser coordinates ω_1 and ω_2, the ensemble field can be calculated as

$$\begin{aligned}\langle E_{\text{tot}}(t;\omega_1,\omega_2)\rangle = &\int K(a,a)E_{\text{tot}}(t;\omega_1-a,\omega_2-a)\\ &\times e^{-ia(\tau_1-\tau_2+\tau_{2'})}da.\end{aligned} \tag{4.21}$$

which is a 1D convolution along the diagonal axis in frequency space. Fig. 4.3 demonstrates the use of Equation 4.21 on a homogeneous line shape.

4.4 Results

We now present portions of our simulated data that highlight the dependence of the spectral line shapes and transients on excitation pulse width, the dephasing rate, detuning from resonance, the pulse delay times, and inhomogeneous broadening.

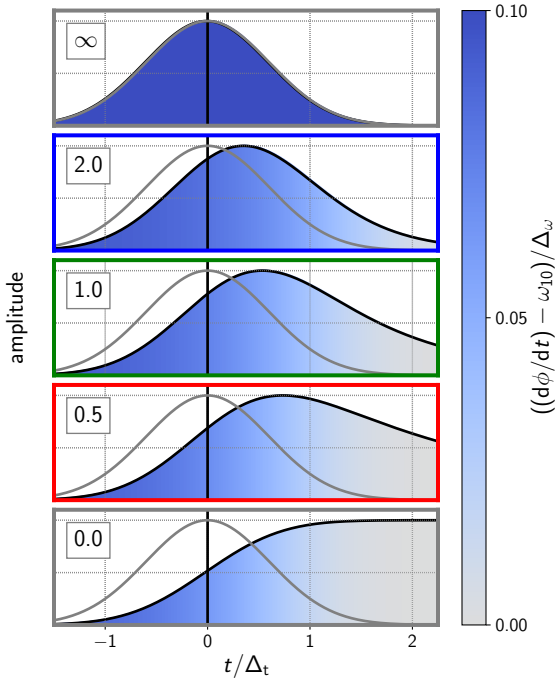

Figure 4.4: The relative importance of FID and driven response for a single quantum coherence as a function of the relative dephasing rate (values of $\Gamma_{10}\Delta_t$ are shown inset). The black line shows the coherence amplitude profile, while the shaded color indicates the instantaneous frequency (see colorbar). For all cases, the pulsed excitation field (gray line, shown as electric field amplitude) is slightly detuned (relative detuning, $\Omega_{fx}/\Delta_\omega = 0.1$).

4.4.1 Evolution of single coherence

It is illustrative to first consider the evolution of single coherences, $\rho_0 \xrightarrow{x} \rho_1$, under various excitation conditions. Fig. 4.4 shows the temporal evolution of ρ_1 with various dephasing rates under Gaussian excitation. The value of ρ_1 differs only by phase factors between various Liouville pathways (this can be verified by inspection of Equation 4.5 under the various conditions in Table S1), so the profiles in Fig. 4.4 apply for the first interaction of any pathway. The pulse frequency was detuned from resonance so that frequency changes could be visualized by the color bar, but the detuning was kept slight so that it did not appreciably change the dimensionless product, $\Delta_t\left(\Gamma_f + i\kappa_f\Omega_{fx}\right) \approx \Gamma_{10}\Delta_t$. In this case, the evolution demonstrates the maximum impulsive character the transient can achieve. The instantaneous frequency, $d\varphi/dt$, is defined as

$$\frac{d\varphi}{dt} = \frac{d}{dt}\tan^{-1}\left(\frac{\mathrm{Im}\left(\rho_1(t)\right)}{\mathrm{Re}\left(\rho_1(t)\right)}\right). \tag{4.22}$$

The cases of $\Gamma_{10}\Delta_t = 0(\infty)$ agree with the impulsive (driven) expressions derived in Appendix 4.3.1. For $\Gamma_{10}\Delta_t = 0$, the signal rises as the integral of the pulse and has instantaneous frequency close to that of the pulse (Equation 4.13), but as the pulse vanishes, the signal adopts the natural system frequency and decay rate (Equation 4.12). For $\Gamma_{10}\Delta_t = \infty$, the signal follows the amplitude and frequency of the pulse for all times (the driven limit, Equation 4.11).

The other three cases show a smooth interpolation between limits. As $\Gamma_{10}\Delta_t$ increases from the impulsive limit, the coherence within the pulse region conforms less to a pulse integral profile and more to a pulse envelope profile. In accordance, the FID component after the pulse becomes less prominent, and the instantaneous frequency pins to the driving frequency more strongly through the course of evolution. The trends can be understood by considering the differential form of evolution (Equation 4.4), and the time-dependent balance of optical coupling and system relaxation. We note that our choices of $\Gamma_{10}\Delta_t = 2.0, 1.0$, and 0.5 give coherences that have mainly driven, roughly equal driven and FID parts, and mainly FID components, respectively. FID character is difficult to isolate when $\Gamma_{10}\Delta_t = 2.0$.

Fig. 4.5a shows the temporal evolution of ρ_1 at several values of $\Omega_{1x}/\Delta_\omega$ with $\Gamma_{10}\Delta_t = 1$.[3] As detuning increases, total amplitude decreases, FID character vanishes, and ρ_1 assumes a more driven character,

[3] See Supplementary Fig. S3 for a Fourier domain representation of Fig. 4.5a.

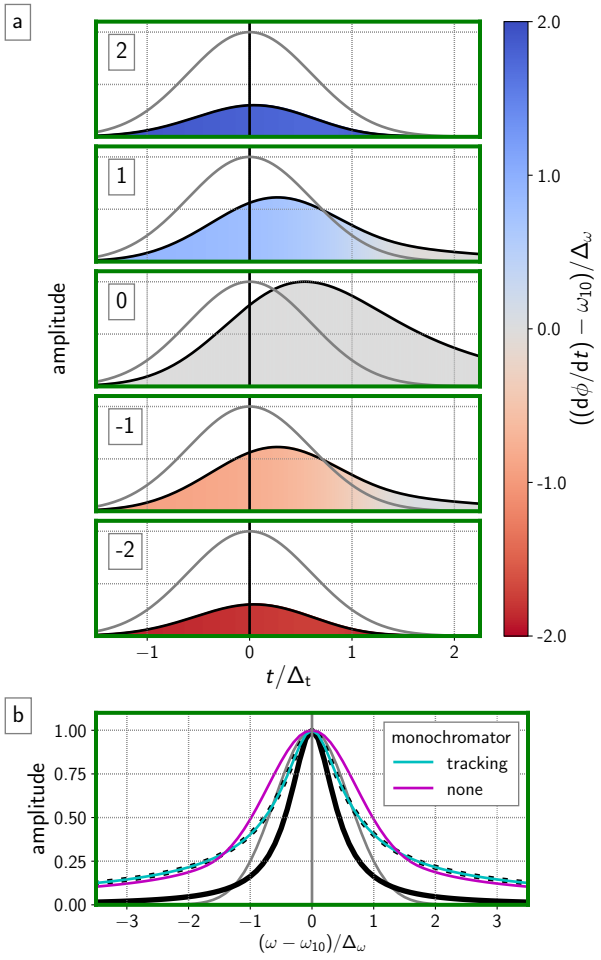

Figure 4.5: Pulsed excitation of a single quantum coherence and its dependence on the pulse detuning. In all cases, relative dephasing is kept at $\Gamma_{10}\Delta_t = 1$. (a) The relative importance of FID and driven response for a single quantum coherence as a function of the detuning (values of relative detuning, $\Omega_{fx}/\Delta_\omega$, are shown inset). The color indicates the instantaneous frequency (scale bar on right), while the black line shows the amplitude profile. The gray line is the electric field amplitude. (b) The time-integrated coherence amplitude as a function of the detuning. The integrated amplitude is collected both with (teal) and without (magenta) a tracking monochromator that isolates the driven frequency components. For comparison, the Green's function of the single quantum coherence is also shown (amplitude is black, hashed; imaginary is black, solid). In all plots, the gray line is the electric field amplitude.

as expected. During the excitation, ρ_1 maintains a phase relationship with the input field (as seen by the instantaneous frequency in Fig. 4.5a). The coherence will persist beyond the pulse duration only if the pulse transfers energy into the system; FID evolution equates to absorption. The FID is therefore sensitive to the absorptive (imaginary) line shape of a transition, while the driven response is the composite of both absorptive and dispersive components. If the experiment isolates the latent FID response, there is consequently a narrower spectral response. This spectral narrowing can be seen in Fig. 4.5a by comparing the coherence amplitudes at $t = 0$ (driven) and at $t/\Delta_t = 2$ (FID); amplitudes for all $\Omega_{fx}/\Delta_\omega$ values shown are comparable at $t = 0$, but the lack of FID formation for $\Omega_{fx}/\Delta_\omega = \pm 2$ manifests as a visibly disproportionate amplitude decay.[4] Many ultrafast spectroscopies take advantage of the latent FID to suppress non-resonant background, improving signal to noise.[**Lagutchev2007**, **Lagutchev2010**, **Donaldson2010**, **Donaldson2008**]

In driven experiments, the output frequency and line shape are fully constrained by the excitation beams. In such experiments, there is no additional information to be resolved in the output spectrum. The situation changes in the mixed domain, where E_{tot} contains FID signal that lasts longer than the pulse duration. Fig. 4.5a provides insight on how frequency-resolved detection of coherent output can enhance resolution when pulses are spectrally broad. Without frequency-resolved detection, mixed-domain resonance enhancement occurs in two ways: (1) the peak amplitude increases, and (2) the coherence duration increases due to the FID transient. Frequency-resolved detection can further discriminate against detuning by requiring that the driving frequency agrees with latent FID. The implications of discrimination are most easily seen in Fig. 4.5a with $\Omega_{1x}/\Delta_\omega = \pm 1$, where the system frequency moves from the driving frequency to the FID frequency. When the excitation pulse frequency is scanned, the resonance will be more sensitive to detuning by isolating the driven frequency (tracking the monochromator with the excitation source).

The functional form of the measured line shape can be deduced by considering the frequency domain form of Equation 4.5 (assume $\rho_i = 1$ and $\tau_x = 0$):

$$\tilde{\rho}_f(\omega) = \frac{i\lambda_f \mu_f}{2\sqrt{2\pi}} \cdot \frac{\mathcal{F}\{c_x\}(\omega - \kappa_f \Omega_{fx})}{\Gamma_f + i\omega}, \tag{4.23}$$

[4] See Supplementary Fig. S4 for explicit plots of $\rho_1(\Omega_{fx}/\Delta_\omega)$ at discrete t/Δ_t values.

where $\mathcal{F}\{c_x\}(\omega)$ denotes the Fourier transform of c_x, which in our case gives

$$\mathcal{F}\{c_x\}(\omega) = \frac{1}{\sqrt{2\pi}} e^{-\frac{(\Delta_t \omega)^2}{4 \ln 2}}. \tag{4.24}$$

For squared-law detection of ρ_f, the importance of the tracking monochromator is highlighted by two limits of Equation 4.23:

- When the transient is not frequency resolved, sig $\approx \int |\tilde{\rho}_f(\omega)|^2 \, d\omega$ and the measured line shape will be the convolution of the pulse envelope and the intrinsic (Green's function) response (Fig. 4.5b, magenta).
- When the driven frequency is isolated, sig $\approx |\tilde{\rho}_f(\kappa_f \Omega_{fx})|^2$ and the measured line shape will give the un-broadened Green's function (Fig. 4.5b, teal).

Monochromatic detection can remove broadening effects due to the pulse bandwidth. For large $\Gamma_{10}\Delta_t$ values, FID evolution is negligible at all $\Omega_{fx}/\Delta_\omega$ values and the monochromator is not useful. Fig. 4.5b shows the various detection methods for the relative dephasing rate of $\Gamma_{10}\Delta_t = 1$.

4.4.2 Evolution of single Liouville pathway

We now consider the multidimensional response of a single Liouville pathway involving three pulse interactions. In a multi-pulse experiment, ρ_1 acts as a source term for ρ_2 (and subsequent excitations). The spectral and temporal features of ρ_1 that are transferred to ρ_2 depend on when the subsequent pulse arrives. Time-gating later in ρ_1 evolution will produce responses with FID behavior, while time-gating ρ_1 in the presence of the initial pulse will produce driven responses. An analogous relationship holds for ρ_3 with its source term ρ_2. As discussed above, signal that time-gates FID evolution gives narrower spectra than driven-gated signal. As a result, the spectra of even single Liouville pathways will change based on pulse delays.

The final coherence will also be frequency-gated by the monochromator. The monochromator isolates signal at the fully driven frequency $\omega_{\text{out}} = \omega_1$. The monochromator will induce line-narrowing to the extent that FID takes place. It effectively enforces a frequency constraint that acts as an additional

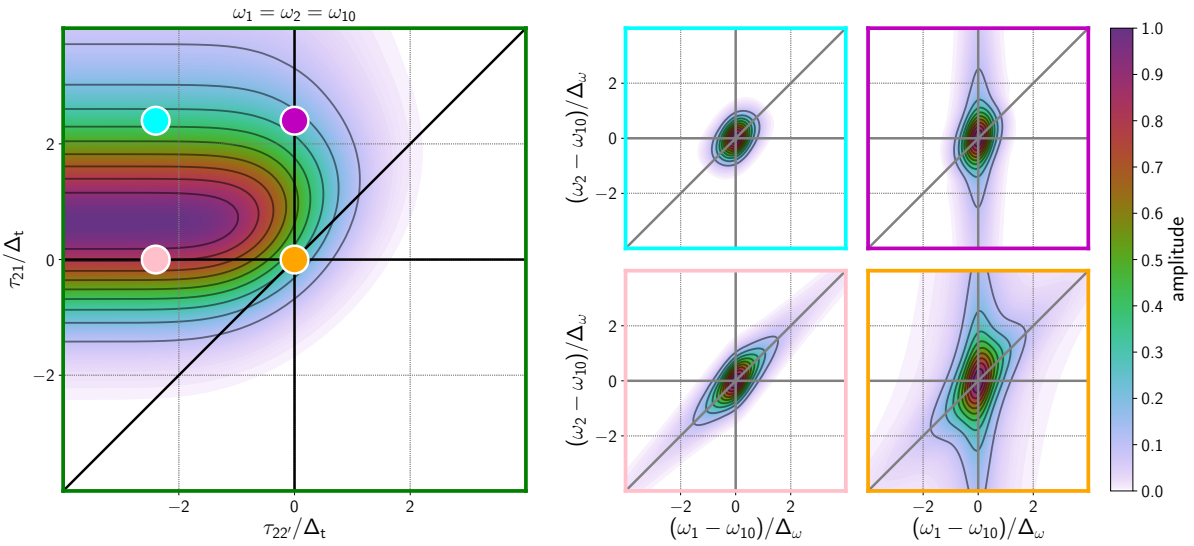

Figure 4.6: Changes to the 2D frequency response of a single Liouville pathway (Iγ) at different delay values. The normalized dephasing rate is $\Gamma_{10}\Delta_t = 1$. Left: The 2D delay response of pathway Iγ at triple resonance. Right: The 2D frequency response of pathway Iγ at different delay values. The delays at which the 2D frequency plots are collected are indicated on the delay plot; compare 2D spectrum frame color with dot color on 2D delay plot.

Table 4.1: Conditions for peak intensity at different pulse delays for pathway Iγ.

Delay		Approximate Resonance Conditions			
τ_{21}/Δ_t	$\tau_{22'}/\Delta_t$	$\rho_0 \xrightarrow{1} \rho_1$	$\rho_1 \xrightarrow{2} \rho_2$	$\rho_2 \xrightarrow{2'} \rho_3$	$\rho_3 \rightarrow$ detection at $\omega_m = \omega_1$
0	0	$\omega_1 = \omega_{10}$	$\omega_1 = \omega_2$	$\omega_1 = \omega_{10}$	–
0	-2.4	$\omega_1 = \omega_{10}$	$\omega_1 = \omega_2$	$\omega_2 = \omega_{10}$	$\omega_1 = \omega_2$
2.4	0	$\omega_1 = \omega_{10}$	$\omega_2 = \omega_{10}$	–	$\omega_1 = \omega_{10}$
2.4	-2.4	$\omega_1 = \omega_{10}$	$\omega_2 = \omega_{10}$	$\omega_2 = \omega_{10}$	$\omega_1 = \omega_2$

resonance condition, $\omega_{\text{out}} = \omega_1$. The driven frequency will be ω_1 if E_1 is the last pulse interaction (time-orderings V and VI), and the monochromator tracks the coherence frequency effectively. If E_1 is not the last interaction, the output frequency may not be equal to the driven frequency, and the monochromator plays a more complex role.

We demonstrate this delay dependence using the multidimensional response of the Iγ Liouville pathway as an example (see Fig. 4.1). Fig. 4.6 shows the resulting 2D delay profile of pathway Iγ signals for $\Gamma_{10}\Delta_t = 1$ (left) and the corresponding ω_1, ω_2 2D spectra at several pulse delay values (right). The spectral changes result from changes in the relative importance of driven and FID components. The prominence of FID signal can change the resonance conditions; Table 4.1 summarizes the changing resonance conditions for each of the four delay coordinates studied. Since E_1 is not the last pulse in pathway Iγ, the tracking monochromator must also be considered.[5]

When the pulses are all overlapped ($\tau_{21} = \tau_{22'} = 0$, lower right, orange), all transitions in the Liouville pathway are simultaneously driven by the incident fields. This spectrum strongly resembles the driven limit spectrum. For this time-ordering, the first, second, and third density matrix elements have driven resonance conditions of $\omega_1 = \omega_{10}$, $\omega_1 - \omega_2 = 0$, and $\omega_1 - \omega_2 + \omega_{2'} = \omega_{10}$, respectively. The second resonance condition causes elongation along the diagonal, and since $\omega_2 = \omega_{2'}$, the first and third resonance conditions are identical, effectively making ω_1 doubly resonant at ω_{10} and resulting in the vertical elongation along $\omega_1 = \omega_{10}$.

The other three spectra of Fig. 4.6 separate the pulse sequence over time so that not all interactions

[5] See Supplementary Fig. S5 for a representation of Fig. 5 simulated without monochromator frequency filtering ($M(\omega - \omega_1) = 1$ for Equation 4.10).

are driven. At $\tau_{21} = 0$, $\tau_{22'} = -2.4\Delta_t$ (lower left, pink), the first two resonances remain the same as at pulse overlap (orange) but the last resonance is different. The final pulse, $E_{2'}$, is latent and probes ρ_2 during its FID evolution after memory of the driven frequency is lost. There are two important consequences. Firstly, the third driven resonance condition is now approximated by $\omega_{2'} = \omega_{10}$, which makes ω_1 only singly resonant at $\omega_1 = \omega_{10}$. Secondly, the driven portion of the signal frequency is determined only by the latent pulse: $\omega_{\text{out}} = \omega_{2'}$. Since our monochromator gates ω_1, we have the detection-induced correlation $\omega_1 = \omega_{2'}$. The net result is double resonance along $\omega_1 = \omega_2$, and the vertical elongation of pulse overlap is strongly attenuated.

At $\tau_{21} = 2.4\Delta_t, \tau_{22'} = 0$ (upper right, purple), the first pulse E_1 precedes the latter two, which makes the two resonance conditions for the input fields $\omega_1 = \omega_{10}$ and $\omega_2 = \omega_{10}$. The signal depends on the FID conversion of ρ_1, which gives vertical elongation at $\omega_1 = \omega_{10}$. Furthermore, ρ_1 has no memory of ω_1 when E_2 interacts, which has two important implications. First, this means the second resonance condition $\omega_1 = \omega_2$ and the associated diagonal elongation is now absent. Second, the final output polarization frequency content is no longer functional of ω_1. Coupled with the fact that E_2 and $E_{2'}$ are coincident, so that the final coherence can be approximated as driven by these two, we can approximate the final frequency as $\omega_{\text{out}} = \omega_{10} - \omega_2 + \omega_{2'} = \omega_{10}$. Surprisingly, the frequency content of the output is strongly independent of all pulse frequencies. The monochromator narrows the $\omega_1 = \omega_{10}$ resonance. The $\omega_1 = \omega_{10}$ resonance condition now depends on the monochromator slit width, the FID propagation of ρ_1, the spectral bandwidth of ρ_3; its spectral width is not easily related to material parameters. This resonance demonstrates the importance of the detection scheme for experiments and how the optimal detection can change depending on the pulse delay time.

Finally, when all pulses are well-separated ($\tau_{21} = -\tau_{22'} = 2.4\Delta_t$, upper left, cyan), each resonance condition is independent and both E_1 and E_2 require FID buildup to produce final output. The resulting line shape is narrow in all directions. Again, the emitted frequency does not depend on ω_1, yet the monochromator resolves the final coherence at frequency ω_1. Since the driven part of the final interaction comes from $E_{2'}$, and since the monochromator track ω_1, the output signal will increase when $\omega_1 = \omega_{2'}$. As a result, the line shape acquires a diagonal character.

The changes in line shape seen in Fig. 4.6 have significant ramifications for the interpretations and

strategies of MR-CMDS in the mixed domain. Time-gating has been used to isolate the 2D spectra of a certain time-ordering[**Meyer2004**, **Pakoulev2006**, **Donaldson2007**], but here we show that time-gating itself causes significant line shape changes to the isolated pathways. The phenomenon of time-gating can cause frequency and delay axes to become functional of each other in unexpected ways.

4.4.3 Temporal pathway discrimination

In the last section we showed how a single pathway's spectra can evolve with delay due to pulse effects and time gating. In real experiments, evolution with delay is further complicated by the six time-orderings/sixteen pathways present in our three-beam experiment (see Fig. 4.1). Each time-ordering has different resonance conditions. When signal is collected near pulse overlap, multiple time-orderings contribute. To identify these effects, we start by considering how strongly time-orderings are isolated at each delay coordinate.

While the general idea of using time delays to enhance certain time-ordered regions is widely applied, quantitation of this discrimination is rarely explored. Because the temporal profile of the signal is dependent on both the excitation pulse profile and the decay dynamics of the coherence itself, quantitation of pathway discrimination requires simulation.

Fig. 4.7 shows the 2D delay space with all pathways present for $\omega_1, \omega_2 = \omega_{10}$. It illustrates the interplay of pulse width and system decay rates on the isolation of time-ordered pathways. The color bar shows the signal amplitude. Signal is symmetric about the $\tau_{21} = \tau_{22'}$ line because when $\omega_1 = \omega_2$, E_1 and $E_{2'}$ interactions are interchangeable: $S_{\text{tot}}(\tau_{21}, \tau_{22'}) = S_{\text{tot}}(\tau_{22'}, \tau_{21})$. The overlaid black contours represent signal "purity," P, defined as the relative amount of signal that comes from the dominant pathway at that delay value:

$$P(\tau_{21}, \tau_{22'}) = \frac{\max\{S_L(\tau_{21}, \tau_{22'})\}}{\sum_L S_L(\tau_{21}, \tau_{22'})}. \tag{4.25}$$

The dominant pathway ($\max\{S_L(\tau_{21}, \tau_{22'})\}$) at given delays can be inferred by the time-ordered region defined in Fig. 4.2d. The contours of purity generally run parallel to the time-ordering boundaries with the exception of time-ordered regions II and IV, which involve the double quantum coherences that have been neglected.

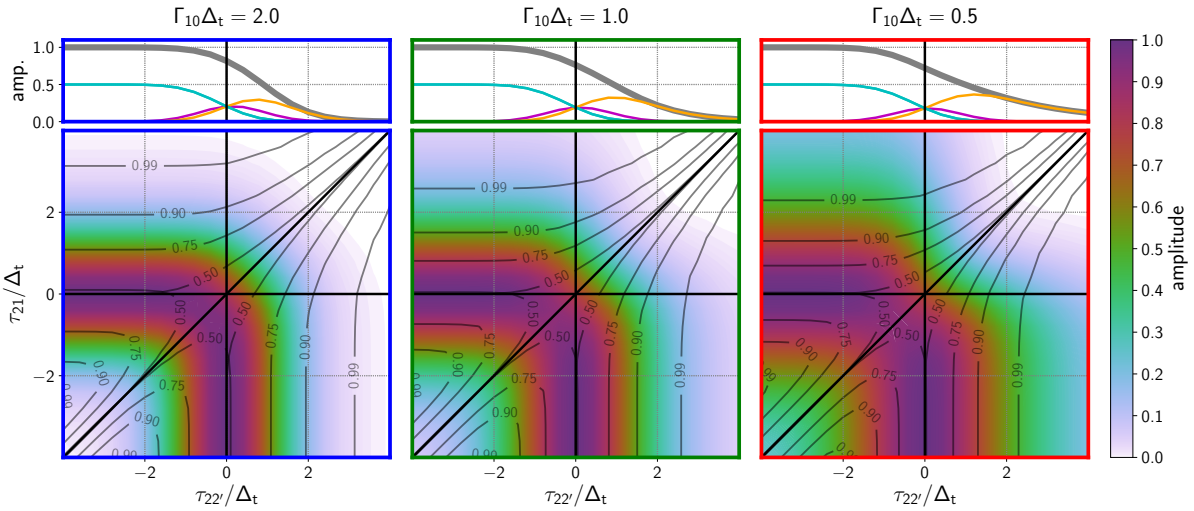

Figure 4.7: Comparison of the 2D delay response for different relative dephasing rates (labeled atop each column). All pulses are tuned to exact resonance. In each 2D delay plot, the signal amplitude is depicted by the colors. The black contour lines show signal purity, P (see Equation 4.25), with purity values denoted on each contour. The small plots above each 2D delay plot examine a $\tau_{22'}$ slice of the delay response ($\tau_{21} = 0$). The plot shows the total signal (black), as well as the component time-orderings VI (orange), V (purple), and III or I (teal).

A commonly-employed metric for temporal selectivity is how definitively the pulses are ordered. This metric agrees with our simulations. The purity contours have a weak dependence on $\Delta_t\Gamma_{10}$ for $|\tau_{22'}|/\Delta_t < 1$ or $|\tau_{21}|/\Delta_t < 1$ where there is significant pathway overlap and a stronger dependence at larger values where the pathways are well-isolated. Because responses decay exponentially, while pulses decay as Gaussians, there always exist delays where temporal discrimination is possible. As $\Delta_t\Gamma_{10} \to \infty$, however, such discrimination is only achieved at vanishing signal intensities; the contour of $P = 0.99$ across our systems highlights this trend.

4.4.4 Multidimensional line shape dependence on pulse delay time

In the previous sections we showed how pathway spectra and weights evolve with delay. This section ties the two concepts together by exploring the evolution of the spectral line shape over a span of τ_{21} delay times that include all pathways. It is a common practice to explore spectral evolution against τ_{21} because this delay axis shows population evolution in a manner analogous to pump-probe spectroscopies. The $\vec{k}_2$ and $\vec{k}_{2'}$ interactions correspond to the pump, and the $\vec{k}_1$ interaction corresponds to the probe. Time-orderings V and VI are the normal pump-probe time-orderings, time-ordering III is a mixed pump-probe-pump ordering (so-called pump polarization coupling), and time-ordering I is the probe-pump ordering (so-called perturbed FID). Scanning τ_{21} through pulse overlap complicates interpretation of the line shape due to the changing nature and balance of the contributing time-orderings. At $\tau_{21} > 0$, time-ordering I dominates; at $\tau_{21} = 0$, all time-orderings contribute equally; at $\tau_{21} < 0$ time-orderings V and VI dominate (Fig. 4.7). Conventional pump-probe techniques recognized these complications long ago,[**BritoCruz1988**, **Palfrey1985**] but the extension of these effects to MR-CMDS has not previously been done.

Fig. 4.8 shows the MR-CMDS spectra, as well as histograms of the pathway weights, while scanning τ_{21} through pulse overlap. The colored histogram bars and line shape contours correspond to different values of the relative dephasing rate, $\Gamma_{10}\Delta_t$. The contour is the half-maximum of the line shape.[6] The dependence of the line shape amplitude on τ_{21} can be inferred from Fig. 4.7.

[6] Supplementary Fig. S6 shows fully colored contour plots of each 2D frequency spectrum.

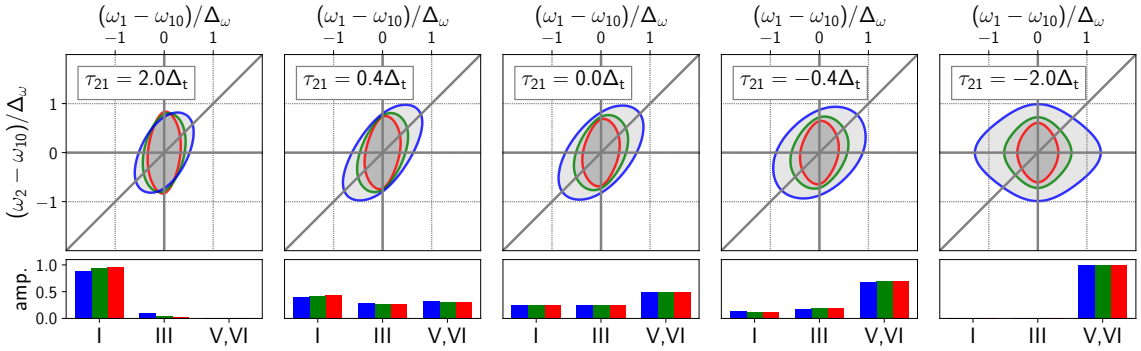

Figure 4.8: Evolution of the 2D frequency response as a function of τ_{21} (labeled inset) and the influence of the relative dephasing rate ($\Gamma_{10}\Delta_t = 0.5$ (red), 1.0 (green), and 2.0 (blue)). In all plots $\tau_{22'} = 0$. To ease comparison between different dephasing rates, the colored line contours (showing the half-maximum) for all three relative dephasing rates are overlaid. The colored histograms below each 2D frequency plot show the relative weights of each time-ordering for each relative dephasing rate. Contributions from V and VI are grouped together because they have equal weights at $\tau_{22'} = 0$.

The qualitative trend, as τ_{21} goes from positive to negative delays, is a change from diagonal/compressed line shapes to much broader resonances with no correlation (ω_1 and ω_2 interact with independent resonances). Such spectral changes could be misinterpreted as spectral diffusion, where the line shape changes from correlated to uncorrelated as population time increases due to system dynamics. The system dynamics included here, however, contain no structure that would allow for such diffusion. Rather, the spectral changes reflect the changes in the majority pathway contribution, starting with time-ordering I pathways, proceeding to an equal admixture of I, III, V, and VI, and finishing at an equal balance of V and VI when E_1 arrives well after E_2 and $E_{2'}$. Time-orderings I and III both exhibit a spectral correlation in ω_1 and ω_2 when driven, but time-orderings V and VI do not. Moreover, such spectral correlation is forced near zero delay because the pulses time-gate the driven signals of the first two induced polarizations. The monochromator detection also plays a dynamic role, because time-orderings V always VI always emit a signal at the monochromator frequency, while in time-orderings I and III the emitted frequency is not defined by ω_1, as discussed above.

When we isolate time-orderings V and VI, we can maintain the proper scaling of FID bandwidth in the ω_1 direction because our monochromator can gate the final coherence. This gating is not possible in time-orderings I and III because the final coherence frequency is determined by $\omega_{2'}$ which is identical to ω_2.

There are differences in the line shapes for the different values of the relative dephasing rate, $\Gamma_{10}\Delta_t$. The spectral correlation at $\tau_{21}/\Delta_t = 2$ decreases in strength as $\Gamma_{10}\Delta_t$ decreases. As we illustrated in Fig. 4.6, this spectral correlation is a signature of driven signal from temporal overlap of E_1 and E_2; the loss of spectral correlation reflects the increased prominence of FID in the first coherence as the field-matter interactions become more impulsive. This increased prominence of FID also reflects an increase in signal strength, as shown by τ_{21} traces in Fig. 4.7. When all pulses are completely overlapped, ($\tau_{21} = 0$), each of the line shapes exhibit spectral correlation. At $\tau_{21}/\Delta_t = -2$, the line shape shrinks as $\Gamma_{10}\Delta_t$ decreases, with the elongation direction changing from horizontal to vertical. The general shrinking reflects the narrowing homogeneous linewidth of the ω_{10} resonance. In all cases, the horizontal line shape corresponds to the homogeneous linewidth because the narrow bandpass monochromator resolves the final ω_1 resonance. The change in elongation direction is due to the resolving power of ω_2. At

$\Gamma_{10}\Delta_t = 0.5$, the resonance is broader than our pulse bandwidth and is fully resolved vertically. It is narrower than the ω_1 resonance because time-orderings V and VI interfere to isolate only the absorptive line shape along ω_2. This narrowing, however, is unresolvable when the pulse bandwidth becomes broader than that of the resonance, which gives rise to a vertically elongated signal when $\Gamma_{10}\Delta_t = 0.5$.

It is also common to represent data as "Wigner plots," where one axis is delay and the other is frequency.[**Kohler2014**, **Aubock2012**, **Czech2015**, **Pakoulev2007**] In Fig. 4.9 we show five τ_{21}, ω_1 plots for varying ω_2 with $\tau_{22'} = 0$.[7] The plots are the analogue to the most common multidimensional experiment of Transient Absorption spectroscopy, where the non-linear probe spectrum is plotted as a function of the pump-probe delay. For each plot, the ω_2 frequency is denoted by a vertical gray line. Each Wigner plot is scaled to its own dynamic range to emphasize the dependence on ω_2. The dramatic line shape changes between positive and negative delays can be seen. This representation also highlights the asymmetric broadening of the ω_1 line shape near pulse overlap when ω_2 becomes non-resonant. Again, these features can resemble spectral diffusion even though our system is homogeneous.

4.4.5 Inhomogeneous broadening

With the homogeneous system characterized, we can now consider the effect of inhomogeneity. For inhomogeneous systems, time-orderings III and V are enhanced because their final coherence will rephase to form a photon echo, whereas time-orderings I and VI will not. In delay space, this rephasing appears as a shift of signal to time-ordered regions III and V that persists for all population times. Fig. 4.10 shows the calculated spectra for relative dephasing rate $\Gamma_{10}\Delta_t = 1$ with a frequency broadening function of width $\Delta_{\text{inhom}} = 0.441\Gamma_{10}$. The inhomogeneity makes it easier to temporally isolate the rephasing pathways and harder to isolate the non-rephasing pathways, as shown by the purity contours.

A common metric of rephasing in delay space is the 3PEPS measurement.[**Weiner1985**, **Fleming1998**, **Boeij1998**, **Salvador2003**] In 3PEPS, one measures the signal as the first coherence time, τ, is scanned across both rephasing and non-rephasing pathways while keeping population time, T, constant. The position of the peak is measured; a peak shifted away from $\tau = 0$ reflects the rephasing ability of the

[7] See Supplementary Fig. S8 for Wigner plots for all $\Gamma_{10}\Delta_t$ values.

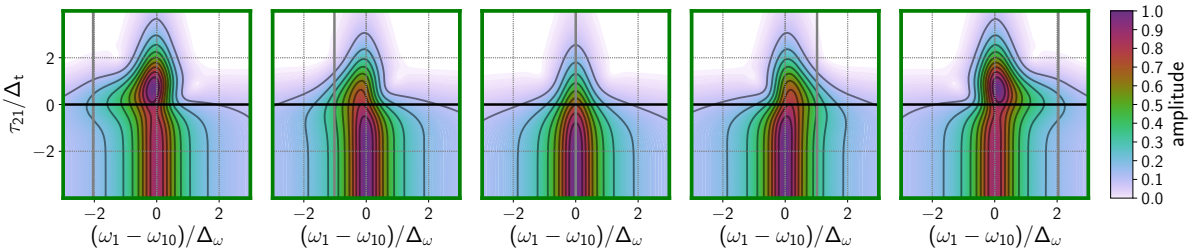

Figure 4.9: Transient (ω_1) line shapes and their dependence on ω_2 frequency. The relative dephasing rate is $\Gamma_{10}\Delta_t = 1$ and $\tau_{22'} = 0$. For each plot, the corresponding ω_2 value is shown as a light gray vertical line.

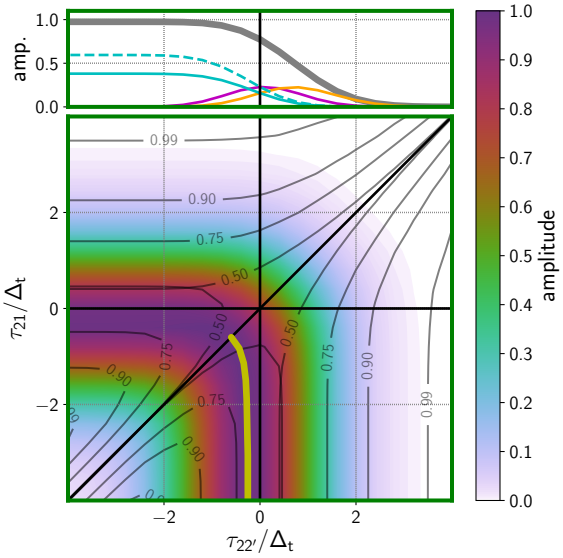

Figure 4.10: 2D delay response for $\Gamma_{10}\Delta_t = 1$ with sample inhomogeneity. All pulses are tuned to exact resonance. The colors depict the signal amplitude. The black contour lines show signal purity, P (see Equation 4.25), with purity values denoted on each contour. The thick yellow line denotes the peak amplitude position that is used for 3PEPS analysis. The small plot above each 2D delay plot examines a $\tau_{22'}$ slice of the delay response ($\tau_{21} = 0$). The plot shows the total signal (black), as well as the component time-orderings VI (orange), V (purple), III (teal, dashed), and I (teal, solid).

system. An inhomogeneous system will emit a photon echo in the rephasing pathway, enhancing signal in the rephasing time-ordering and creating the peak shift. In our 2D delay space, the τ trace can be defined if we assume E_2 and $E_{2'}$ create the population (time-orderings V and VI). The trace runs parallel to the III-V time-ordering boundary (diagonal) if $\tau_{22'} < 0$ and runs parallel to the IV-VI time-ordering boundary (horizontal) if $\tau_{22'} > 0$, and both intersect at $\tau_{22'} = 0$; the $-\tau_{21}$ value at this intersection is T.[8] In our 2D delay plots (Fig. 4.7, Fig. 4.10), the peak shift is seen as the diagonal displacement of the signal peak from the $\tau_{21} = 0$ vertical line.[9] Fig. 4.10 highlights the peak shift profile as a function of population time with the yellow trace; it is easily verified that our static inhomogneous system exhibits a non-zero peak shift value for all population times.

The unanticipated feature of the 3PEPS analysis is the dependence on T. Even though our inhomogeneity is static, the peak shift is maximal at $T = 0$ and dissipates as T increases, mimicking spectral diffusion. This dynamic arises from signal overlap with time-ordering III, which uses E_2 and E_1 as the first two interactions ,and merely reflects E_1 and E_2 temporal overlap. At $T = 0$, the τ trace gives two ways to make a rephasing pathway (time-orderings III and V) and only one way to make a non-rephasing pathway (time-ordering VI). This pathway asymmetry shifts signal away from $\tau = 0$ into the rephasing direction. At large T (large τ_{21}), time-ordering III is not viable and pathway asymmetry disappears. Peak shifts imply inhomogeneity only when time-orderings V and III are minimally contaminated by each other i.e. at population times that exceed pulse overlap. This fact is easily illustrated by the dynamics of homogeneous system (Fig. 4.7); even though the homogeneous system cannot rephase, there is a non-zero peak shift near $T = 0$. The contamination of the 3PEPS measurement at pulse overlap is well-known and is described in some studies,[**DeBoeij1996**, **Agarwal2002**] but the dependence of pulse and system properties on the distortion has not been investigated previously. Peak-shifting due to pulse overlap is less important when $\omega_1 \neq \omega_2$ because time-ordering III is decoupled by detuning.

In frequency space, spectral elongation along the diagonal is the signature of inhomogeneous broadening. Fig. 4.11 shows the line shape changes of a Gaussian inhomogeneous distribution.[10] All systems are

[8] See Supplementary Fig. S9 for an illustration of how 3PEPS shifts are measured from a 2D delay plot.

[9] Supplementary Fig. S10 shows the 3PEPS measurements of all 12 combinations of $\Gamma_{10}\Delta_t$ and Δ_{inhom}, for every population delay surveyed.

[10] As in Fig. 4.8, Fig. 4.11 shows only the contours at the half-maximum amplitude. See Supplementary Fig. S7 for all contours.

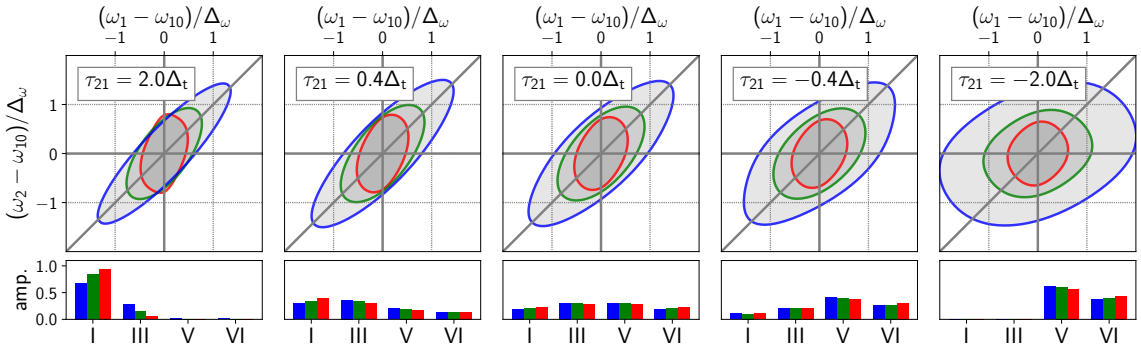

Figure 4.11: Same as Fig. 4.8, but each system has inhomogeneity ($\Delta_{\text{inhom}} = 0.441\Gamma_{10}$). Relative dephasing rates are $\Gamma_{10}\Delta_t = 0.5$ (red), 1.0 (green), and 2.0 (blue). In all plots $\tau_{22'} = 0$. To ease comparison between different dephasing rates, the colored line shapes of all three systems are overlaid. Each 2D plot shows a single representative contour (half-maximum) for each $\Gamma_{10}\Delta_t$ value. The colored histograms below each 2D frequency plot show the relative weights of each time-ordering for each 2D frequency plot. In contrast to Fig. 4.8, inhomogeneity makes the relative contributions of time-orderings V and VI unequal.

broadened by a distribution proportional to their dephasing bandwidth. As expected, the sequence again shows a gradual broadening along the ω_1 axis, with a strong spectral correlation at early delays ($\tau_{21} > 0$) for the more driven signals. The anti-diagonal width at early delays (e.g. Fig. 4.11, $\tau_{21} = 2.0\Delta_t$) again depends on the pulse bandwidth and the monochromator slit width. At delay values that isolate time-orderings V and VI, however, the line shapes retain diagonal character, showing the characteristic balance of homogeneous and inhomogeneous width.

4.5 Discussion

4.5.1 An intuitive picture of pulse effects

Our chosen values of the relative dephasing time, $\Gamma_{10}\Delta_t$, describe experiments where neither the impulsive nor driven limit unilaterally applies. We have illustrated that in this intermediate regime, the multidimensional spectra contain attributes of both limits, and that it is possible to judge when these attributes apply. In our three-pulse experiment the second and third pulses time-gate coherences and populations produced by the previous pulse(s), and the monochromator frequency-gates the final coherence. Time-gating isolates different properties of the coherences and populations. Consequently, spectra evolve against delay. For any delay coordinate, one can develop qualitative line shape expectations by considering the following three principles:

1. When time-gating during the pulse, the system pins to the driving frequency with a buildup efficiency determined by resonance.
2. When time-gating after the pulse, the FID dominates the system response.
3. The emitted signal field contains both FID and driven components; the $\omega_{\text{out}} = \omega_1$ component is isolated by the tracking monochromator.

Fig. 4.4 illustrates principles 1 and 2 and Fig. 4.5 illustrates principle 2 and 3. Fig. 4.6 provides a detailed example of the relationship between these principles and the multidimensional line shape changes for different delay times.

The principles presented above apply to a single pathway. For rapidly dephasing systems it is difficult to achieve complete pathway discrimination, as shown in Fig. 4.7. In such situations the interference between pathways must be considered to predict the line shape. The relative weight of each pathway to the interference can be approximated by the extent of pulse overlap. The pathway weights exchange when scanning across pulse overlap, which creates the dramatic line shape changes observed in Figs. 4.8 and 4.11.

4.5.2 Conditional validity of the driven limit

We have shown that the driven limit misses details of the line shape if $\Gamma_{10}\Delta_t \approx 1$, but we have also reasoned that in certain conditions the driven limit can approximate the response well (see principle 1). Here we examine the line shape at delay values that demonstrate this agreement. Fig. 4.12 compares the results of our numerical simulation (third column) with the driven limit expressions for populations where $\Gamma_{11}\Delta_t = 0$ (first column) or 1 (second column). The top and bottom rows compare the line shapes when $(\tau_{22'}, \tau_{21} = (0, 0))$ and $(0, -4\Delta_t)$, respectively. The third column demonstrates the agreement between the driven limit approximations with the simulation by comparing the diagonal and anti-diagonal cross-sections of the 2D spectra.

Note the very sharp diagonal feature that appears for $(\tau_{21}, \tau_{22'}) = (0, 0)$ and $\Gamma_{11} = 0$; this is due to population resonance in time-orderings I and III. This expression is inaccurate: the narrow resonance is only observed when pulse durations are much longer than the coherence time. A comparison of picosecond and femtosecond studies of quantum dot exciton line shapes (Yurs *et al.*[**Yurs2011**] and Kohler *et al.*[**Kohler2014**], respectively) demonstrates this difference well. The driven equation fails to reproduce our numerical simulations here because resonant excitation of the population is impulsive; the experiment time-gates only the rise time of the population, yet driven theory predicts the resonance to be vanishingly narrow ($\Gamma_{11} = 0$). In light of this, one can approximate this time-gating effect by substituting population lifetime with the pulse duration ($\Gamma_{11}\Delta_t = 1$), which gives good agreement with the numerical simulation (third column).

When $\tau_{22'} = 0$ and $\tau_{21} < \Delta_t$, signals can also be approximated by driven signal (Fig. 4.12 bottom row).

Only time-orderings V and VI are relevant. The intermediate population resonance is still impulsive but it depends on $\omega_{2'} - \omega_2$ which is not explored in our 2D frequency space.

4.5.3 Extracting true material correlation

We have shown that pulse effects mimic the qualitative signatures of inhomogeneity. Here we address how one can extract true system inhomogeneity in light of these effects. We focus on two ubiquitous metrics of inhomogeneity: 3PEPS for the time domain and ellipticity[11] for the frequency domain[**Kwac2003**, **Okumura1999**]. In the driven (impulsive) limit, ellipticity (3PEPS) corresponds to the frequency correlation function and uniquely extracts the inhomogeneity of the models presented here. In their respective limits, the metrics give values proportional to the inhomogeneity.

Fig. 4.13 shows the results of this characterization for all Δ_{inhom} and $\Gamma_{10}\Delta_t$ values explored in this work. We study how the correlations between the two metrics depend on the relative dephasing rate, $\Gamma_{10}\Delta_t$, the absolute inhomogeneity, $\Delta_{\text{inhom}}/\Delta_\omega$, the relative inhomogeneity $\Delta_{\text{inhom}}/\Gamma_{10}$, and the population time delay.[12] The top row shows the correlations of the $\Delta_{\text{3PEPS}}/\Delta_t$ 3PEPS metric that represents the normalized coherence delay time required to reach the peak intensity. The upper right graph shows the correlations for a population time delay of $T = 4\Delta_t$ that isolates the V and VI time-orderings. For this time delay, the $\Delta_{\text{3PEPS}}/\Delta_t$ metric works well for all dephasing times of $\Gamma_{10}\Delta_t$ when the relative inhomogeneity is $\Delta_{\text{inhom}}/\Delta_\omega \ll 1$. It becomes independent of $\Delta_{\text{inhom}}/\Delta_\omega$ when $\Delta_{\text{inhom}}/\Delta_\omega > 1$. This saturation results because the frequency bandwidth of the excitation pulses becomes smaller than the inhomogeneous width and only a portion of the inhomogeneous ensemble contributes to the 3PEPS experiment.[**Weiner1985**] The corresponding graph for $T = 0$ shows a large peak shift occurs, even without inhomogeneity. In this case, the peak shift depends on pathway overlap, as discussed in Section 4.4.5.

The middle row in Fig. 4.13 shows the ellipticity dependence on the relative dephasing rate and inhomogeneity assuming the measurement is performed when the first two pulses are temporally overlapped

[11] There are many ways to characterize the ellipticity of a peak shape. We adopt the convention $\mathcal{E} = \left(a^2 - b^2\right) / \left(a^2 + b^2\right)$, where a is the diagonal width and b is the antidiagonal width.

[12] The simulations for each value of the 3PEPS and ellipticity data in Fig. 4.13 appear in Supplementary Figs. S10-S12.

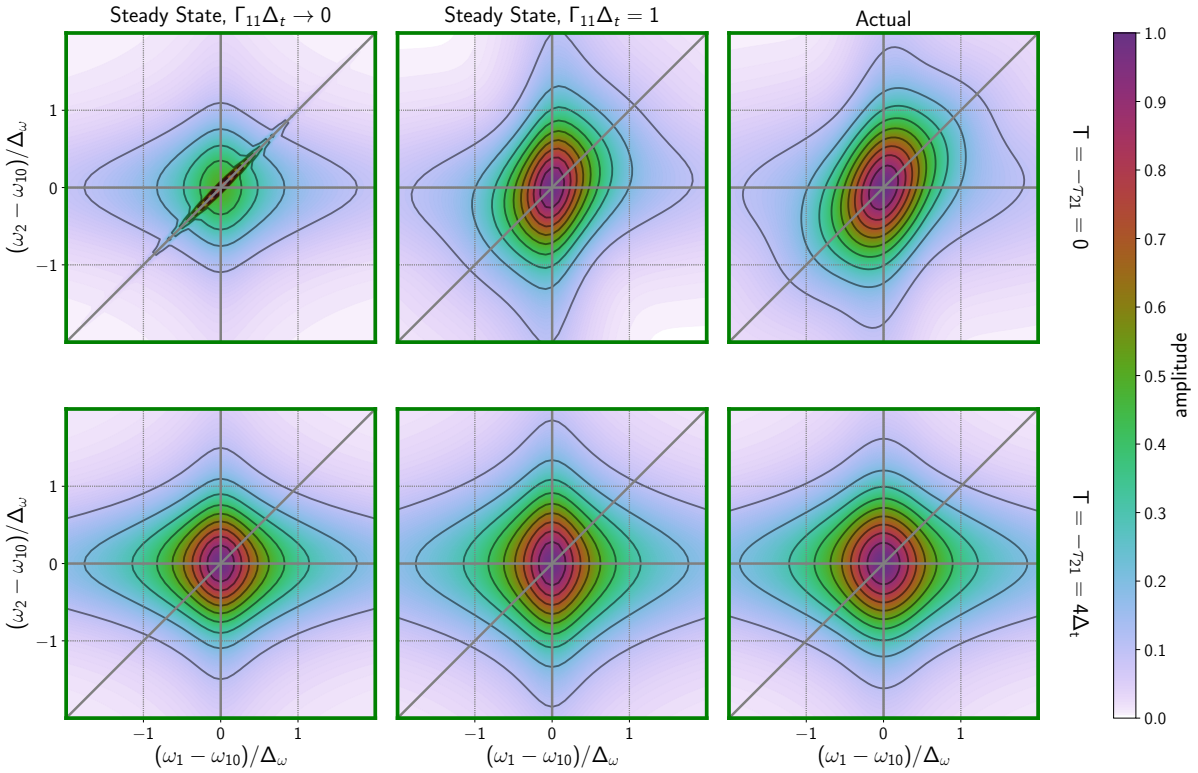

Figure 4.12: Comparing approximate expressions of the 2D frequency response with the directly integrated response. $\Gamma_{10}\Delta_t = 1$. The top row compares the 2D response of all time-orderings ($\tau_{21} = 0$) and the bottom row compares the response of time-orderings V and VI ($\tau_{21} = -4\Delta_t$). First column: The driven limit response. Note the narrow diagonal resonance for $\tau_{21} = 0$. Second column: Same as the first column, but with ad hoc substitution $\Gamma_{11} = \Delta_t$. Third column: The directly integrated response.

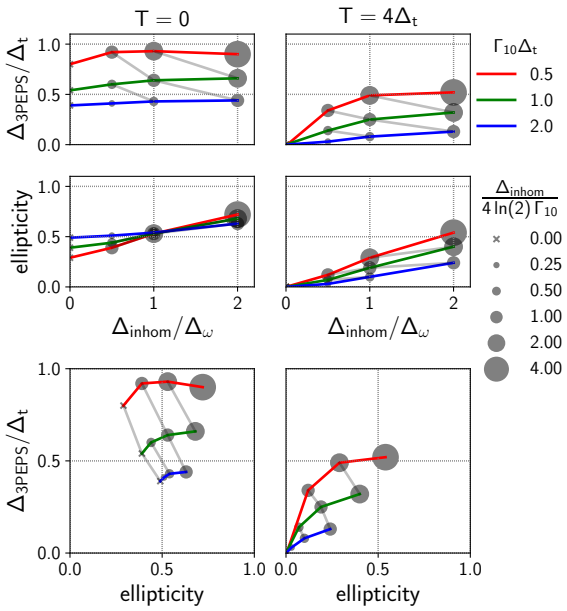

Figure 4.13: Temporal (3PEPS) and spectral (ellipticity) metrics of correlation and their relation to the true system inhomogeneity. The left column plots the relationship at pulse overlap ($T = 0$) and the right column plots the relationship at a delay where driven correlations are removed ($T = 4\Delta_t$). For the ellipticity measurements, $\tau_{22'} = 0$. In each case, the two metrics are plotted directly against system inhomogeneity (top and middle row) and against each other (bottom row). Colored lines guide the eyes for systems with equal relative dephasing rates ($\Gamma_{10}\Delta_t$, see upper legend), while the area of the data point marker indicates the relative inhomogeneity ($\Delta_{\text{inhom}}/\Gamma_{10}$, see lower legend). Gray lines indicate contours of constant relative inhomogeneity (scatter points with the same area are connected).

($\tau_{22'} = 0$). For a $T = 4\Delta_t$ population time, the ellipticity is proportional to the inhomogeneity until $\Delta_{\text{inhom}}/\Delta_\omega \ll 1$ where the excitation bandwidth is wide compared with the inhomogeneity. Unlike 3PEPS, saturation is not observed because pulse bandwidth does not limit the frequency range scanned. The 3PEPS and ellipticity metrics are therefore complementary since 3PEPS works well for $\Delta_{\text{inhom}}/\Delta_\omega \ll 1$ and ellipticity works well for $\Delta_{\text{inhom}}/\Delta_\omega \gg 1$. When all pulses are temporally overlapped at $T = 0$, the ellipticity is only weakly dependent on the inhomogeneity and dephasing rate. The ellipticity is instead dominated by the dependence on the excitation pulse frequency differences of time-orderings I and III that become important at pulse overlap.

It is clear from the previous discussion that both metrics depend on the dephasing and inhomogeneity. The dephasing can be measured independently in the frequency or time domain, depending upon whether the dephasing is very fast or slow, respectively. In the mixed frequency/time domain, measurement of the dephasing becomes more difficult. One strategy to address this challenge is to use both the 3PEPS and ellipticity metrics. The bottom row in Fig. 4.13 plots 3PEPS against ellipticity to show how the relationship between the metrics changes for different amounts of dephasing and inhomogeneity. The anti-diagonal contours of constant relative inhomogeneity show that these metrics are complementary and can serve to extract the system correlation parameters.

Importantly, the metrics are uniquely mapped both in the presence and absence of pulse-induced effects (demonstrated by $T = 0$ and $T = 4\Delta_t$, respectively). The combined metrics can be used to determine correlation at $T = 0$, but the correlation-inducing pulse effects give a mapping significantly different than at $T = 4\Delta_t$. At $T = 0$, 3PEPS is almost nonresponsive to inhomogeneity; instead, it is an almost independent characterization of the pure dephasing. In fact, the $T = 0$ trace is equivalent to the original photon echo traces used to resolve pure dephasing rates.[**Aartsma1976**] Both metrics are offset due to the pulse overlap effects. Accordingly, the region to the left of homogeneous contour is non-physical, because it represents observed correlations that are less than that given by pulse overlap effects. If the metrics are measured as a function of T, the mapping gradually changes from the left figure to the right figure in accordance with the pulse overlap. Both metrics will show a decrease, even with static inhomogeneity. If a system has spectral diffusion, the mapping at late times will disagree with the mapping at early times; both ellipticity and 3PEPS will be smaller at later times than predicted

by the change in mappings alone.

4.6 Conclusion

This study provides a framework to describe and disentangle the influence of the excitation pulses in mixed-domain ultrafast spectroscopy. We analyzed the features of mixed domain spectroscopy through detailed simulations of MR-CMDS signals. When pulse durations are similar to coherence times, resolution is compromised by time-bandwidth uncertainty and the complex mixture of driven and FID response. The dimensionless quantity $\Delta_t\,(\Gamma_f + i\kappa_f\Omega_{fx})$ captures the balance of driven and FID character in a single field-matter interaction. In the nonlinear experiment, with multiple field-matter interactions, this balance is also controlled by pulse delays and frequency-resolved detection. Our analysis shows how these effects can be intuitive.

The dynamic nature of pulse effects can lead to misleading changes to spectra when delays are changed. When delays separate pulses, the spectral line shapes of individual pathways qualitatively change because the delays isolate FID contributions and de-emphasize driven response. When delays are scanned across pulse overlap, the weights of individual pathways change, further changing the line shapes. In a real system, these changes would all be present in addition to actual dynamics and spectral changes of the material.

Finally, we find that, in either frequency or time domain, pulse effects mimic signatures of ultrafast inhomogeneity. Even homogeneous systems take on these signatures. For mixed domain experiments, pulse effects induce spectral ellipticity and photon echo signatures, even in homogeneous systems. Driven character gives rise to pathway overlap peak shifting in the 2D delay response, which artificially produces rephasing near pulse overlap. Driven character also produces resonances that depend on $\omega_1 - \omega_2$ near pulse overlap. Determination of the homogeneous and inhomogeneous broadening at ultrashort times is only possible by performing correlation analysis in both the frequency and time domain.

Part II

Instrumental Development

Chapter 5

Software

Cutting-edge science increasingly relies on custom software. In their 2008 survey, Hannay et al. [7] demonstrated just how important software is to the modern scientist.

- → 84.3% of surveyed scientists state that developing scientific software is important or very important for their own research.
- → 91.2% of surveyed scientists state that using scientific software is important or very important for their own research.
- → On average, scientists spend approximately 40% of their work time using scientific software.
- → On average, scientists spend approximately 30% of their work time developing scientific software.

Despite the importance of software to science and scientists, most scientists are not familiar with basic software engineering concepts. This is in part due to the their general lack of formal training in programming and software development. Hannay et al. [7] found that over 90% of scientists learn software development through 'informal self study'. Indeed, I myself have never been formally trained in software development.

Software development in a scientific context poses unique challenges. Many traditional software development paradigms demand an upfront articulation of goals and requirements. This allows the developers to carefully design their software, even before a single line of code is written. In her seminal 2005

case study Segal [8] describes a collaboration between a team of researchers and a contracted team of software engineers. Ultimately

5.1 Overview

In the Wright Group, PyCMDS replaces the old acquisition softwares 'ps control', written by Kent Meyer and 'Control for Lots of Research in Spectroscopy' written by Schuyler Kain.

5.2 WrightTools

WrightTools is a software package at the heart of all work in the Wright Group.

5.3 PyCMDS

PyCMDS directly addresses the hardware during experiments.

5.3.1 Overview

PyCMDS has, through software improvements alone, dramatically lessened scan times...

- → simultaneous motor motion
- → digital signal processing
- → ideal axis positions 5.3.2

5.3.2 Ideal Axis Positions

Frequency domain multidimensional spectroscopy is a time-intensive process. A typical pixel takes between one-half second and three seconds to acquire. Depending on the exact hardware being scanned and signal being detected, this time may be mostly due to hardware motion or signal collection. Due to the curse of dimensionality, a typical three-dimensional CMDS experiment contains roughly 100,000 pixels. CMDS hardware is transiently-reliable, so speeding up experiments is a crucial component of unlocking ever larger dimensionalities and higher resolutions.

One obvious way to decrease the scan-time is to take fewer pixels. Traditionally, multidimensional scans are done with linearly arranged points in each axis—this is the simplest configuration to program into the acquisition software. Because signal features are often sparse or slowly varying (especially so in high-dimensional scans) linear stepping means that *most of the collected pixels* are duplicates or simply noise. A more intelligent choice of axis points can capture the same nonlinear spectrum in a fraction of the total pixel count.

An ideal distribution of pixels is linearized in *signal*, not coordinate. This means that every signal level (think of a contour in the N-dimensional case) has roughly the same number of pixels defining it. If some generic multidimensional signal goes between 0 and 1, one would want roughly 10% of the pixels to be between 0.9 and 1.0, 10% between 0.8 and 0.9 and so on. If the signal is sparse in the space explored (imagine a narrow two-dimensional Lorentzian in the center of a large 2D-Frequency scan) this would place the majority of the pixels near the narrow peak feature(s), with only a few of them defining the large (in axis space) low-signal floor. In contrast linear stepping would allocate the vast majority of the pixels in the low-signal 0.0 to 0.1 region, with only a few being used to capture the narrow peak feature. Of course, linearizing pixels in signal requires prior expectations about the shape of the multidimensional signal—linear stepping is still an appropriate choice for low-resolution "survey" scans.

CMDS scans often posses correlated features in the multidimensional space. In order to capture such features as cheaply as possible, one would want to define regions of increased pixel density along the correlated (diagonal) lineshape. As a concession to reasonable simplicity, our acquisition software

(PyCMDS) assumes that all scans constitute a regular array with-respect-to the scanned axes. We can acquire arbitrary points along each axis, but not for the multidimensional scan. This means that we cannot achieve strictly ideal pixel distributions for arbitrary datasets. Still, we can do much better than linear spacing.

Almost all CMDS lineshapes (in frequency and delay) can be described using just a few lineshape functions:

- → exponential
- → Gaussian
- → Lorentzian
- → bimolecular

Exponential and bimolecular dynamics fall out of simple first and second-order kinetics (I will ignore higher-order kinetics here). Gaussians come from our Gaussian pulse envelopes or from normally-distributed inhomogeneous broadening. The measured line-shapes are actually convolutions of the above. I will ignore the convolution except for a few illustrative special cases. More exotic lineshapes are possible in CMDS—quantum beating and breathing modes, for example—I will also ignore these. Derivations of the ideal pixel positions for each of these lineshapes appear below.

5.3.3 Exponential

Simple exponential decays are typically used to describe population and coherence-level dynamics in CMDS. For some generic exponential signal S with time constant τ,

$$S(t) = \mathrm{e}^{-\frac{t}{\tau}}\,. \tag{5.1}$$

We can write the conjugate equation to 5.1, asking "what t do I need to get a certain signal level?":

$$\log(S) = -\frac{t}{\tau} \tag{5.2}$$

$$t = -\tau \log(S). \tag{5.3}$$

So to step linearly in t, my step size has to go as $-\tau \log(S)$.

We want to go linearly in signal, meaning that we want to divide S into even sections. If S goes from 0 to 1 and we choose to acquire N points,

$$t_n = -\tau \log\left(\frac{n}{N}\right). \tag{5.4}$$

Note that t_n starts at long times and approaches zero delay. So the first t_1 is the smallest signal and t_N is the largest.

Now we can start to consider realistic cases, like where τ is not quite known and where some other longer dynamics persist (manifested as a static offset). Since these values are not separable in a general system, I'll keep S normalized between 0 and 1.

$$S = (1-c)\,\mathrm{e}^{-\frac{t}{\tau_{\text{actual}}}} + c \tag{5.5}$$

$$S_n = (1-c)\,\mathrm{e}^{-\frac{-\tau_{\text{step}} \log\left(\frac{n}{N}\right)}{\tau_{\text{actual}}}} + c \tag{5.6}$$

$$S_n = (1-c)\,\mathrm{e}^{-\frac{\tau_{\text{step}}}{\tau_{\text{actual}}} \log\left(\frac{N}{n}\right)} + c \tag{5.7}$$

$$S_n = (1-c)\left(\frac{N}{n}\right)^{-\frac{\tau_{\text{step}}}{\tau_{\text{actual}}}} + c \tag{5.8}$$

$$S_n = (1-c)\left(\frac{n}{N}\right)^{\frac{\tau_{\text{step}}}{\tau_{\text{actual}}}} + c \tag{5.9}$$

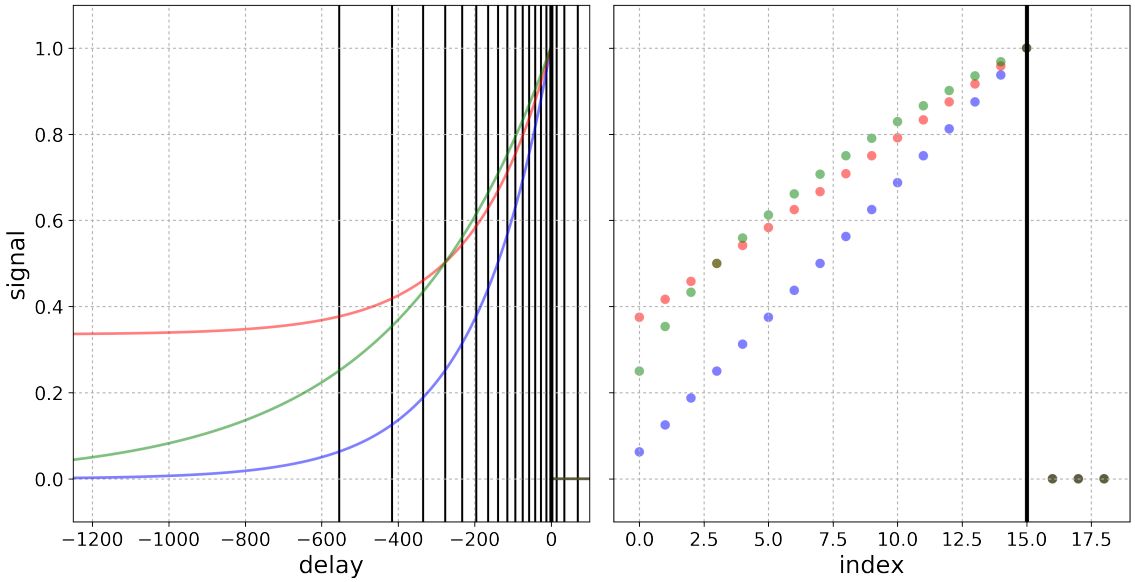

Figure 5.1: TODO

Gaussian

Lorentzian

Bimolecular

5.4 WrightSim

WrightSim does simulations.

Chapter 6

Instrumental Development

6.1 Hardware

6.1.1 Delay Stages

6.2 Signal Acquisition

Old boxcar: 300 ns window, 10 micosecond delay. Onset of saturation 2 V.

6.2.1 Digital Signal Processing

6.3 Artifacts and Noise

6.3.1 Scatter

Scatter is a complex microscopic process whereby light traveling through a material elastically changes its propagation direction. In CMDS we use propagation direction to isolate signal. Scattering samples

defeat this isolation step and allow some amount of excitation light to reach the detector. In homodyne-detected 4WM experiments,

$$I_{\text{detected}} = |E_{4\text{WM}} + E_1 + E_2 + E_{2'}|^2 \tag{6.1}$$

Where E is the entire time-dependent complex electromagnetic field. When expanded, the intensity will be composed of diagonal and cross terms:

$$\begin{aligned} I_{\text{detected}} = \overline{(E_1 + E_2)} E_{2'} + (E_1 + E_2)\overline{E_{2'}} + |E_1 + E_2|^2 + (E_1 + E_2)\overline{E_{4\text{WM}}} \\ +(E_1 + E_2)\overline{E_{4\text{WM}}} + \overline{E_{2'}} E_{4\text{WM}} + E_{2'}\overline{E_{4\text{WM}}} + |E_{4\text{WM}}|^2 \end{aligned} \tag{6.2}$$

A similar expression in the case of heterodyne-detected 4WM is derived by Brixner et al. [9]. The goal of any 'scatter rejection' processing procedure is to isolate $|E_{4\text{WM}}|^2$ from the other terms.

Abandon the Random Phase Approximation

Interference Patterns in TrEE

TrEE is implicitly homodyne-detected. Scatter from excitation fields will interfere on the amplitude level with TrEE signal, causing interference patterns that beat in delay and frequency space. The pattern of beating will depend on which excitation field(s) reach(es) the detector, and the parameterization of delay space chosen.

First I focus on the interference patterns in 2D delay space where all excitation fields and the detection field are at the same frequency.

Here I derive the slopes of constant phase for the old delay space, where d1 = $\tau_{2'1}$ and d2 = τ_{21}. For simplicity, I take τ_1 to be 0, so that $\tau_{21} \rightarrow \tau_2$ and $\tau_{2'1} \rightarrow \tau_{2'}$. The phase of signal is then

$$\Phi_{\text{sig}} = \mathrm{e}^{-((\tau_{2'} - \tau_2)\omega)} \tag{6.3}$$

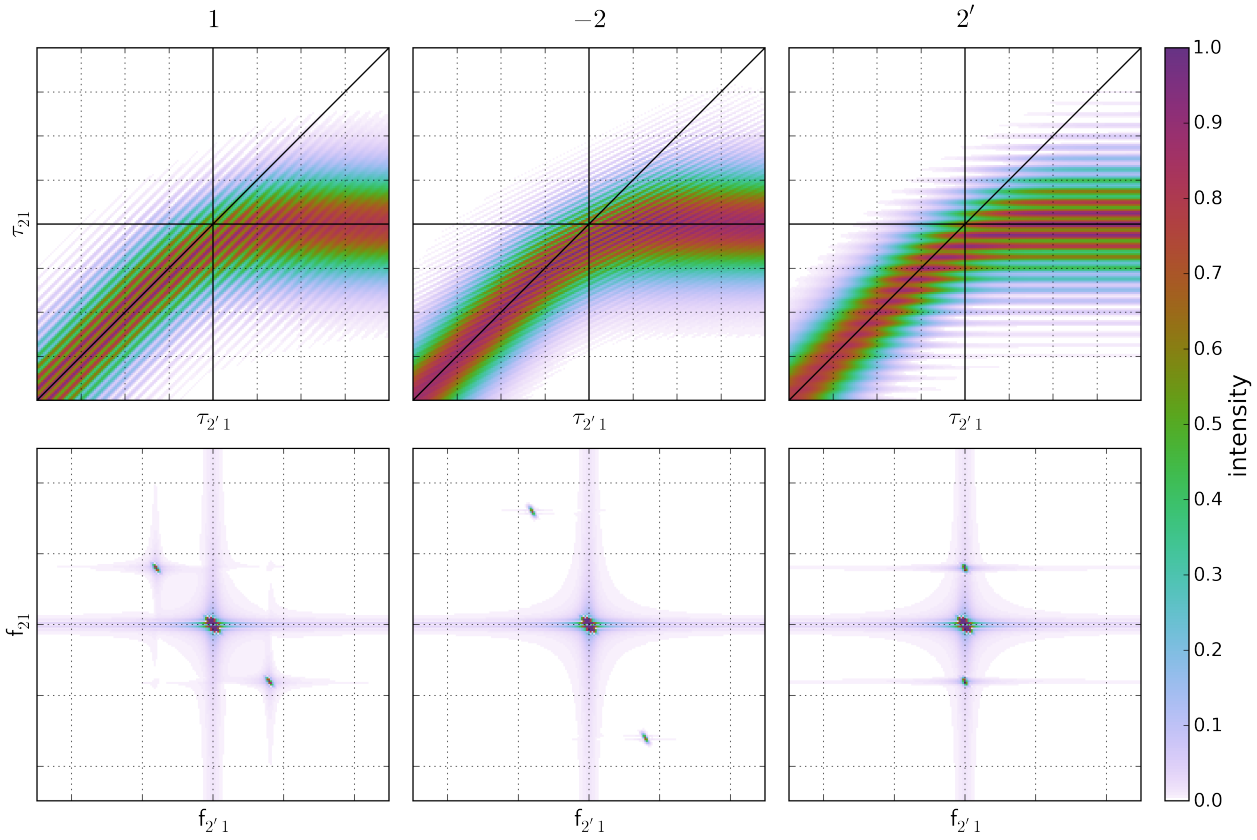

Figure 6.1: Numerically simulated interference patterns between scatter and TrEE for the old delay parametrization. Each column has scatter from a single excitation field. The top row shows the measured intensities, the bottom row shows the 2D Fourier transform, with the colorbar's dynamic range chosen to show the cross peaks.

The phase of each excitation field can also be written:

$$\Phi_1 = e^0 \tag{6.4}$$

$$\Phi_2 = e^{-\tau_2\omega} \tag{6.5}$$

$$\Phi_{2'} = e^{-\tau_{2'}\omega} \tag{6.6}$$

The cross term between scatter and signal is the product of Φ_{sig} and $\Phi_{scatter}$. The cross terms are:

$$\Delta_1 = \Phi_{sig} = e^{-((\tau_{2'}-\tau_2)\omega)} \tag{6.7}$$

$$\Delta_2 = \Phi_{sig}e^{-\tau_2\omega} = e^{-((\tau_{2'}-2\tau_2)\omega)} \tag{6.8}$$

$$\Delta_{2'} = \Phi_{sig}e^{-\tau_{2'}\omega} = e^{-\tau_2\omega} \tag{6.9}$$

Figure 6.1 presents numerical simulations of scatter interference as a visual aid. See Yurs 2011 [10].

Here I derive the slopes of constant phase for the current delay space, where d1 = $\tau_{22'}$ and d2 = τ_{21}. I take τ_2 to be 0, so that $\tau_{22'} \rightarrow \tau_{2'}$ and $\tau_{21} \rightarrow \tau_1$. The phase of the signal is then

$$\Phi_{sig} = e^{-((\tau_{2'}+\tau_1)\omega)} \tag{6.10}$$

The phase of each excitation field can also be written:

$$\Phi_1 = e^{-\tau_1\omega} \tag{6.11}$$

$$\Phi_2 = e^0 \tag{6.12}$$

$$\Phi_{2'} = e^{-\tau_{2'}\omega} \tag{6.13}$$

The cross term between scatter and signal is the product of Φ_{sig} and $\Phi_{scatter}$. The cross terms are:

$$\Delta_1 = \Phi_{sig}e^{-\tau_1\omega} = e^{-\tau_{2'}\omega} \tag{6.14}$$

$$\Delta_2 = \Phi_{sig} = e^{-((\tau_2+\tau_1)\omega)} \tag{6.15}$$

$$\Delta_{2'} = \Phi_{sig}e^{-\tau_{2'}\omega} = e^{-\tau_1\omega} \tag{6.16}$$

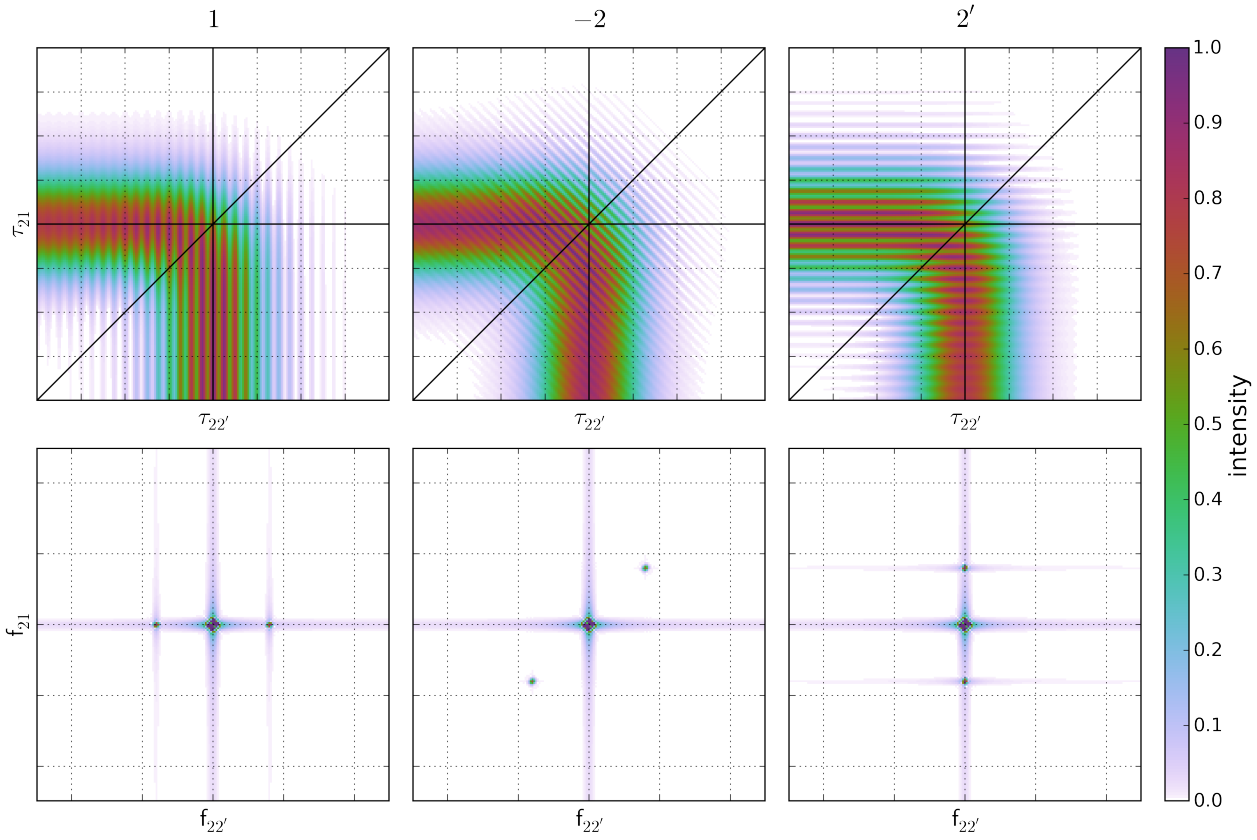

Figure 6.2: Numerically simulated interference patterns between scatter and TrEE for the current delay parametrization. Each column has scatter from a single excitation field. The top row shows the measured intensities, the bottom row shows the 2D Fourier transform, with the colorbar's dynamic range chosen to show the cross peaks.

Figure 6.2 presents numerical simulations of scatter interference for the current delay parameterization.

Instrumental Removal of Scatter

The effects of scatter can be entirely removed from CMDS signal by combining two relatively straightforward instrumental techniques: *chopping* and *fibrillation*. Conceptually, chopping removes intensity-level offset terms and fibrillation removes amplitude-level interference terms. Both techniques work by modulating signal and scatter terms differently so that they may be separated after light collection.

	A	B	C	D
signal			✓	
scatter 1		✓	✓	
scatter 2			✓	✓
other	✓	✓	✓	✓

Table 6.1: Four shot-types in a general phase shifted parallel modulation scheme. The 'other' category represents anything that doesn't depend on either chopper, including scatter from other excitation sources, background light, detector voltage offsets, etc.

We use the dual chopping scheme developed by Furuta, Fuyuki, and Wada [11] called 'phase shifted parallel modulation'. In this scheme, two excitation sources are chopped at 1/4 of the laser repetition rate (two pulses on, two pulses off). Very similar schemes are discussed by Augulis and Zigmantas [12] and Heisler et al. [13] for two-dimensional electronic spectroscopy. The two chop patterns are phase-shifted to make the four-pulse pattern represented in Table 6.1. In principle this chopping scheme can be achieved with a single judiciously placed mechanical chopper - this is one of the advantages of Furuta's scheme. Due to practical considerations we have generally used two choppers, one on each OPA. The key to phase shifted parallel modulation is that signal only appears when both of your chopped beams are passed. It is simple to show how signal can be separated through simple addition and subtraction of the A, B, C, and D phases shown in Table 6.1. First, the components of each phase:

$$A = I_{\text{other}} \tag{6.17}$$

$$B = I_1 + I_{\text{other}} \tag{6.18}$$

$$C = I_{\text{signal}} + I_1 + I_2 + I_{\text{other}} \tag{6.19}$$

$$D = I_2 + I_{\text{other}} \tag{6.20}$$

Grouping into difference pairs,

$$A - B = -I_1 \tag{6.21}$$

$$C - D = I_{\text{signal}} + I_1 \tag{6.22}$$

So:

$$A - B + C - D = I_{\text{signal}} \tag{6.23}$$

I have ignored amplitude-level interference terms in this treatment because they cannot be removed via any chopping strategy. Interference between signal and an excitation beam will only appear in 'C'-type shots, so it will not be removed in Equation 6.23. To remove such interference terms, you must *fibrillate* your excitation fields.

An alternative to dual chopping is single-chopping and 'leveling'... this technique was used prior to May 2016 in the Wright Group... 'leveling' and single-chopping is also used in some early 2DES work... [9].

Figure 6.3 shows the effects of dual chopping for some representative MoS_2 TA data. Each subplot is a probe wigner, with the vertical grey line representing the pump energy. Note that the single chopper passes pump scatter, visible as a time-invariant increase in intensity when the probe and monochromator are near the pump energy. Dual chopping efficiently removes pump scatter, but at the cost of signal to noise for the same number of laser shots. Taking twice as many laser shots when dual chopping brings the signal to noise to at least as good as the original single chopping.

Fibrillation is the intentional randomization of excitation phase during an experiment. Because the interference term depends on the phase of the excitation field relative to the signal, averaging over many shots with random phase will cause the interference term to approach zero. This is a well known strategy for removing unwanted interference terms [14, 15].

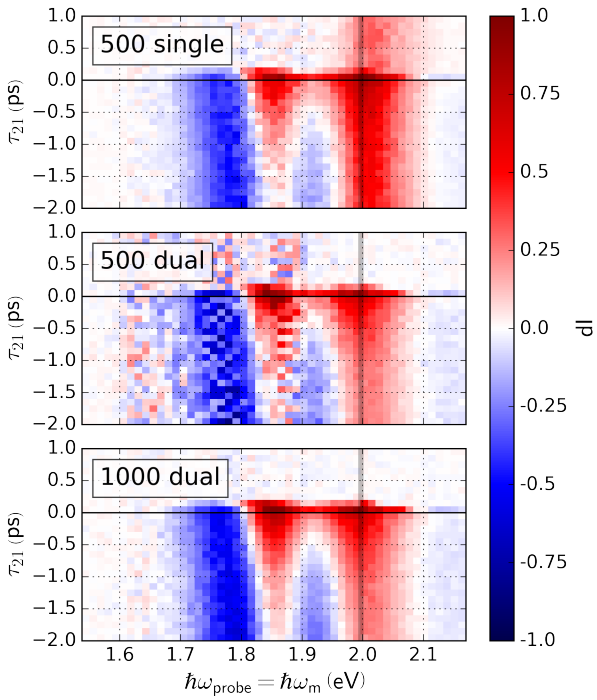

Figure 6.3: Comparison of single and dual chopping in a MoS_2 transient absorption experiment. Note that this data has not been processed in any way - the colorbar represents changes in intensity seen by the detector. The grey line near 2 eV represents the pump energy. The inset labels are the number of laser shots taken and the chopping strategy used.

6.3.2 Normalization of dual-chopped self-heterodyned signal

Shot-by-shot normalization is not trivial for these experiments. As in table above, with 1 as pump and 2 as probe.

Starting with ΔI from 6.23, we can normalize by probe intensity to get the popular $\Delta I/I$ representation. Using the names defined above:

$$\frac{\Delta I}{I} = \frac{A - B + C - D}{D - A} \tag{6.24}$$

Now consider the presence of excitation intensity monitors, indicated by subscripts PR for probe and PU for pump.

We can further normalize by the pump intensity by dividing the entire expression by C_{PU}:

$$\frac{\Delta I}{I} = \frac{A - B + C - D}{(D - A) * C_{PU}} \tag{6.25}$$

Now, substituting in BRAZARD formalism:

$$A = constant \tag{6.26}$$

$$B = SI^{B}_{PU}(1 + \delta^{B}_{PU}) \tag{6.27}$$

$$C = I^{C}_{PR}(1 + \delta^{C}_{PR}) + SI^{C}_{PU}(1 + \delta^{C}_{PR}) \tag{6.28}$$

$$D = I^{D}_{PR}(1 + \delta^{D}_{PR}) \tag{6.29}$$

$$\frac{\Delta I}{I} = \frac{< A > - \frac{<B_{PU}>B}{B_{PU}} + \frac{<C_{PU}><C_{PR}C}{C_{PU}C_{PR}} - \frac{<D_{PR}>D}{D_{PR}}}{< PR >< PU >} \tag{6.30}$$

6.4 Light Generation

6.4.1 Automated OPA Tuning

6.5 Optomechanics

6.5.1 Automated Neutral Density Wheels

Part III

Applications

Chapter 7

PbSe

Chapter 8

MX2

We report the first coherent multidimensional spectroscopy study of a MoS_2 film. A four-layer sample of MoS_2 was synthesized on a silica substrate by a simplified sulfidation reaction and characterized by absorption and Raman spectroscopy, atomic force microscopy, and transmission electron microscopy. State-selective coherent multidimensional spectroscopy (CMDS) on the as-prepared MoS_2 film resolved the dynamics of a series of diagonal and cross-peak features involving the spin—orbit split A and B excitonic states and continuum states. The spectra are characterized by striped features that are similar to those observed in CMDS studies of quantum wells where the continuum states contribute strongly to the initial excitation of both the diagonal and cross-peak features, while the A and B excitonic states contributed strongly to the final output signal. The strong contribution from the continuum states to the initial excitation of both the diagonal and cross-peak features, while the A and B excitonic states contributed strongly to the final output signal. The strong contribution from the continuum states to the initial excitation shows that the continuum states are coupled to the A and B excitonic states and that fast intraband relaxation is occurring on a sub-70 fs time scale. A comparison of the CMDS excitation signal and the absorption spectrum shows that the relative importance of the continuum states is determined primarily by their absorption strength. Diagonal and cross-peak features decay with a 680 fs time constant characteristic of exciton recombination and/or trapping. The short time dynamics are complicated by coherent and partially coherent pathways that become important when the excitation pulses are temporally overlapped. In this region, the coherent dynamics create diagonal

features involving both the excitonic states and continuum states, while the partially coherent pathways contribute to cross-peak features.

8.1 Introduction

Transition metal dichalcogenides (TMDCs), such as MoS_2, are layered semiconductors with strong spin-orbit coupling, high charge mobility, and an indirect band gap that becomes direct for monolayers. [16, 17] The optical properties are dominated by the A and B excitonic transitions between two HOMO spin-orbit split valence bands and the lowest state of the conduction band at the K and K' valleys of the two-dimensional hexagonal Brillouin zone. [18] The spin and valley degrees of freedom are coupled in individual TMDC layers as a result of the strong spin-orbit coupling and the loss of inversion symmetry. The coupling suppresses spin and valley relaxation since both spin and valley must change in a transition. These unusual properties have motivated the development of TMDC monolayers for next-generation nano/optoelectronic devices as well as model systems for spintronics and valleytronics applications. [17, 19, 20]

Ultrafast dynamics of the MoS_2 A and B electronic states have been measured by pump-probe, transient absorption, and transient reflection spectroscopy. [21, 4, 22, 23, 24] The spectra contain A and B excitonic features that result from ground-state bleaching (GSB), stimulated emission (SE), and excited-state absorption (ESA) pathways. The excitons exhibit biexponential relaxation times of $\approx$10–20 and $\approx$350–650 fs, depending on the fluence and temperature. The dependence on excitation frequency has not been explored in previous ultrafast experiments on MoS_2, but it has played a central role in understanding exciton cooling dynamics and exciton-phonon coupling in studies of quantum dots. [25]

Coherent multidimensional spectroscopy (CMDS) is a complementary four wave mixing (FWM) methodology that differs from pump-probe, transient absorption, and transient reflection methods. [20, 21, 4, 22, 24, 26, 23] Rather than measuring the intensity change of a probe beam caused by the state population changes induced by a pump beam, CMDS measures the intensity of a coherent output beam created by interactions with three excitation pulses. The interest in CMDS methods arise from their ability to remove inhomogeneous broadening, define interstate coupling, and resolve coherent and

incoherent dynamics. [27, 28, 29, 10, 30, 31, 32, 33, 34] CMDS typically requires interferometric phase stability between excitation pulses, so CMDS has been limited to materials with electronic states within the excitation-pulse bandwidth. Multiresonant CMDS is a particularly attractive method for the broader range of complex materials because it does not require interferometric stability and is able to use independently tunable excitation pulses over wide frequency ranges.

The multiresonant CMDS used in this work employs two independently tunable excitation beams with frequencies ω_1 and ω_2. The ω_2 beam is split into two beams, denoted by ω_2 and ω_2'. These three beams are focused onto the MoS_2 thin film at angles, creating an output beam in the phase-matched direction $\mathbf{k}_{out} = \mathbf{k}_1 - \mathbf{k}_2 + \mathbf{k}_{2'}$ where $\mathbf{k}$ is the wave vector for each beam and the subscripts label the excitation frequencies. Multidimensional spectra result from measuring the output intensity dependence on frequency and delay times.

Figure 8.1 introduces our conventions for representing multidimensional spectra. Figure 8.1b,d are simulated data. Figure 8.1a shows one of the six time orderings of the three excitation pulses where $\tau_{22'} \equiv t_2 - t_{2'} > 0$ and $\tau_{21} \equiv t_2 - t_1 < 0$; that is, the $\omega_{2'}$ pulse interacts first and the ω_1 pulse interacts last. Figure 8.1b illustrates the 2D delay-delay spectrum for all six time orderings when ω_1 and ω_2 are both resonant with the same state. The color denotes the output amplitude. Along the negative ordinate where $\tau_{22'} = 0$, interactions with the ω_2 and $\omega_{2'}$ pulses create a population that is probed by ω_1. Similarly, along the negative absicissa where $\tau_{21} = 0$, interactions with the ω_2 and ω_1 pulses create a population that is probed by $\omega_{2'}$. The decay along these axes measures the population relaxation dynamics. Note that these delay representations differ from previous publications by our group. [35] This paper specifically explores the dynamics along the ordinate where $\tau_{22'}$ is zero and the τ_{21} delay is changed.

Figure 8.1c depicts the A and B excitonic transitions between the spin-orbit split valence bands and the degenerate conduction band states of MoS_2. Figure 8.1d illustrates the 2D frequency-frequency spectrum when ω_1 and ω_2 are scanned over two narrow resonances. The spectrum contains diagonal and cross-peaks that we label according to the excitonic resonances AA, AB BA, and BB for illustrative purposes. The dynamics of the individual quantum states are best visualized by 2D frequency-delay plots, which combine the features seen in Figure 8.1b,d.

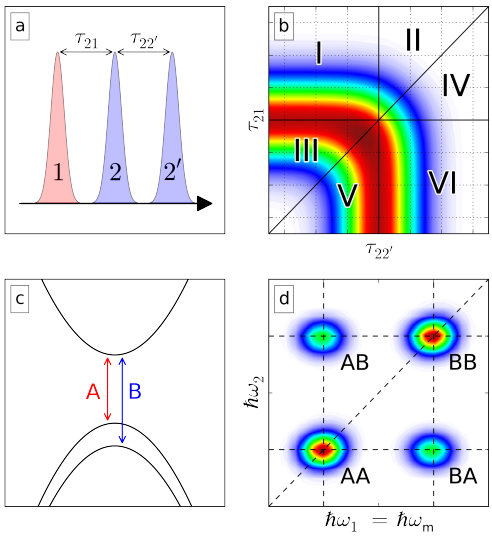

Figure 8.1: (a) Example delays of the ω_1, ω_2, and $\omega_{2'}$ excitation pulses. (b) Dependence of the output intensity on the $\tau_{22'}$ and τ_{21} time delays for $\omega_1 = \omega_2$. The solid lines define the regions for the six different time orderings of the ω_1, ω_2, and $\omega_{2'}$ excitation pulses. We have developed a convention for numbering these time orderings, as shown. (c) Diagram of the band structure of MoS_2 at the K point. The A and B exciton transitions are shown. (d) Two dimensional frequency-frequency plot labeling two diagonal and cross-peak features for the A and B excitons.

This works reports the first multiresonant CMDS spectra of MoS_2. It includes the excitation frequency dependence of the A and B excitonic-state dynamics. These experiments provide a fundamental understanding of the multidimensional MoS_2 spectra and a foundation for interpreting CMDS experiments on more complex TMDC heterostructures. The experimental spectra differ from the simple 2D spectrum shown in Figure 8.1d and those of earlier CMDS experiments with model systems. The line shape of the CMDS excitation spectrum closely matches the absorption spectrum, but the line shape of the output coherence is dominated by the A and B excitonic features. The difference arises from fast, $<$ 70 fs intraband relaxation from the hot A and B excitons of the continuum to the band edge. A longer, 680 fs relaxation occurs because of trapping and/or exciton dynamics. [24] The intensity of the cross-peaks depends on the importance of state filling and intraband relaxation of hot A excitons as well as the presence of interband population trnasfer of the A and B exciton states.

8.2 Methods

MoS_2 thin films were prepared *via* a Mo film sulfidation reaction, similar to methods reported by Laskar et al. [36]. A 1 nm amount of Mo (Kurt J. Lesker, 99.95%) metal was electron-beam evaporated onto a fused silica substrate at a rate of 0.05 Å/s. The prepared Mo thin films were quickly transferred to the center of a 1-inch fused silica tub furnace equipped with gas flow controllers (see Figure 8.2) and purged with Ar. The temperature of the Mo substrate was increased to 900 $^{\circ}$C over the course of 15 min, after which 200 mg of sulfur was evaporated into the reaction chamber. Sulfidation was carried out for 30 min, and the furnace was subsequently cooled to room temperature; then the reactor tube was returned to atmospheric pressure, and the MoS_2 thin film samples were collected. The MoS_2 samples were characterized and used for CMDS experiments with no further preparation.

MoS_2 thin film absorption spectra were collected by a Shimadzu 2401PC ultraviolet-visible spectrophotometer. Raman and photoluminescence experiments were carried out in parallel using a Thermo DXR Raman microscope with a 100x 0.9 NA focusing objective and a 2.0 mW 532 nm excitation source. Raman/PL measurements were intentionally performed at an excitation power of $<$8.0 mW to prevent sample damage. [37] Contact-mode atomic foce microscopy was performed with an Agilent 5500 AFM.

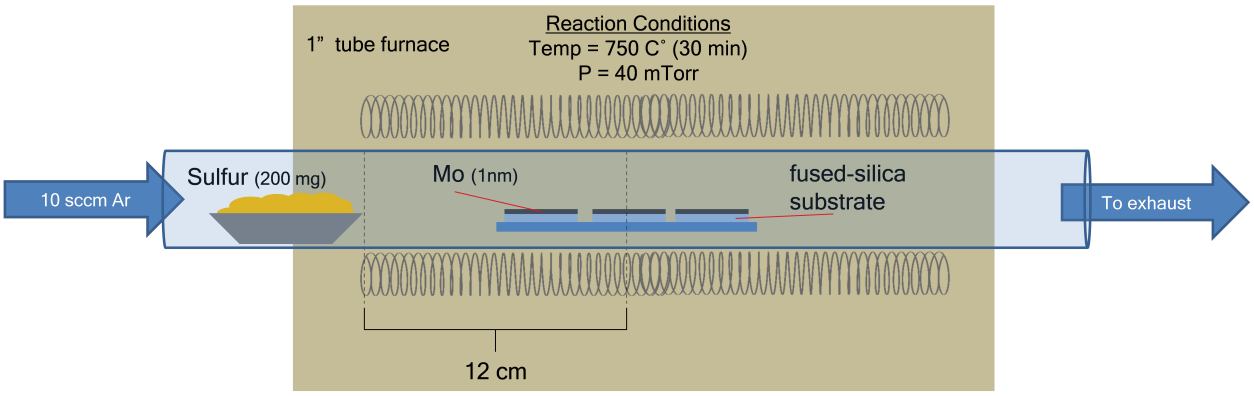

Figure 8.2: Schemiatic of the synthetic setup used for Mo thin film sulfidation reactions.

MoS_2 film thickness was determined by scratching the sample to provide a clean step-edge between the MoS_2 film and the fused silica substrate. TEM samples were prepared following the method outlined by Shanmugam, Durcan, and Yu [38] using concentrated KOH in a 35 °C oil bath for 20 minutes. The delaminated MoS_2 sample was removed from the basic solution, rinsed five times with DI water, and transferred to a Cu-mesh TEM grid. TEM experiments were performed on a FEI Titan aberration corrected (S)TEM under 200 kV accelerating voltage.

The coherent multidimensional spectroscopy system used a 35 fs seed pulse, centered at 800 nm and generated by a 1 kHz Tsunami Ti-sapphire oscillator. The seed was amplified by a Spitfire-Pro regenerative amplifier. The amplified output was split to pump two TOPAS-C collinear optical parametric amplifiers. OPA signal output was immediately frequency doubled with BBO crystals, providing two $\approx$50 fs independently tunable pulses denoted ω_1 and ω_2 with frequencies ranging from 1.62 to 2.12 eV. Signal and idler were not filtered out, but played no role due to their low photon energy. Pulse ω_2 was split into pulses labeled ω_2 and $\omega_{2'}$ to create a total of three excitation pulses.

In this experiment we use motorized OPAs which allow us to set the output color in software. OPA1 and OPA2 were used to create the ω_1 and ω_2 frequencies, respectively. In Figure 8.4 we compare the spectral envelope generated by the OPA at each set color. Negative detuning values correspond to regions of the envelope lower in energy than the corresponding set color. The colorbar allows for comparison between set color intensities. The fluence values reported correspond to the brightest set color for each OPA. A single trace of OPA2 output at set color = 1.95 eV can be found in Figure 8.7.

After passing through automated delay stages (Newport SMC100 actuators), all three beams were focused onto the sample surface by a 1 meter focal length spherical mirror in a distorted BOXCARS geometry to form a 630, 580, and 580 μm FWHM spot sizes for ω_1, ω_2, and $\omega_{2'}$, respectively.

Figure 8.5 represents delay corrections applied for each OPA. The corrections were experimentally determined using driven FWM output from fused silica. Corrections were approximately linear against photon energy, in agreement with the normal dispersion of transmissive optics inside our OPAs and between the OPAs and the sample. OPA2 required a relatively small correction along $\tau_{22'}$ (middle subplot) to account for any dispersion experienced differently between the two split beams. OPA1 was not split and

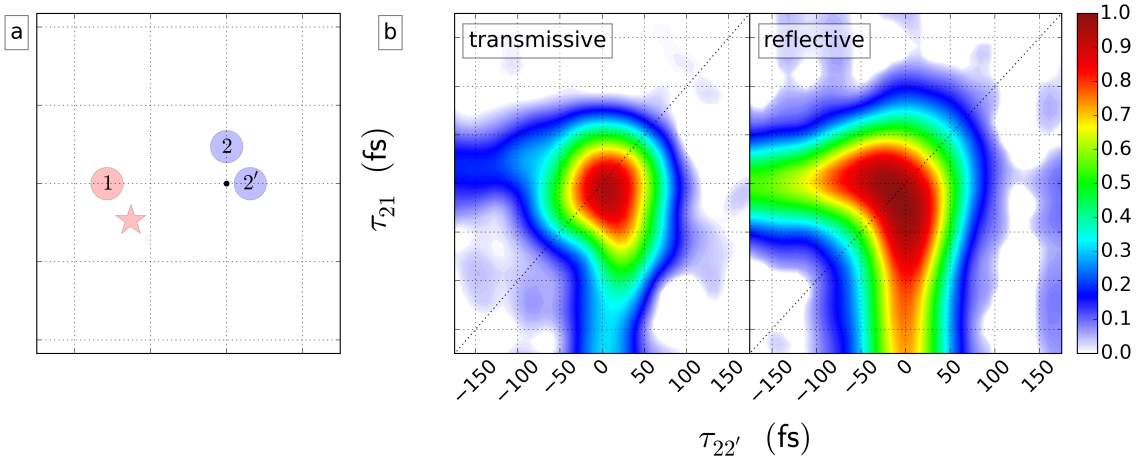

Figure 8.3: (a) Mask. (b) 2D delay spectra at the BB diagonal ($\omega_1 = \omega_2 \approx 1.95$ eV) for transmissive and reflective geometries. Transmissive signal is a mixture of MoS_2 signal and a large amount of driven signal from the substrate that only appears in the pulse overlap region. Reflective signal is representative of the pure MoS_2 response.

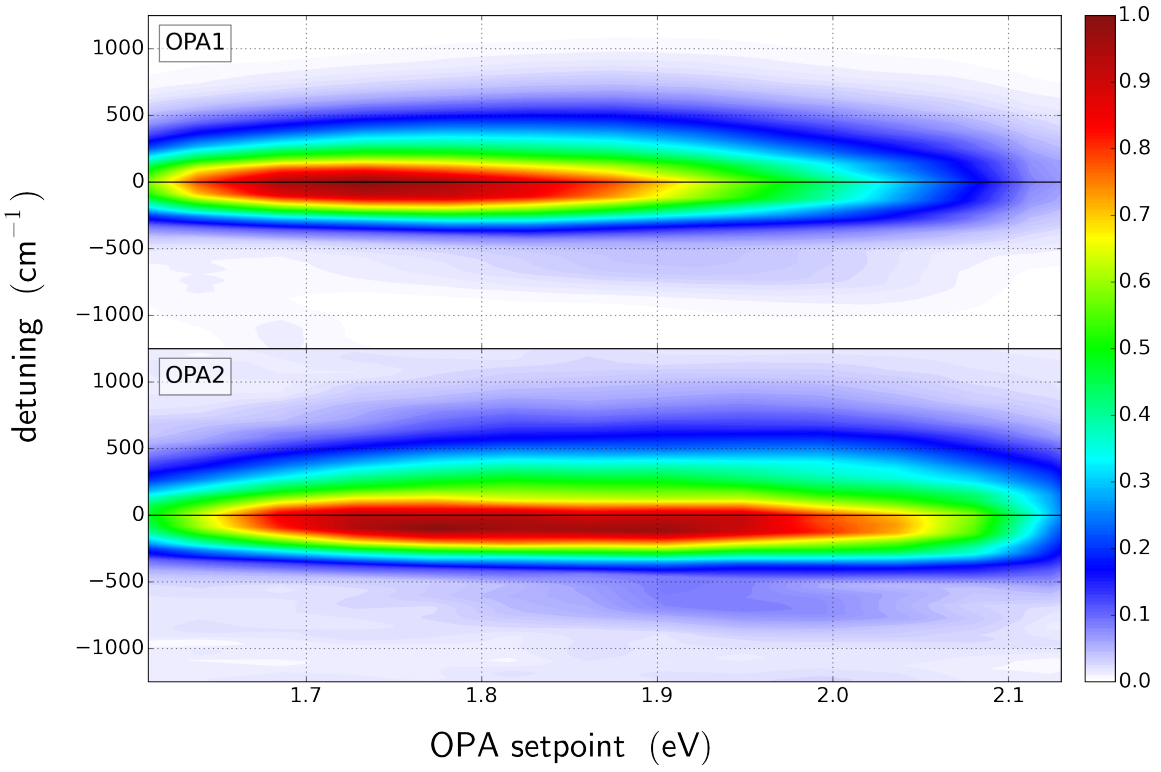

Figure 8.4: OPA outputs at each color explored.

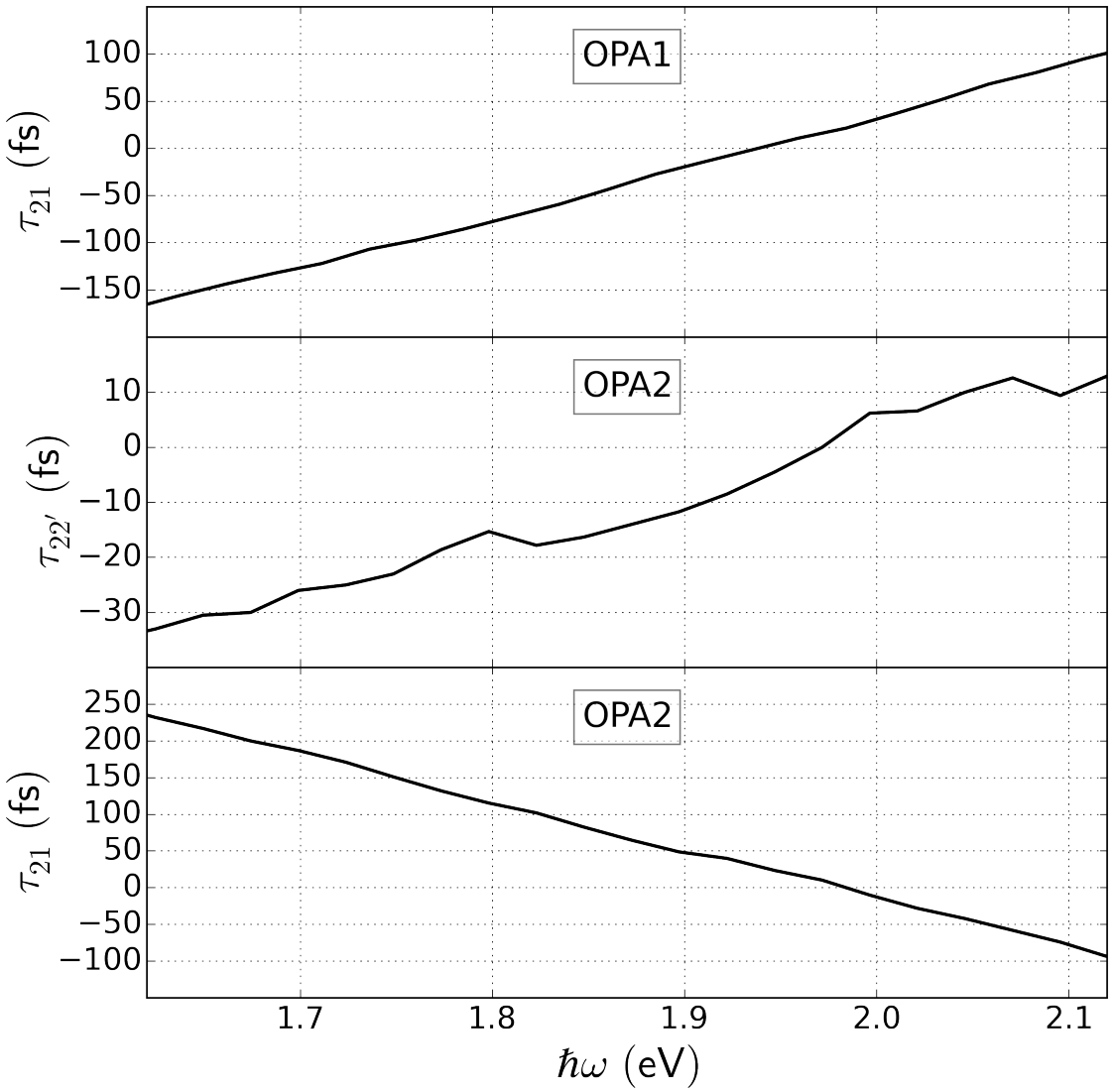

Figure 8.5: Spectral delay correction.

therefore needed no such correction.

Figure 8.3a represents the to-scale mask that defines our distorted BOXCARS configuration. Relative to the center of the BOXCARS mask (small black dot), ω_1, ω_2, and $\omega_{2'}$ enter the sample at angles of 5.0, 1.5, and 1.0 degrees. Each is angled only along the vertical or horizontal dimension, as indicated in Figure 8.3a. This distortion allowed us to remove a large amount of unwanted ω_2 and $\omega_{2'}$ photons from our signal path (Figure 8.3a red star). ω_1 photons were less efficiently rejected, as we show below. The center of the BOXCARS mask was brought into the sample at $\approx$45 degrees. All three beams had S polarization. After reflection, the output beam was isolated using a series of apertures, spectrally resolved with a monochromator (spectral resolution 9 meV). and detected using a photomultiplier (RCA C31034A).

Our experimental setup allowed for the collection of both transmissive and reflective (epi-directional) FWM signal. The 2D delay spectra in Figure 8.3b show the presence of a large nonresonant contribution at the origin for the transmissive FWM signal and weaker signals from the MoS_2 thin film at negative values of τ_{21} and $\tau_{22'}$. The nonresonant contribution is much weaker than the signals from the film for the reflective signal id is the geometry chosen for this experiment. This discrimination between a film and the substrate was also seen in reflective and transmissive CARS microscopy experiments. [39]

Once measured, the FWM signal was sent through a four-stage workup process to create the data set shown here. This workup procedure is visualized in Figure 8.6. We use a chopper and boxcar in active background subtraction mode (averaging 100 laser shots) to extract the FWM signal from ω_1 and ω_2 scatter. We collect this differential signal (Figure 8.6b) in software with an additional 50 shots of averaging. In post-process we subtract ω_2 scatter and smooth the data using a 2D Kaiser window. Finally, we represent the homodyne collected data as $(\text{sig})^{1/2}$ to make the dynamics and line widths comparable to heterodyne-collected techniques like absorbance and pump-probe spectra. Throughout this work, zero signal on the color bar is set to agree with the average rather than the minimum of noise. Values below zero due to measurement uncertainty underflow the color bar and are plotted in white. This is especially evident in lots such as +120 fs in Figure 8.14, where there is no real signal. IPython [40] and matplotlib [41] were important for data processing and plotting in this work.

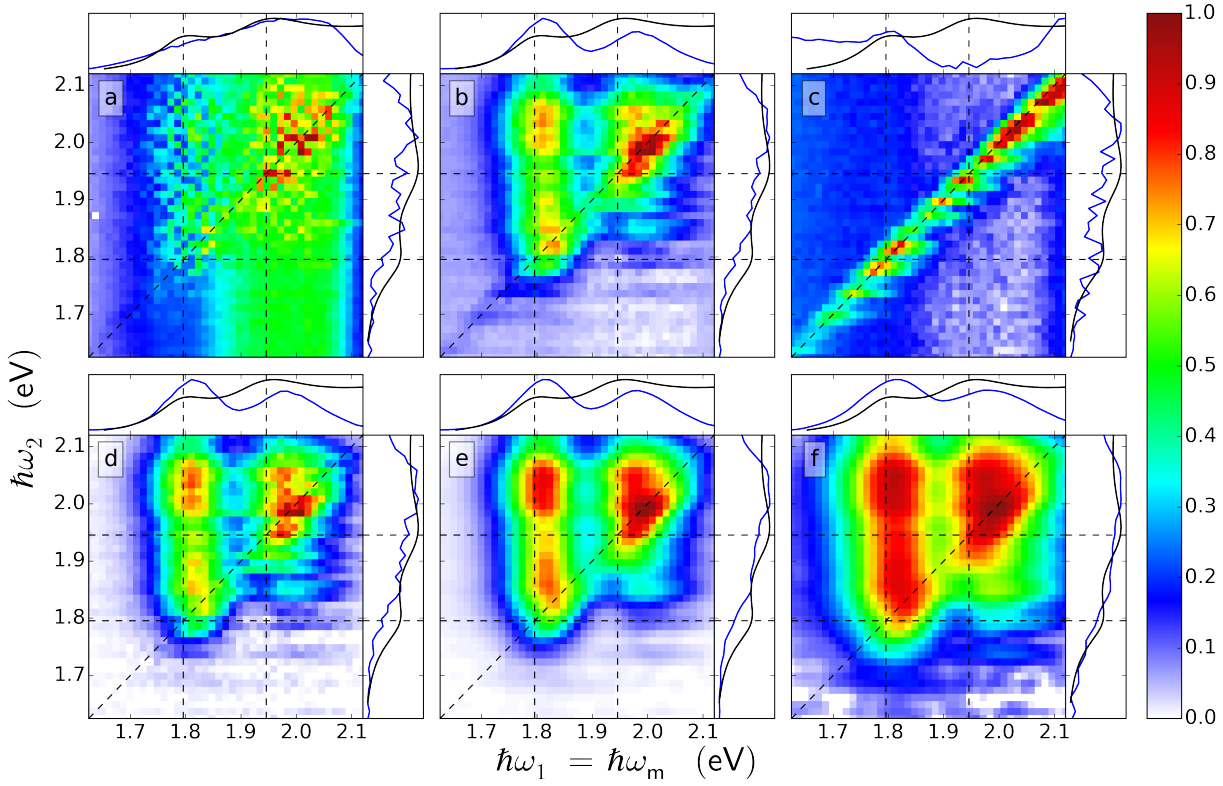

Figure 8.6: Visualization of data collection and processing. With the exception of (c), each subsequent pane represents an additional processing step on top of previous processing. The color bar of each image is separate. (a) Voltages read by the detector at teach color combination. The large vertical feature is ω_1 scatter; the shape is indicative of the power curve of the OPA. MoS_2 response can be barely seen above this scatter. (b) Data after chopping and active background subtraction at the boxcar (100 shots). (c) The portion of chopped signal that is not material response. This portion is extracted by averaging several collections at very positive τ_{21} values, where no material response is present due to the short coherence times of MoS_2 electronic states. The largest feature is ω_2 scatter. Cross-talk between digital-to-analog channels can also be seen as the negative portion that goes as ω_1 intensity. (d) Signal after (c) is subtracted. (e) Smoothed data. (f) Amplitude level (square root) data. This spectrum corresponds to that at 0 delay in Figure 8.9. Note that the color bar's range is different than in Figure 8.9.

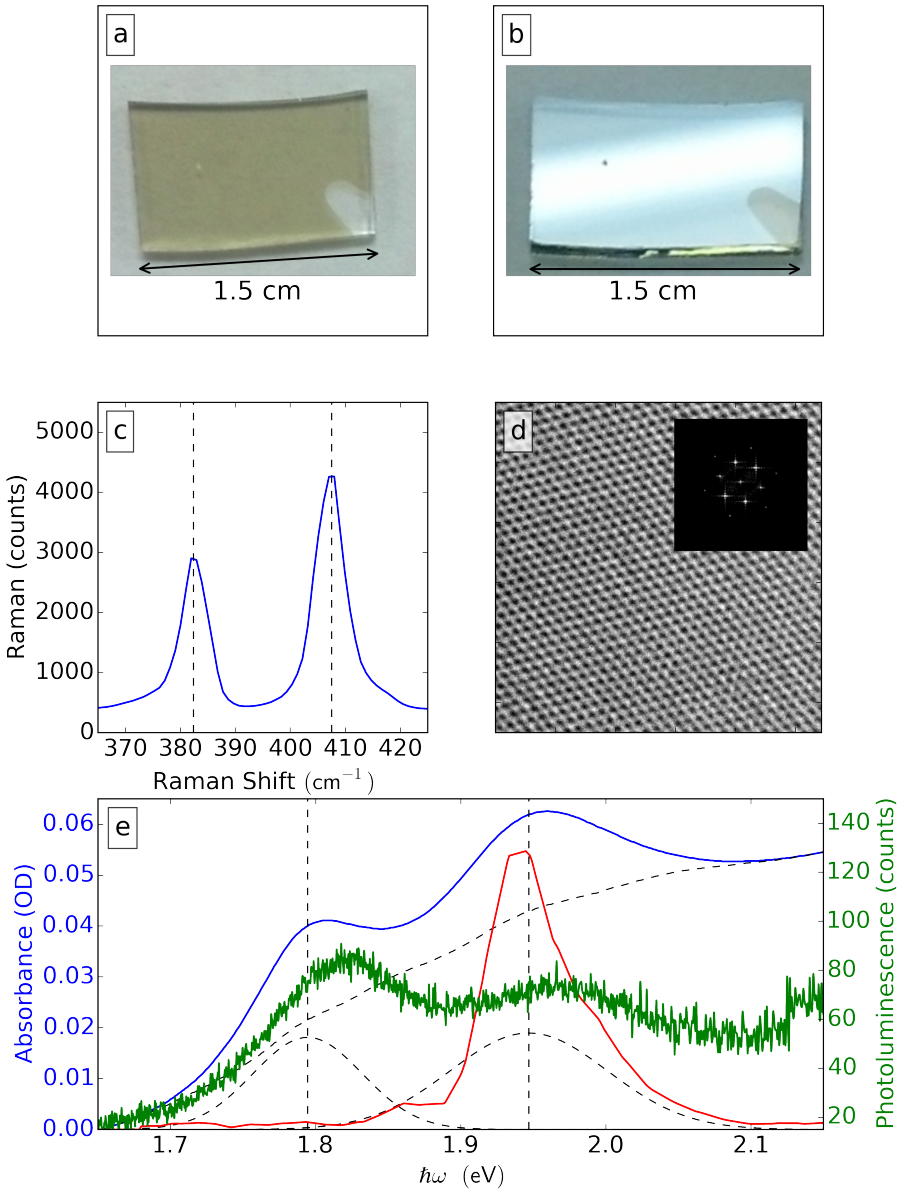

Figure 8.7: Characterization of the few-layer MoS_2 film studied in this work. Optical images of the MoS_2 thin film on fused silica substrate in (a) transmission and (b) reflection. (c) Raman spectrum of the E^1_{2g} and A_{1g} vibrational modes. (d) High-resolution TEM image and its corresponding FFT shown in the inset. (e) Absorption (blue), photoluminescence (green), Gaussian fits to the A and B excitons, along with the residules betwen the fits and absorbance (dotted), A and B exciton centers (dotted) and representative excitation pulse shape (red).

8.3 Results and discussion

The few-layer MoS_2 thin film sample studied in this work was prepared on a transparent fused silica substrate by a simple sufidation reaction of a Mo thin film using a procedure modified from a recent report. [36] Figure 8.7a and b show the homogeneous deposition and surface smoothness of the sample over the centimeter-sized fused silica substrate, respectively. The Raman spectrum shows the E^1_{2g} and A_{1g} vibrational modes (Figure 8.7c) that are characteristic of MoS_2. ¡teLiSongLin2012a The transmission electron micrograph (TEM) in Figure 8.7d shows the lattice fringes of the film with an inset fast Fourier transform (FFT) of the TEM image indicative of the hexagonal crystal structure of the film corresponding to the 0001 plane of MoS_2. [42] The MoS_2 film thickness was determined to be 2.66 nm by atomic force microscopy and corresponds to approximately four monolayers. Figure 8.73 shows the absorption and fluorescence spectrum of the film along with the A and B excitonic line shapes that were extracted from the absorption spectrum. A representative excitation pulse profile is also shown in red for comparison.

Extracting the exciton absorbance spectrum is complicated by the large "rising background" signal from other MoS_2 bands. With this in mind, we fit the second derivative absorption spectrum to a sum of two second derivative Gaussians, as seen in Figure 8.8. Conceptually, this method can be thought of as maximizing the smoothness (as opposed to minimizing the amplitude) of the remainder between the fit and the absorption spectrum. The fit parameters can be found in the inset table in Figure 8.8. The Gaussians themselves and the remainder can be found in Figure 8.8.

The multiresonant CMDS experiment uses ≈70 fs excitation pulses created by two independently tunable optical parametric amplifiers (OPAs). Automated delay stages and neutral density filters set the excitation time delays over all values of τ_{21} with $\tau_{22'} = 0$ and the pulse fluence to 90 μJ/cm^2 (114 μJ/cm^2) for the ω_1 (ω_2 and $\omega_{2'}$) beam(s). Each pulse was focused onto the sample using a distorted BOXCARS configuration. [43] The FWM signal was spatially isolated and detected with a monochromator that tracks the output frequency so $\omega_m = \omega_1$. In order to compare the FWM spectra with the absorption spectrum, the signal has been defined as the square root of the measured FWM signal since FWM depends quadratically on the sample concentration and path length.

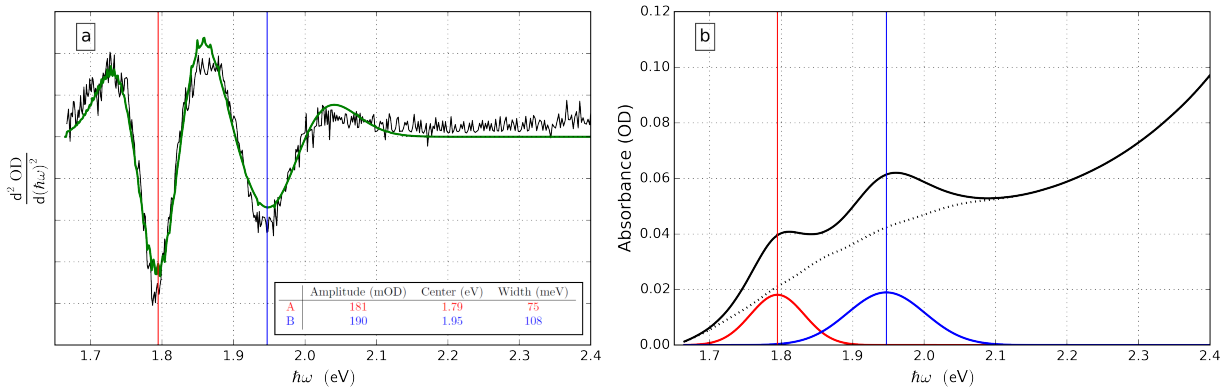

Figure 8.8: Extraction of excitonic features from absorbance spectrum. (a) Second derivative spectra of absorbance (black) and fit second derivative spectrum (green). Gaussian fit parameters are shown in the inset table. (b) Absorption curve (black), Gaussian fits (blue and red), and remainder (black dotted).

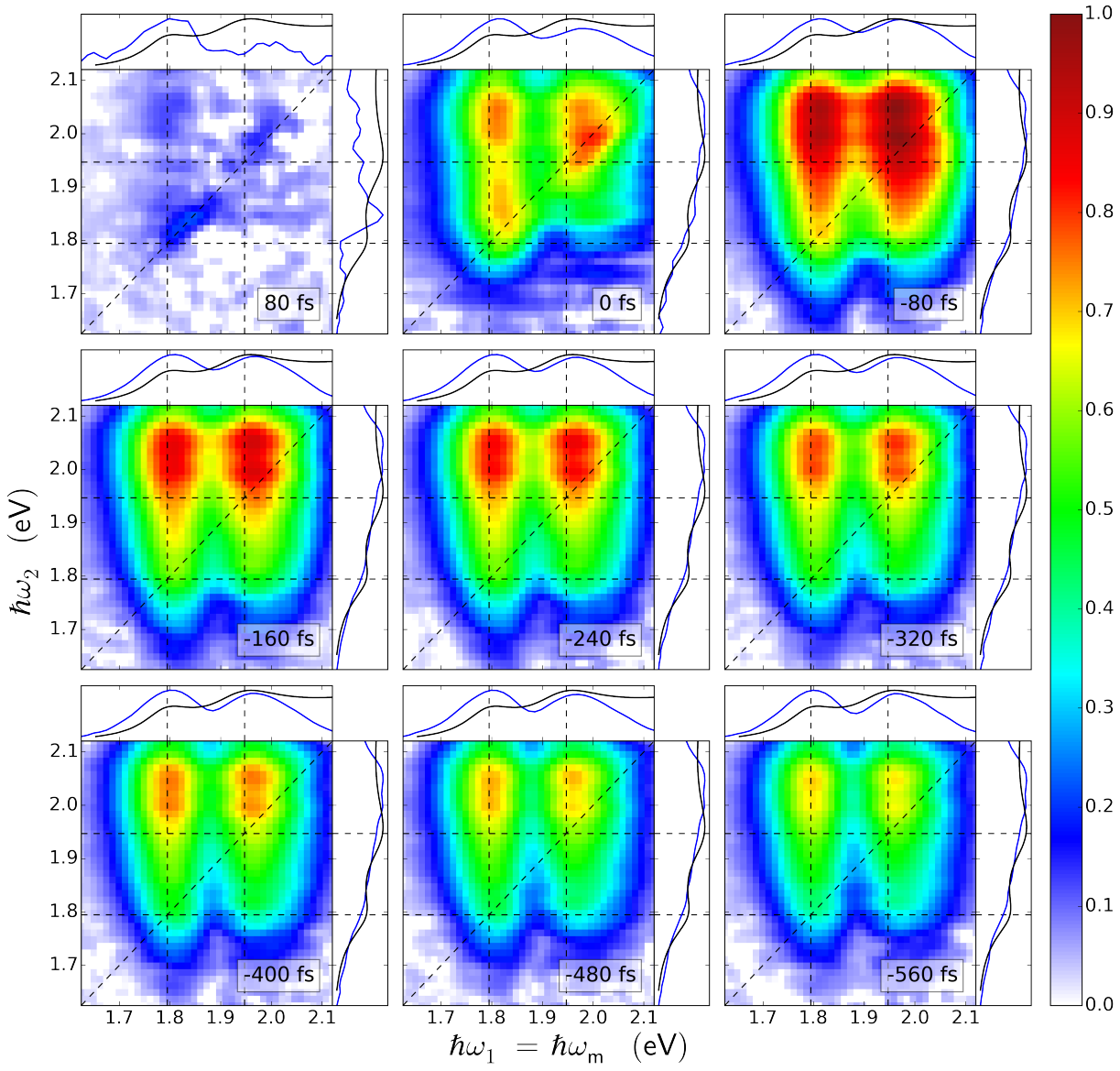

Figure 8.9: 2D frequency-frequency spectra of the MoS_2 sample in the epi configuration. In all spectra $\tau_{22'} = 0$ fs, while τ_{21} is designated in the bottom-right corner of each spectral panel. The color bar defines the square root of the intensity normalized to the most intense feature in the series of spectra. The integration of the signal onto the $\hbar\omega_1 = \hbar\omega_m$ and $\hbar\omega_2$ axes are represented ans the blue curves in the top and right side plots, respectively. The side plots also contain the absorbance spectrum (black line) to aid intepretation of the dynamics of the integrated 2D signals. The dashed lines mark the centers of the A and B excitons, as designated from the absorption spectrum.

The main set of data presented in this work is an $\omega_1\omega_2\tau_{21}$ "movie" with $\tau_{22\prime} = 0$. **??** shows representative 2D frequency-frequency slices from this movie at increasingly negative τ_{21} times. Each 2D frequency spectrum contains side plots along both axes that compare the absorbance spectrum (black) to the projection of the integrated signal onto the axis (blue). Along ω_1 (which for negative τ_{21} times acts as the "probe") we observe two peaks corresponding to the A and B excitons. In contrast, we see no well-defined excitonic peaks along the ω_2 "pump" axis. Instead, the signal amplitude increases toward bluer ω_2 values. The decrease in FWM above 2.05 eV is caused by a drop in the ω_2 OPA power.

Figures 8.10 and 8.11 show representative 2D frequency-delay slices from this movie, where the absicissa is the ω_1 or ω_2 frequency, respectively, the ordinate is the τ_{21} delay time, and the solid bold lines represent five different ω_2 or ω_1 frequencies. The color bar is normalized to the brightest feature in each subplot. This normalization allows comparison of the time dependence of the line shapes, positions, and relative signal amplitudes along the ω_1 or ω_2 axis directly.

Each subplot in Figure 8.10 is similar to published pump-probe, transient absorption, multidimensional and transient reflection experiments that have measured the electronc dynamics of the A and B excitons. [20, 21, 4, 22, 23, 24, 26, 44] These previous experiments measure relaxation dynamics on the same $\approx$400-600 fs time scale that is characteristic of Figure 8.10.

Our experiments also show how the spectral features change as a function of the ω_2 excitation frequency. The top to subplots of Figure 8.10 reflect the changes in the AA and BA features, while the bottom two subplots reflect the changes in the AB and BB features. The figure highlights the changes in the relative amplitude of the A and B features as a function of excitation frequency. Both the line shapes and the dynamics of the spectral features are very similar. Figure 8.11 is an excitation spectrum that shows that the dynamics of the spectral features do not depend strongly on the ω_1 frequency.

The spectral features in Figures 8.9, 8.10 and 8.11 depend on the quantum mechanical interference effects caused by the different pathways. Figure 8.12 shows all of the Liouville pathways required to understand the spectral features. [45, 46] These pathways correspond to the time orderings labeled V and VI in Figure 8.7b. The letters denote the density matrix elements, ρ_{ij}, where g representest the ground state and e, e$'$ represent any excitonic state. Interaction with the temporally overlapped ω_2 and

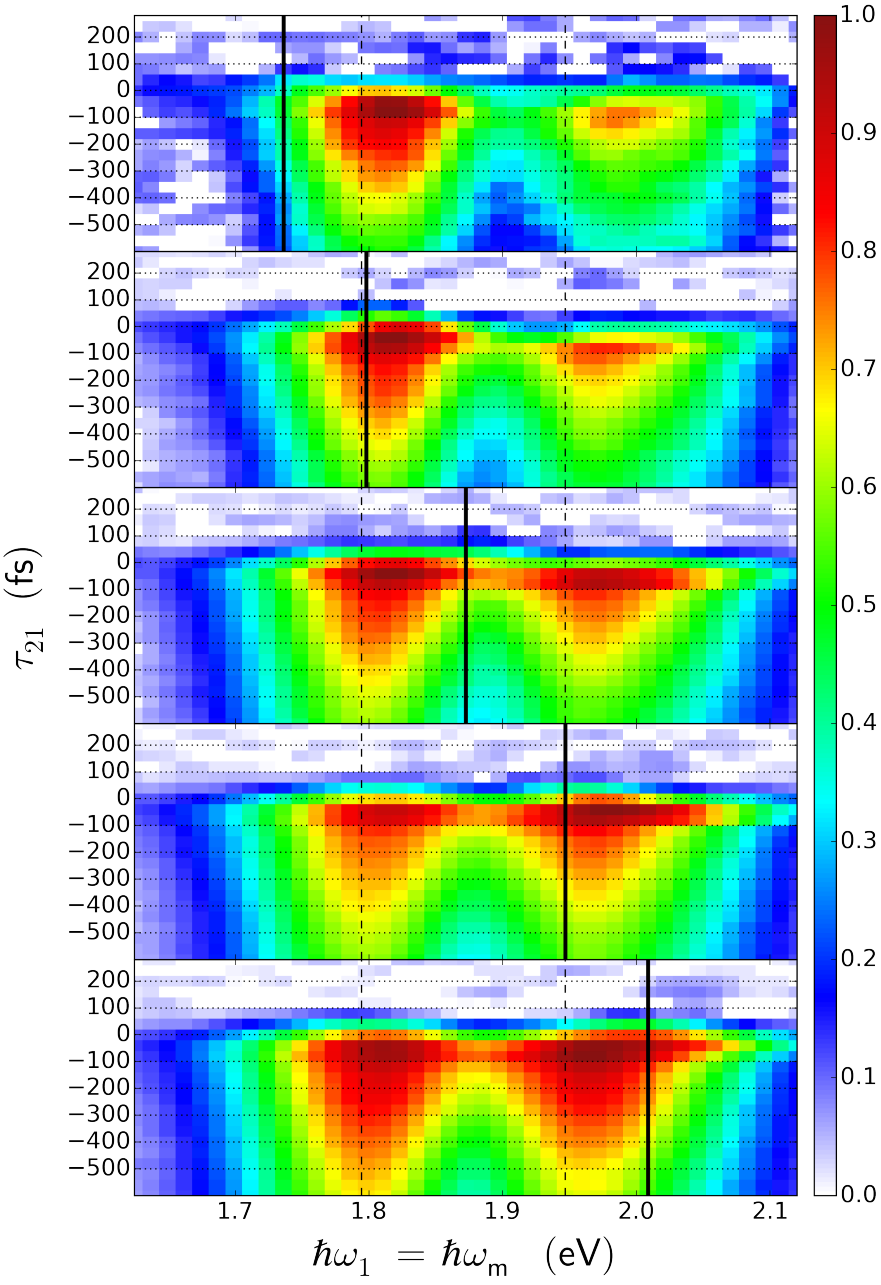

Figure 8.10: Mixed ω_1—τ_{21} time—frequency representations of the 3D data set at five ascending ω_2 excitation frequencies (solid black lines) showing the impact of the ω_2 excitation frequency on the ω_1 spectral line shape as a function of time. The A and B exciton energies are marked as dashed lines within each spectrum.

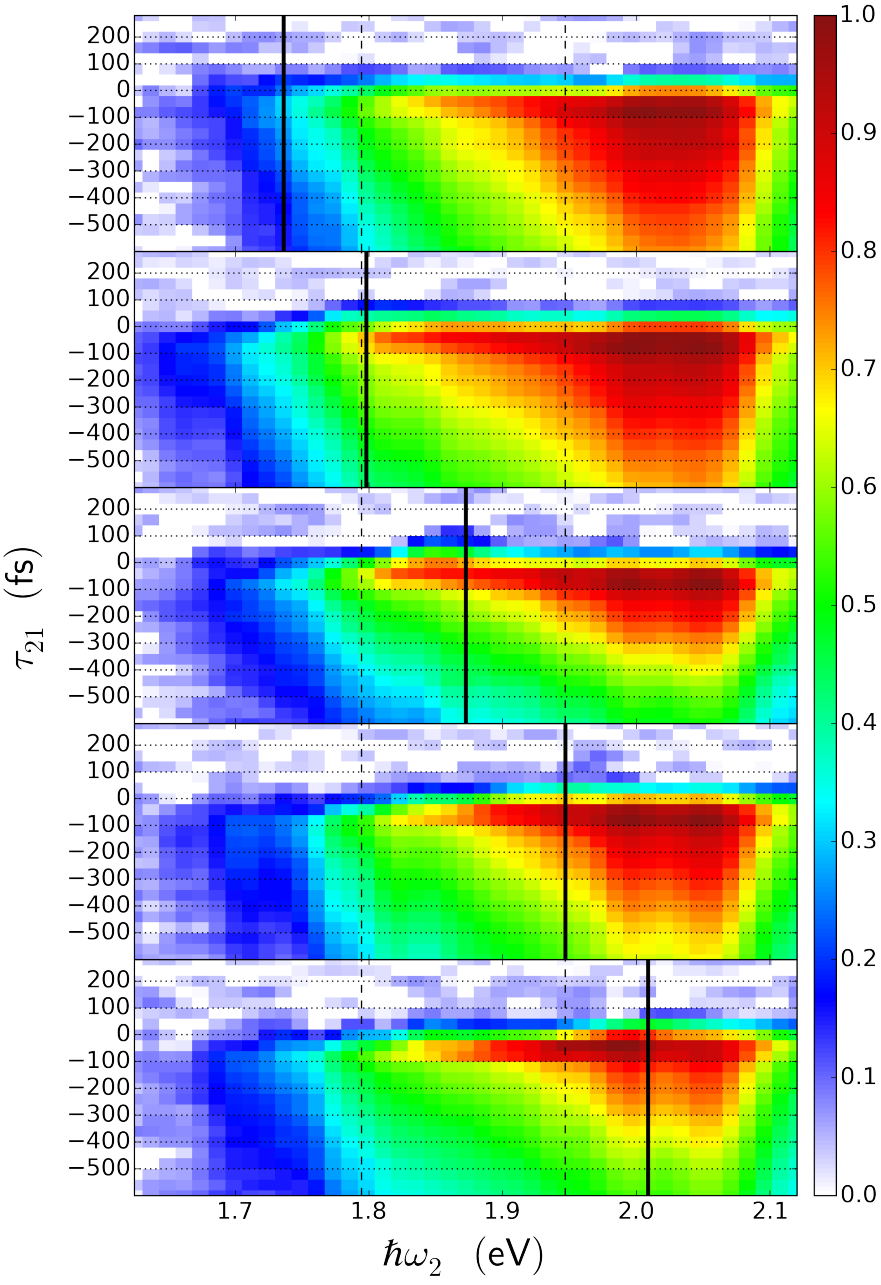

Figure 8.11: Mixed ω_2—τ_{21} time—frequency representations of the 3D data set at five ascending ω_1 probe frequencies (solid black lines) showing the impact of the ω_1 excitation frequency on the ω_2 spectral line shape as a function of time. The A and B exciton energies are marked as dashed lines within each spectrum.

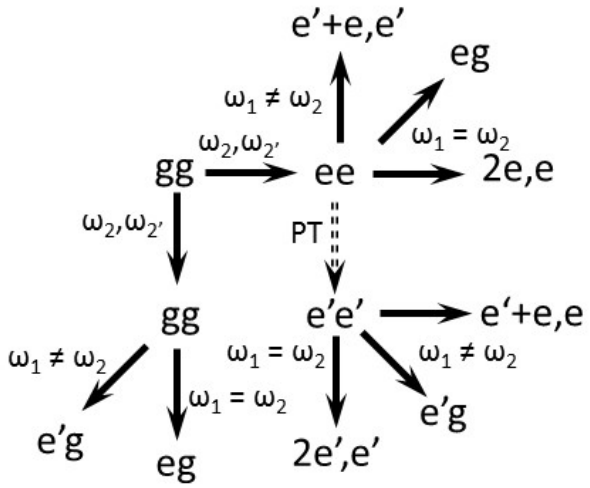

Figure 8.12: Liouville pathways for Figure 8.10. gg and ee designate ground- and excited-state populations, the eg, 2e,e, and e′+e,e represent the excitonic and biexcitonic output coherences, and the arrows are labeled with the frequencies or population transfer responsible for the transitions. e and e′ represent either A or B excitonic states.

$\omega_{2'}$ pulses excites the ee excited-state population and bleaches the ground-state population. Subsequent interaction with ω_1 creates the output coherences for the diagonal spectral features when $\omega_1 = \omega_2$ or the cross-peak features when $\omega_1 \neq \omega_2$. The stimulated emission (SE) and ground-state bleaching (GSB) pathways create the eg or e′g output coherences from the ee and gg populations, respectively, while the excited-state absorption pathway creates the 2e,e or e′+e,e biexcitonic output coherences. Figure 8.12 also includes a population transfer pathway from the ee excited-state population to an e′e′ population from which similar SE and ESA pathways occur. Since the ESA pathways destructively interfere with the SE and GSB pathways, the output singal depends on the differences between the pathways. Factors that change the biexcitonic output coherences such as the transition moments, state filling (Pauli blocking), frequency shifts, or dephasing rate changes will control the output signal. State filling and ground-state depletion are important factors for MoS_2 since the transitions excite specific electron and hole spin and valley states in individual layers.

The state-filling and ground-state bleaching effects on the diagonal and cross-peak features in Figure 8.9 depend on the spin and valley states in the output coherence. [19] The effects of these spins will disappear as the spin and valley states return to equilibrium. [47, 48, 49] If we assume spin relaxation is negligible, the FWM transitions that create the diagonal features involve either the A or B ESA transitions, so the resulting 2e,e state includes two spin-aligned conduction band electrons and valence band holes. Similarly, the cross-peak regions denoted by AB or BA in Figure 8.1d will have two transitions involving an A exciton, so the initial e′+e,e state will include antialigned spins. A quantitative treatment of the cancellation effects between the GSB, SE, and ESA pathways requries knowledge of the transition moments and state degeneracies and is beyond the scope of this paper. [50]

The most important characteristic of the experimental spectra is the contrast between the absence of well-resolved excitonic features that depend on ω_2 in Figures 8.9 and 8.11 and the well-defined excitonic features that depend on ω_1. It is also important to note that the projections of the signal amplitude onto the ω_2 axis in Figure 8.9 match closely with the continuum features in the absorption spectrum and that the line shapes of the features along the ω_2 axis in Figure 8.11 do not change appreciably for different delay times or ω_1 values. It shoudl be noted that the excitation pulse bandwidth (see Figure 8.7e) contributes to the absence of well-resolved A and B excitonic features along ω_2. The similarity to

the continuum states in the absorption spectrum and the absence of a strong dependence on ω_1 show that the continuum states observed at higher ω_2 frequencies participate directly in creating the final output coherences and that their increasing importance reflects the increasing absorption strength of higher energy continuum states. In contrast, the features dependent on ω_1 in Figures 8.9 and 8.10 match the line shapes of the A and B excitonic resonances. Although the relative amplitudes of the spectral features depend on the ω_2 frequency, they do not depend strongly on the delay times. These characteristics show that hot A and B excitonic states undergo rapid intraband population relaxation over a $<$70 fs time scale set by excitation pulses to the A and B excitonic states excited by ω_1.

A central feature of Figures 8.9 and 8.10 is that the AB region is much brighter than the BA region. This difference is suprising because simple models predict cross-peaks of equal amplitude, as depicted in Figure 8.1d. The symmetry in simple models arises because the AB and BA cross-peaks involve the same four transitions. The symmetry between AB and BA may be broken by material processes such as population relaxation and transfer, the output coherence dephasing rates, and the bleaching and state-filling effects of the valence and conduction band states involved in the transitions.

We believe that ultrafast intraband population transfer breaks the symmetry of AB and BA cross-peaks. For the BA peak, the interactions with ω_2 and $\omega_{2'}$ generate only A excitons that do not relax on $<$70 fs time scales. For the AB peak, ω_2 and $\omega_{2'}$ generate two kinds of excitons: (1) B excitons and (2) hot excitons in the A band. Relaxation to A may occur by interband transitions of B excitons or intraband transitions of hot A excitons. Either will lead to the GSB, SE, and ESA shown in the ee $\rightarrow$ e$'$e$'$ population transfer pathways of Figure 8.12. This relaxation must occur on the time scale of our pulse-width since the cross-peak asymmetry is observed even during temporal overlap. We believe that intraband relaxation of hot A excitons is the main factor in breaking the symmetry between AB and BA cross-peaks. Figure 8.10 shows that B $\rightarrow$ A interband relaxation occurs on a longer time scale. The B/A ratio is higher when ω_2 is resonant with the B excitonic transition than when ω_2 is lower than the A exciton frequency (the top subplot). If population transfer of holes from the B to A valence bands occurred during temporal overlap, the B/A ratio would be independent of pump frequency at $\tau_2 1 < 0$.

Figure 8.13 shows the delay transients at the different frequencies shown in the 2D spectrum. The colors of the dots on the 2D frequency-frequency spectrum match the colors of the transients. The transients

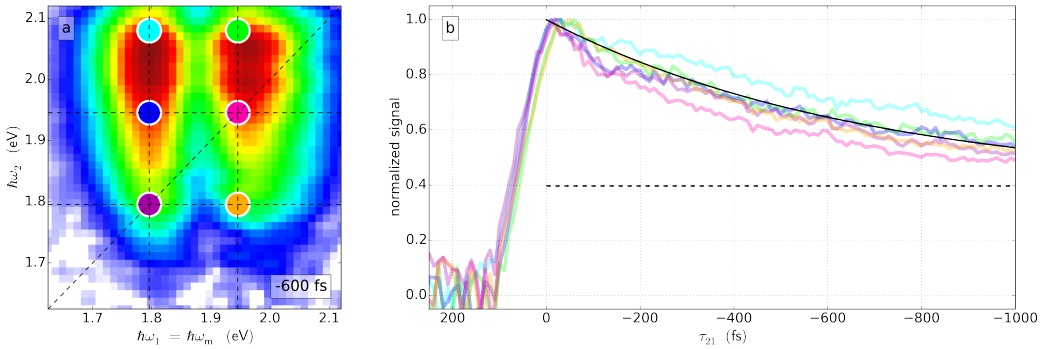

Figure 8.13: Transients taken at the different ω_1 and ω_2 frequencies indicated by the colored markers on the 2D spectrum. The dynamics are assigned to a 680 fs fast time constant (black solid line) and a slow time constant represented as an unchanging offset over this timescale (black dashed line).

were taken with a smaller step size and a longer time scale than the delay space explored in the 3D data set. The transients are quite similar. Our data are consistent with both monomolecular biexponential and bimolecular kinetic models and cannot discriminate between them. We have fit the decay kinetics to a single exponential model with a time constant of 680 fs and an offset that represents the long time decay. The 680 fs decay is similar to previously published pump-probe and transient absorption experiments. [22, 23, 51]

The spectral features change quantitatively for delay times near temporal overlap. Figure 8.14 shows a series of 2D spectra for both positive and negative τ_{21} delay times with $\tau_{22'} = 0$. Each spectrum is normalized to its brightest feature. The spectra at positive τ_{21} delay times become rapidly weaker as the delay times become more positive until the features vanish into the noise at $+120$ fs. The spectra also develop more diagonal character as the delay time moves from negative to positive values. The AB cross-peak is also a strong feature in the spectrum at early times.

The pulse overlap region is complicated by the multiple Liouville pathways that must be considered. Additionally, interference between scattered light from the ω_1 excitation beam and the output signal becomes a larger factor as the FWM signal decreases. Figure 8.15 shows the ω_1, ω_2, and $\omega_{2'}$ time ordered pathway that becomes and important consideration for positive τ_{21} delay times. Since $\tau_{22'} = 0$, the initial ω_1 pulse creates an excited-state coherence, while the subsequent ω_2 and $\omega_{2'}$ pulses create the output coherence. The output signal is only important at short $\tau_{21} > 0$ values because the initially excited coherence dephases very rapidly. When $\omega_1 \neq \omega_2$, the first two interactions create an e$'$e zero quantum coherence that also dephases rapidly. However, when $\omega_1 = \omega_2$, the first two interactions create an ee, gg population difference that relaxes on linger time scales. The resulting signal will therefore appear as the diagonal feature in Figure 8.14 (*e.g.*, see the $+40$ fs 2D spectrum). In addition to the diagonal feature in Figure 8.14, there is also a vertical feature when ω_1 is resonant with the A excitonic transition as well as the AB cross-peak. These features are attributed to the pathways in Figure 8.12. Although these pathways are depressed when $\tau_{21} > 0$, there is sufficient temporal overlap between the ω_2, $\omega_{2'}$, and ω_1 pulses to make their contribution comparable to those in Figure 8.15. More positie values of τ_{21} emphasize the Figure 8.15 pathways over the Figure 8.12 pathways, accounting for the increasing percentage of diagonal character at increasingly positive delays.

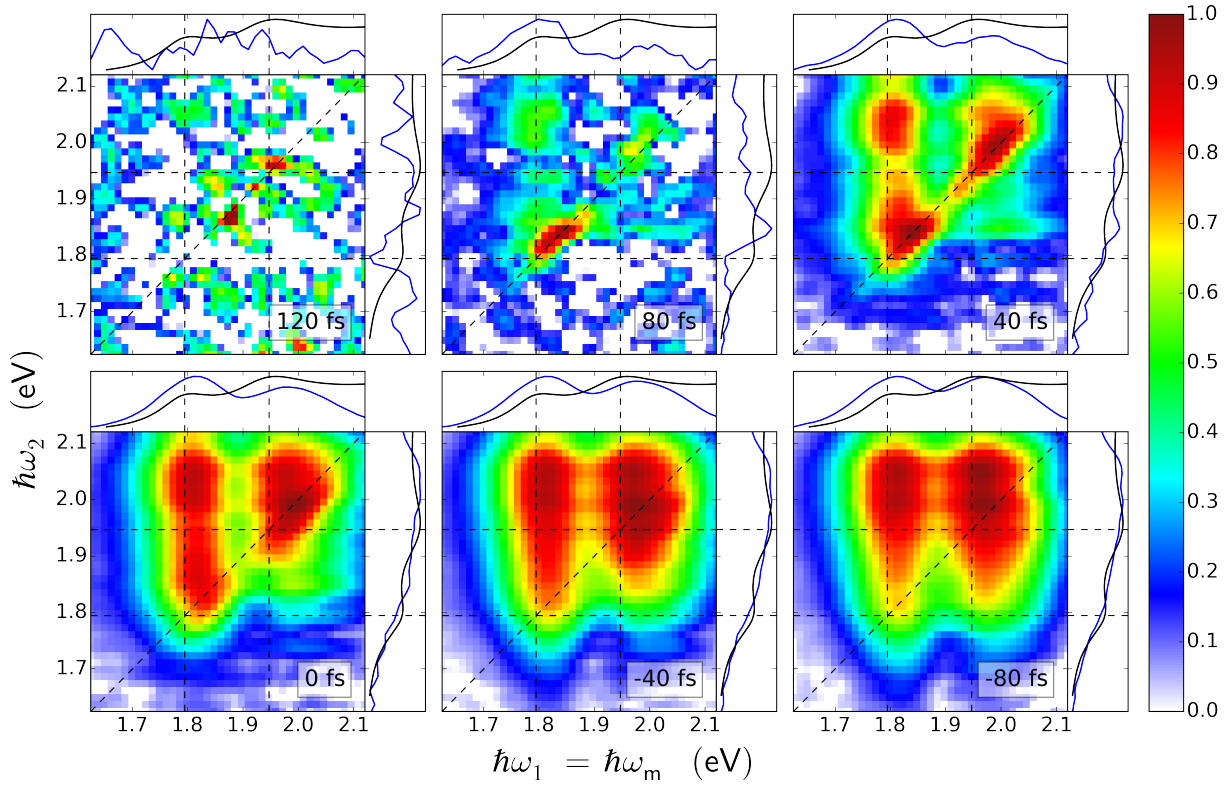

Figure 8.14: 2D frequency-frquency spectra near zero τ_{21} delay times. The signal amplitude is normalized to the brightest features in each spectrum.

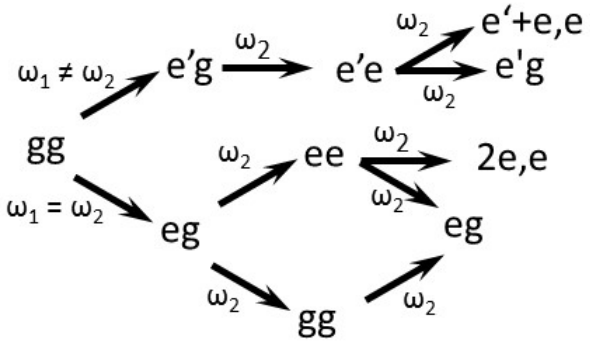

Figure 8.15: Liouville pathways for the ω_1, ω_2, and $\omega_{2'}$ time ordering of pulse interactions. e and e′ represent either A or B excitonic states.

8.4 Conclusions

This paper presents the first coherent multidimensional spectroscopy of MoS_2 thin films. CMDS methods are related to the earlier ultrafast pump-probe and transient absorption methods since they all share bleaching, stimulated emission, Pauli blocking, and excited-state absorption pathways, but they differ in how these pathways define the spectra. In addition, CMDS methods have many additional pathways that become important when the coherence dephasing times are longer than the excitation pulse widths. In this work, the dephasing times are short so the pathways are identical to transient absorption. This work reports the first frequency-frequency-delay spectra of MX_2 samples. These spectra are complementary to previous work because they allow a direct comparison between the initially excited excitonic states and the states creating the final output coherence. The spectra show that the same hot A and B exciton continuum states that are observed in the absorption spectrum also dominate the CMDS excitation spectra. They also show that rapid, ¡70 fs intraband relaxation occurs to create the band-edge A and B excitonic features observed in the CMSD spectrum. The relative intensity of the diagonal peak features depends on the relative absorption strength of the A and B excitons. The relative intensity of cross-peak features in the 2D spectra depends on the excitation frequency. Excitation at or above the B exciton feature creates strong cross-peaks associated with hot A and B excitons that undergo ultrafast intraband population transfer. Excitation below the B excitonic feature creates a weak cross-peak indicating A-induced B-state bleaching but at a lower signal level corresponding to the lower optical density at this energy. Population relaxation occurs over $\approx$680 fs, either by transfer to traps or by bimolecular charge recombination.

These experiments provide the understanding of MoS_2 coherent multidimensional spectra that will form the foundation required to measure the dynamical processes occurring in more complex MoS_2 and other TMDC heterostructures with quantum-state resolution. The frequency domain based multiresonant CMDS methods described in this paper will play a central role in these measurements. They use longer, independently tunable pulses that provide state-selective excitation over a wide spectral range without the requirement for interferometric stability.

Chapter 9

PEDOT:PSS

Chapter 10

Pyrite

Chapter 11

BiVO4

pass

Part IV

Appendix

Appendix A

Public

A.1 Chemical systems

Chemical systems are complex! They contain many molecules (10^{25} in a cup of coffee, 1 trillion in each human cell). These molecules have multiple interaction modes, both internal (intramolecular) and external (intermolecular). The reactivity of the system taken as a whole can be dominated by very rare but very important species, *e.g.* catalysts.

Despite this complexity, scientists have gotten very good at describing chemical systems through representations of dynamic equilibrium. In such situations, several key parameters emerge:

- concentration
- timescale (rate)
- lengthscale

A.1.1 Concentration

A.1.2 Timescale

A.1.3 Lengthscale

A.2 Analytical chemistry

Traditionally, chemists have seen fit to divide themselves into four specializations: analytical, inorganic, organic, and physical. In recent years, materials chemistry and chemical biology have become specializations in their own right. This dissertation focuses on analytical chemistry.

Analytical chemists separate, identify, and quantify chemical systems. To do this, we build instruments that exploit physical properties of the chemical components:

- separation science (chromatography, electrophoresis)
- mass spectrometry
- electrochemistry
- microscopy
- spectroscopy

Spectroscopy is a family of strategies that exploit the interaction of chemical systems with light.

A.3 Spectroscopy

Molecules respond to electric fields. Static electric fields cause charged molecules (ions) to move, as in electrophoresis and mass spectrometry. Oscillating electric fields, also known as light, can interact directly with the molecules themselves, driving transitions. However, these transitions can only be driven with the appropriate frequency of light (resonance). Different frequencies (colors) of light interact with different kinds of transitions, revealing different features of the molecule of interest.

A.3.1 Nonlinear spectroscopy

Spectroscopy is fantastic, but sometimes simple experiments don't reveal everything. Nonlinear spectroscopy uses multiple electric fields simultaniously, revealing even more information about the chemical system.

A.4 Instrumentation

To accomplish nonlinear spectroscopy, specialized light sources are needed:

- gigantic electric fields
- ultrafast time resoution
- tunable frequencies

A.4.1 LASER

These sources are made using Light Amplified by the Stimulated Emission of Radiation (LASER).

By keeping a wide range ofr colors in phase simulatniously, we are able to create truly ultrafast pulses of light. The work presented in this dissertation was primarily taken using a 35 fs 1 KHz system.

35 fs (35×10^{15} second) pulses are incredibly short:

$$\frac{\text{pulse duration (35 fs)}}{\text{time between pulses (1 ms)}} \approx \frac{\text{5.75 months}}{\text{age of universe (13.7 billion years)}} \tag{A.1}$$

proportionally, our sample spends 6 months in the "sun" for every age of the unverse in the dark.

Because all of the energy within the pulse is compressed to such a short period of time, these pulses are

also incredibly powerful:

$$\frac{\text{energy per pulse (4 mJ)}}{\text{pulse duration (35 fs)}} \approx \frac{\text{US electricity generation}(5.43 \times 10^{11} W)}{5} \tag{A.2}$$

this laser outputs electric fields one fifth as powerful as total US electricity generation (2016).

A.4.2 OPA

Appendix B

Procedures

B.1 Aligining TOPAS-C

B.2 Aligning Spitfire PRO

B.3 Air Handling

B.4 Six Month Maintenance

B.5 Tuning MicroHR Monochromator

Visible Grating.

Align the HeNe as perpendicular as possible to the monochromator entrance slit.

Move the grating angle until the HeNe falls on the exit slit.

Shine a flashlight through the entrance slit and observe the colour on the exit slit: if white, then you

are at 0-order (0 nm), if red, then you are at 1st order (632.8 nm).

Go to 0-order, narrow the slits, and slowly adjust the angle until the HeNe is going through the exit slit.

Go to Jovin Yvon/utilities and find the motor configuration program.

In the Gratings tab, select the 1st grating (1200 line density) and hit Calibrate.

In theoretical wavelength, enter 0 nm.

In experimental wavelength, enter the wavelength you observe from the control program.

Hit set.

Appendix C

Hardware

In this chapter I collect some of the specific hardware contribution details that do not belong in the body of the dissertation.

C.1 Adjustable periscopes

OPAs output horizontal or vertical polarizations according to which tuning process is used. Our experiments are opinionated about polarization, so some strategy for aligning polarization is necessary. In addition, it is useful to bring all excitation beams to the same height. To this end, I designed and constructed two adjustable periscopes. Each periscope is designed to bring OPA output to table height standard (5 inches) while either keeping or switching polarization. Both polarization configurations take the same path length, so source polarization can be switched without large changes to zero delay. All of this is done with just two (switched polarization) or three (kept polarzation) reflections. A picture of these periscopes is shown in C.1.

While these periscopes are easy to align, their unique design means that it is not necessarily obvious what the correct strategy is. The following strategy will always converge:

1. use two "magic" apertures along the output beamline

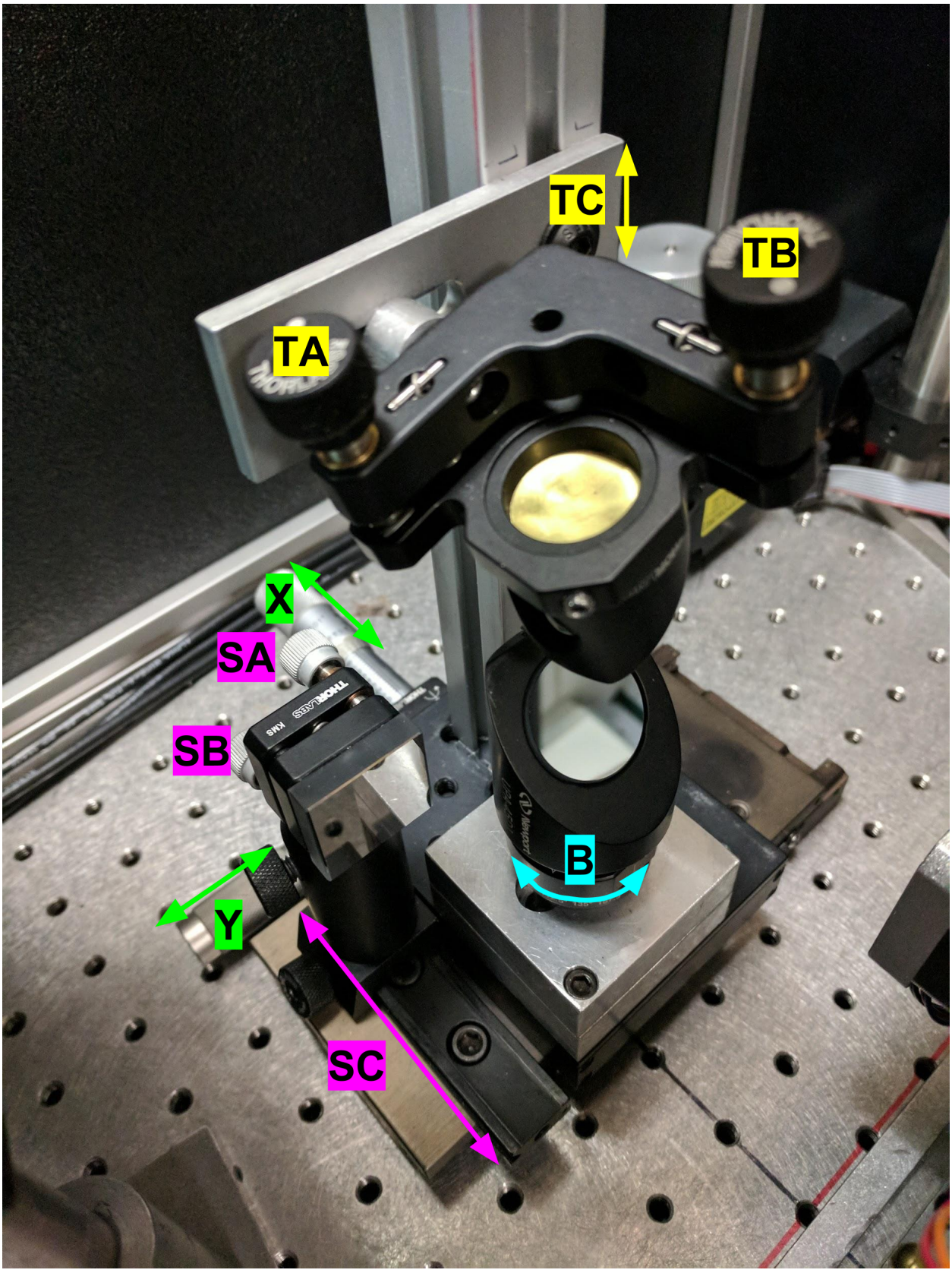

Figure C.1: CAPTION TODO

2. in flipped polarization (two mirror configuration):
    - use the stage (green X, Y) to align near aperture
    - use the upper mirror (yellow TA, TB) to align far aperture
    - iterate above
3. in kept polarization (three mirror configuration):
    - use stage X (green X) and upper mirror height (yellow TC) to align near aperture
    - use lower mirror (pink SA, SB) to align far aperture
    - iterate above

The kept polarization alignment is derivative of the fixed polarization alignment. One must ensure that the fixed polarization is correctly aligned at all times.

Mirror B (aqua) is magnetically mounted to switch between polarization conditions. Ensure that the lower turning mirror (pink) does not bump into mirror B (aqua) in polarization swtiching configuration. The lower turning mirror is on a rail (pink SC). This rail is a rough adjust for the same degree of freedom as pink SA. Adjust the rail only to ensure that the beam is roughly centered on the free aperture of the turning mirror.

The first reflection is often accomplished using a wedge, as OPA output may be strong enough to damage downstream optics. This optic can and should be replaced if more of the OPA output is desired on the table (keeping damage thresholds in mind).

C.1.1 Wedge polarization preference

TODO: wedges will be more efficent at reflecting horizontal / vertical at 45 degrees

C.2 Automated transmissive filters

TODO

C.3 Electronics

TODO

Appendix D

Errata

In this appendix I list the errors I am currently aware of in my publications and associated work.

D.1 Czech 2015

The following is an errata for Czech et al. [52], published in November 2015.

- Reference 13 is identical to reference 9.
- In the last paragraph of the introduction the sentence "The experimental spectra differ from the simple 2D spectrum shown in Figure 1d and those of earlier CMDS experiments with model systems" appears. This sentence cites references 6 through 10. Instead, it should cite references 15 through 20.
- In the last paragraph begining on page 12148, the text "Automated delay stages and neutral density filters set the excitation time delays over all values of τ_{21} with $\tau_{22} = 0$" appears. For the second τ, the subscript should read $22'$, not 22.
- Caption of Figure 5 reads, in part: "showing the impact of the ω_1 excitation frequency on the ω_1 spectral line shape". This should instead read "showing the impact of the ω_1 excitation frequency on the ω_2 spectral line shape". The subscript on the last ω should be a 2 and not a 1.

- Figure 6 e′+e,e′ should read e′+e,e and vice versa.

Appendix E

Colophon

This chapter lays out the technical aspects of this dissertation as a software and data product, including instructions for obtaining the source and regeneration of figures and documents.

Bibliography

[1] Daniel Kahneman. *Thinking, Fast and Slow*. Farrar, Straus and Giroux, 2013. ISBN: 9780374533557.

[2] Duckhwan Lee and Andreas C. Albrecht. "A Unified View of Raman, Resonance Raman, and Fluorescence Spectroscopy (and their Analogues in Two-Photon Absorption". In: *Advances in infrared and Raman Spectroscopy*. Ed. by R. J. H. Clark and R. E. Hester. 1st ed. London; New York, 1985. Chap. 4, pp. 179–213. ISBN: 9780471906742.

[3] Jacques Pankove. *Optical Processes in Semiconductors*. Dover Publications, 1975. ISBN: 9780486602752.

[4] Nardeep Kumar, Jiaqi He, Dawei He, Yongsheng Wang, and Hui Zhao. "Charge carrier dynamics in bulk MoS2 crystal studied by transient absorption microscopy". In: *Journal of Applied Physics* 113.13 (2013), p. 133702. DOI: 10.1063/1.4799110.

[5] Ji-xin Cheng, Andreas Volkmer, Lewis D Book, and X Sunney Xie. "An Epi-Detected Coherent Anti-Stokes Raman Scattering (E-CARS) Microscope with High Spectral Resolution and High Sensitivity". In: *The Journal of Physical Chemistry B* 105.7 (Feb. 2001), pp. 1277–1280. DOI: 10.1021/jp003774a.

[6] Austin P. Spencer, Hebin Li, Steven T. Cundiff, and David M. Jonas. "Pulse Propagation Effects in Optical 2D Fourier-Transform Spectroscopy: Theory". In: *The Journal of Physical Chemistry A* 119.17 (2015), pp. 3936–3960. DOI: 10.1021/acs.jpca.5b00001.

[7] Jo Erskine Hannay, Carolyn MacLeod, Janice Singer, Hans Petter Langtangen, Dietmar Pfahl, and Greg Wilson. "How do scientists develop and use scientific software?" In: *2009 ICSE Workshop on Software Engineering for Computational Science and Engineering*. Institute of Electrical and Electronics Engineers (IEEE), May 2009. DOI: 10.1109/secse.2009.5069155.

[8] Judith Segal. "When Software Engineers Met Research Scientists: A Case Study". In: *Empirical Software Engineering* 10.4 (Oct. 2005), pp. 517–536. DOI: 10.1007/s10664-005-3865-y.

[9] Tobias Brixner, Tomas Mancal, Igor V. Stiopkin, and Graham R. Fleming. "Phase-stabilized two-dimensional electronic spectroscopy". In: *The Journal of Chemical Physics* 121.9 (2004), p. 4221. DOI: 10.1063/1.1776112.

[10] Lena A Yurs, Stephen B. Block, Andrei V Pakoulev, Rachel S. Selinsky, Song Jin, and John Wright. "Multiresonant Coherent Multidimensional Electronic Spectroscopy of Colloidal PbSe Quantum Dots". In: *The Journal of Physical Chemistry C* 115.46 (Nov. 2011), pp. 22833–22844. DOI: 10.1021/jp207273x.

[11] Koichi Furuta, Masanori Fuyuki, and Akihide Wada. "Cross-Term Selective, Two-Pulse Correlation Measurements by Phase-Shifted Parallel Modulation for Analysis of a Multi-Photon Process". In: *Applied Spectroscopy* 66.12 (Dec. 2012), pp. 1475–1479. DOI: 10.1366/12-06657.

[12] Ramūnas Augulis and Donatas Zigmantas. "Two-dimensional electronic spectroscopy with double modulation lock-in detection: enhancement of sensitivity and noise resistance." In: *Optics express* 19.14 (June 2011), pp. 13126–13133. DOI: 10.1364/OE.19.013126.

[13] Ismael A. Heisler, Roberta Moca, Franco V A Camargo, and Stephen R. Meech. "Two-dimensional electronic spectroscopy based on conventional optics and fast dual chopper data acquisition". In: *Review of Scientific Instruments* 85.6 (June 2014), p. 063103. DOI: 10.1063/1.4879822.

[14] Ivan C. Spector, Courtney M. Olson, Christopher J. Huber, and Aaron M. Massari. "Simple fully reflective method of scatter reduction in 2D-IR spectroscopy". In: *Optics Letters* 40.8 (Apr. 2015), pp. 1850–1852. DOI: 10.1364/OL.40.001850.

[15] Brian L. McClain, Ilya J. Finkelstein, and M. D. Fayer. "Vibrational echo experiments on red blood cells: Comparison of the dynamics of cytoplasmic and aqueous hemoglobin". In: *Chemical Physics Letters* 392.4-6 (July 2004), pp. 324–329. DOI: 10.1016/j.cplett.2004.05.080.

[16] Qing Hua Wang, Kourosh Kalantar-Zadeh, Andras Kis, Jonathan N. Coleman, and Michael S. Strano. "Electronics and optoelectronics of two-dimensional transition metal dichalcogenides". In: *Nature Nanotechnology* 7.11 (Nov. 2012), pp. 699–712. DOI: 10.1038/nnano.2012.193. URL: https://doi.org/10.1038/nnano.2012.193.

[17] Kin Fai Mak, Changgu Lee, James Hone, Jie Shan, and Tony F. Heinz. "Atomically ThinMoS2: A New Direct-Gap Semiconductor". In: *Physical Review Letters* 105.13 (Sept. 2010). DOI: 10.1103/physrevlett.105.136805.

[18] Alejandro Molina-Sánchez, Davide Sangalli, Kerstin Hummer, Andrea Marini, and Ludger Wirtz. "Effect of spin-orbit interaction on the optical spectra of single-layer, double-layer, and bulk MoS2". In: *Physical Review B* 88.4 (July 2013). DOI: 10.1103/physrevb.88.045412.

[19] Xiaodong Xu, Wang Yao, Di Xiao, and Tony F. Heinz. "Spin and pseudospins in layered transition metal dichalcogenides". In: *Nature Physics* 10.5 (Apr. 2014), pp. 343–350. DOI: 10.1038/nphys2942.

[20] Di Xiao, Gui-Bin Liu, Wanxiang Feng, Xiaodong Xu, and Wang Yao. "Coupled Spin and Valley Physics in Monolayers ofMoS2and Other Group-VI Dichalcogenides". In: *Physical Review Letters* 108.19 (May 2012). DOI: 10.1103/physrevlett.108.196802.

[21] H. Fang, C. Battaglia, C. Carraro, S. Nemsak, B. Ozdol, J. S. Kang, H. A. Bechtel, S. B. Desai, F. Kronast, A. A. Unal, G. Conti, C. Conlon, G. K. Palsson, M. C. Martin, A. M. Minor, C. S. Fadley, E. Yablonovitch, R. Maboudian, and A. Javey. "Strong interlayer coupling in van der Waals heterostructures built from single-layer chalcogenides". In: *Proceedings of the National Academy of Sciences* 111.17 (Apr. 2014), pp. 6198–6202. DOI: 10.1073/pnas.1405435111.

[22] Zhaogang Nie, Run Long, Linfeng Sun, Chung-Che Huang, Jun Zhang, Qihua Xiong, Daniel W. Hewak, Zexiang Shen, Oleg V. Prezhdo, and Zhi-Heng Loh. "Ultrafast Carrier Thermalization and Cooling Dynamics in Few-Layer MoS2". In: *ACS Nano* 8.10 (Oct. 2014), pp. 10931–10940. DOI: 10.1021/nn504760x.

[23] Dezheng Sun, Yi Rao, Georg A. Reider, Gugang Chen, Yumeng You, Louis Brézin, Avetik R. Harutyunyan, and Tony F. Heinz. "Observation of Rapid Exciton–Exciton Annihilation in Monolayer Molybdenum Disulfide". In: *Nano Letters* 14.10 (Oct. 2014), pp. 5625–5629. DOI: 10.1021/nl5021975.

[24] Sangwan Sim, Jusang Park, Jeong-Gyu Song, Chihun In, Yun-Shik Lee, Hyungjun Kim, and Hyunyong Choi. "Exciton dynamics in atomically thin MoS2: Interexcitonic interaction and broadening kinetics". In: *Physical Review B* 88.7 (Aug. 2013). DOI: 10.1103/physrevb.88.075434.

[25] Patanjali Kambhampati. "Unraveling the Structure and Dynamics of Excitons in Semiconductor Quantum Dots". In: *Accounts of Chemical Research* 44.1 (Jan. 2011), pp. 1–13. DOI: 10.1021/ar1000428.

[26] Kin Fai Mak, Keliang He, Jie Shan, and Tony F. Heinz. "Control of valley polarization in monolayer MoS2 by optical helicity". In: *Nature Nanotechnology* 7.8 (June 2012), pp. 494–498. DOI: 10.1038/nnano.2012.96.

[27] Steven T. Cundiff. "Coherent spectroscopy of semiconductors". In: *Optics Express* 16.7 (Mar. 2008), p. 4639. DOI: 10.1364/oe.16.004639.

[28] Daniel B. Turner, Katherine W. Stone, Kenan Gundogdu, and Keith A. Nelson. "Three-dimensional electronic spectroscopy of excitons in GaAs quantum wells". In: *The Journal of Chemical Physics* 131.14 (Oct. 2009), p. 144510. DOI: 10.1063/1.3245964.

[29] Daniel D. Kohler, Stephen B. Block, Schuyler Kain, Andrei V. Pakoulev, and John C. Wright. "Ultrafast Dynamics within the 1S Exciton Band of Colloidal PbSe Quantum Dots Using Multiresonant Coherent Multidimensional Spectroscopy". In: *The Journal of Physical Chemistry C* 118.9 (Mar. 2014), pp. 5020–5031. DOI: 10.1021/jp412058u. URL: https://doi.org/10.1021/jp412058u.

[30] Graham B. Griffin, Sandrine Ithurria, Dmitriy S. Dolzhnikov, Alexander Linkin, Dmitri V. Talapin, and Gregory S. Engel. "Two-dimensional electronic spectroscopy of CdSe nanoparticles at very low pulse power". In: *The Journal of Chemical Physics* 138.1 (Jan. 2013), p. 014705. DOI: 10.1063/1.4772465. URL: https://doi.org/10.1063/1.4772465.

[31] Elad Harel, Sara M. Rupich, Richard D. Schaller, Dmitri V. Talapin, and Gregory S. Engel. "Measurement of electronic splitting in PbS quantum dots by two-dimensional nonlinear spectroscopy". In: *Physical Review B* 86.7 (Aug. 2012). DOI: 10.1103/physrevb.86.075412. URL: https://doi.org/10.1103/physrevb.86.075412.

[32] S. T. Cundiff, M. Koch, W. H. Knox, J. Shah, and W. Stolz. "Optical Coherence in Semiconductors: Strong Emission Mediated by Nondegenerate Interactions". In: *Physical Review Letters* 77.6 (Aug. 1996), pp. 1107–1110. DOI: 10.1103/physrevlett.77.1107. URL: https://doi.org/10.1103/physrevlett.77.1107.

[33] D. Birkedal, V. G. Lyssenko, J. M. Hvam, and K. El Sayed. "Continuum contribution to excitonic four-wave mixing due to interaction-induced nonlinearities". In: *Physical Review B* 54.20 (Nov. 1996), R14250–R14253. DOI: 10.1103/physrevb.54.r14250. URL: https://doi.org/10.1103/physrevb.54.r14250.

[34] M. U. Wehner, D. Steinbach, and M. Wegener. "Ultrafast coherent transients due to exciton-continuum scattering in bulk GaAs". In: *Physical Review B* 54.8 (Aug. 1996), R5211–R5214. DOI: 10.1103/physrevb.54.r5211. URL: https://doi.org/10.1103/physrevb.54.r5211.

[35] Andrei V. Pakoulev, Mark A. Rickard, Kent A. Meyer, Kathryn Kornau, Nathan A. Mathew, David E. Thompson, and John C. Wright. "Mixed Frequency/Time Domain Optical Analogues of Heteronuclear Multidimensional NMR". In: *The Journal of Physical Chemistry A* 110.10 (Mar. 2006), pp. 3352–3355. DOI: 10.1021/jp057339y. URL: https://doi.org/10.1021/jp057339y.

[36] Masihhur R. Laskar, Lu Ma, Santhakumar Kannappan, Pil Sung Park, Sriram Krishnamoorthy, Digbijoy N. Nath, Wu Lu, Yiying Wu, and Siddharth Rajan. "Large area single crystal (0001) oriented MoS2". In: *Applied Physics Letters* 102.25 (June 2013), p. 252108. DOI: 10.1063/1.4811410. URL: https://doi.org/10.1063/1.4811410.

[37] A. Castellanos-Gomez, M. Barkelid, A. M. Goossens, V. E. Calado, H. S. J. van der Zant, and G. A. Steele. "Laser-Thinning of MoS2: On Demand Generation of a Single-Layer Semiconductor". In: *Nano Letters* 12.6 (June 2012), pp. 3187–3192. DOI: 10.1021/nl301164v. URL: https://doi.org/10.1021/nl301164v.

[38] Mariyappan Shanmugam, Chris A. Durcan, and Bin Yu. "Layered semiconductor molybdenum disulfide nanomembrane based Schottky-barrier solar cells". In: *Nanoscale* 4.23 (2012), p. 7399. DOI: 10.1039/c2nr32394j. URL: https://doi.org/10.1039/c2nr32394j.

[39] Andreas Volkmer, Ji-Xin Cheng, and X. Sunney Xie. "Vibrational Imaging with High Sensitivity via Epidetected Coherent Anti-Stokes Raman Scattering Microscopy". In: *Physical Review Letters* 87.2 (June 2001). DOI: 10.1103/physrevlett.87.023901. URL: https://doi.org/10.1103/physrevlett.87.023901.

[40] Fernando Perez and Brian E. Granger. "IPython: A System for Interactive Scientific Computing". In: *Computing in Science & Engineering* 9.3 (2007), pp. 21–29. DOI: 10.1109/mcse.2007.53. URL: https://doi.org/10.1109/mcse.2007.53.

[41] John D. Hunter. "Matplotlib: A 2D Graphics Environment". In: *Computing in Science & Engineering* 9.3 (2007), pp. 90–95. DOI: 10.1109/mcse.2007.55. URL: https://doi.org/10.1109/mcse.2007.55.

[42] Mark A. Lukowski, Andrew S. Daniel, Fei Meng, Audrey Forticaux, Linsen Li, and Song Jin. "Enhanced Hydrogen Evolution Catalysis from Chemically Exfoliated Metallic MoS2 Nanosheets". In: *Journal of the American Chemical Society* 135.28 (July 2013), pp. 10274–10277. DOI: 10.1021/ja404523s. URL: https://doi.org/10.1021/ja404523s.

[43] Alan C. Eckbreth. "BOXCARS: Crossed-beam phase-matched CARS generation in gases". In: *Applied Physics Letters* 32.7 (Apr. 1978), pp. 421–423. DOI: 10.1063/1.90070.

[44] Markus Thomalla and Helmut Tributsch. "Photosensitization of Nanostructured TiO2 with WS2 Quantum Sheets". In: *The Journal of Physical Chemistry B* 110.24 (June 2006), pp. 12167–12171. DOI: 10.1021/jp061371q. URL: https://doi.org/10.1021/jp061371q.

[45] Andrei V. Pakoulev, Stephen B. Block, Lena A. Yurs, Nathan A. Mathew, Kathryn M. Kornau, and John C. Wright. "Multiply Resonant Coherent Multidimensional Spectroscopy: Implications for Materials Science". In: *The Journal of Physical Chemistry Letters* 1.5 (Mar. 2010), pp. 822–828. DOI: 10.1021/jz9003476. URL: https://doi.org/10.1021/jz9003476.

[46] Andrei V. Pakoulev, Mark A. Rickard, Kathryn M. Kornau, Nathan A. Mathew, Lena A. Yurs, Stephen B. Block, and John C. Wright. "Mixed Frequency-/Time-Domain Coherent Multidimensional Spectroscopy: Research Tool or Potential Analytical Method?" In: *Accounts of Chemical Research* 42.9 (Sept. 2009), pp. 1310–1321. DOI: 10.1021/ar900032g. URL: https://doi.org/10.1021/ar900032g.

[47] Hualing Zeng, Junfeng Dai, Wang Yao, Di Xiao, and Xiaodong Cui. "Valley polarization in MoS2 monolayers by optical pumping". In: *Nature Nanotechnology* 7.8 (June 2012), pp. 490–493. DOI: 10.1038/nnano.2012.95. URL: https://doi.org/10.1038/nnano.2012.95.

[48] Bairen Zhu, Hualing Zeng, Junfeng Dai, and Xiaodong Cui. "The Study of Spin-Valley Coupling in Atomically Thin Group VI Transition Metal Dichalcogenides". In: *Advanced Materials* 26.31 (Apr. 2014), pp. 5504–5507. DOI: 10.1002/adma.201305367. URL: https://doi.org/10.1002/adma.201305367.

[49] Cong Mai, Andrew Barrette, Yifei Yu, Yuriy G. Semenov, Ki Wook Kim, Linyou Cao, and Kenan Gundogdu. "Many-Body Effects in Valleytronics: Direct Measurement of Valley Lifetimes in Single-Layer MoS2". In: *Nano Letters* 14.1 (Dec. 2013), pp. 202–206. DOI: 10.1021/nl403742j. URL: https://doi.org/10.1021/nl403742j.

[50] Cathy Y. Wong and Gregory D. Scholes. "Using two-dimensional photon echo spectroscopy to probe the fine structure of the ground state biexciton of CdSe nanocrystals". In: *Journal of Luminescence* 131.3 (Mar. 2011), pp. 366–374. DOI: 10.1016/j.jlumin.2010.09.015. URL: https://doi.org/10.1016/j.jlumin.2010.09.015.

[51] Callum J. Docherty, Patrick Parkinson, Hannah J. Joyce, Ming-Hui Chiu, Chang-Hsiao Chen, Ming-Yang Lee, Lain-Jong Li, Laura M. Herz, and Michael B. Johnston. "Ultrafast Transient Terahertz Conductivity of Monolayer MoS2 and WSe2 Grown by Chemical Vapor Deposition". In: *ACS Nano* 8.11 (Nov. 2014), pp. 11147–11153. DOI: 10.1021/nn5034746. URL: https://doi.org/10.1021/nn5034746.

[52] Kyle J. Czech, Blaise J. Thompson, Schuyler Kain, Qi Ding, Melinda J. Shearer, Robert J. Hamers, Song Jin, and John C. Wright. "Measurement of Ultrafast Excitonic Dynamics of Few-Layer MoS2Using State-Selective Coherent Multidimensional Spectroscopy". In: *ACS Nano* 9.12 (Dec. 2015), pp. 12146–12157. DOI: 10.1021/acsnano.5b05198.